

DISS. ETH NO. 25474

***Conformal Deposition of Metal Silicide Layer on Si Wafer  
for Transistor Technology via a Molecular Approach***

A thesis submitted to attain the degree of  
DOCTOR OF SCIENCES of ETH ZURICH  
(Dr. sc. ETH Zurich)

presented by

*Tsung-Han Lin*

*MSc., National Taiwan University, Taiwan*

Born on 16.06.1987

Citizen of Taiwan

Accepted on the recommendation of

*Prof. Dr. C. Copéret, examiner*

*Prof Dr. V. Wood, co-examiner*

*Prof. Dr. C. –J. Shih, co-examiner*

2018





*to my wife, 家綸 (Cathy)*

*for her unconditional support*



## Acknowledgement

I would like to express my sincere gratitude to people who have ever helped me in any way during my PhD. All the works are not possible to be done without the helps from all of you.

First of all, I would like to thank Prof. Dr. Christophe Copéret for giving me the opportunity to do my PhD in this resourceful group, and always providing me with instructive advices and guidance on my research. His academic passion and working attitude always inspire me a lot. Also, I am grateful to Prof. Dr. Vanessa Wood and Prof. Dr. Chih-Jen Shih for being my PhD referees and attending my public presentations with many meaningful suggestions and questions afterwards. Dr. Wei-Chih Liao is thanked for his advertisement of this PhD position so that I could start this wonderful journey. I also thank Prof. Dr. Pierre-Emmanuel Gaillardon and Prof. Dr. Giovanni De Micheli, who always provide meaningful suggestions and supports to this thesis and guides me into the field of microelectronic devices from the beginning of my PhD. I want to thank Dr. David Baudouin for our collaboration and discussion during these 4 years.

Secondly, I acknowledge Dr. Tigran Margossian for being my mentor in my first year of PhD, leading me into the world of colloidal chemistry and encouraging me in many ways. I also want to thank Rick, Dima, Keith, and Kim, who ever advised me during my PhD. All the group members and collaborators are kindly acknowledged for the discussion and experimental supports, during which I met full of great friends all around the world. In addition, I appreciate all my friends in H206: Tigran, Shohei, Patrick, Kim, Keith, Erwin, Gina, etc, who makes the room full of interesting words and topics during these 4 years. I will also cherish the time when we played the football table or real football with Florian, Tigran, Maxence, Jordan, Erwin, Nicolas, Margherita, George, Dima, Ilia, Lukas, Christopher, Hung-Kun, etc.

Lastly, I appreciate the unconditional supports from my parents in my life. Special and very big thanks to my wife, Chia-Lun Chang (Cathy), who always supports and encourages me in any case. My lovely daughters, Yun-Ting and Yun-Fei, are also acknowledged for always making the house full of happiness.



# Table of contents

Acknowledgement .....	i
Abstract .....	1
Zusammenfassung.....	3
Chapter 1: Introduction .....	5
1.1. Basics of Semiconductor.....	5
1.2. Transistors.....	9
1.3. Metal-Silicon Alloys in Microelectronics.....	10
1.4. Salicidation Process for Metal Silicide .....	12
1.5. Thesis Objectives .....	15
1.6. Strategy and Thesis Outline .....	16
1.7. References.....	18
Chapter 2: Low Temperature Wet Conformal Nickel Silicide Deposition for Transistor Technology via a Molecular Approach .....	24
2.1. Introduction.....	25
2.2. Results and discussion .....	26
2.3. Conclusion .....	36
2.4. Experimental details.....	37
2.5. References.....	40
Chapter 3: Nickel Silicide Layer Deposition on Si Wafer for the Transistor Technology via a Molecular-Tailored Nickel Precursor in a Colloidal Approach.....	45
3.1. Intoduction .....	46
3.2. Results and discussion .....	47

3.3. Conclusion .....	51
3.4. Experimental details.....	52
3.5. References.....	55
Chapter 4: Conformal Deposition of Conductive Single-Crystalline Cobalt Silicide Layer on Si Wafer via a Molecular Approach .....	58
4.1. Introduction.....	59
4.2. Results and discussion .....	60
4.3. Conclusion .....	66
4.4. Experimental details.....	67
4.5. References.....	71
Chapter 5: Conclusions and Outlook .....	75
5.1. Conclusions.....	75
5.2. Outlooks.....	78
5.3. References.....	80
Appendix A: Annexes.....	81
Appendix B: Investigation of Phosphorus Grafting Capability on Silica with Different Surface Environments via $^{31}\text{P}$ NMR.....	111
B.1. Introduction .....	112
B.2. Results and discussion.....	113
B.3. Conclusion.....	121
B.4. Experimental details .....	122
B.5. References .....	125
Appendix C: Additional synthesis .....	132

Curriculum Vitae .....	136
------------------------	-----





## Abstract

The race for performance of integrated circuits is nowadays facing a downscale limitation. To overpass this nanoscale limit, modern transistors with complex geometries have flourished allowing higher performance and energy efficiency. Accompany with this breakthrough, processing challenges toward high-performance devices have emerged on each significant step. Metal silicides, which are of great interest to the microelectronics industry, are commonly used in current semiconductor devices as contacts between semiconductor substrate and metal lines for the most suitable electronic properties. Nowadays, keeping track to the Moore's law, semiconductor industry is moving towards small and complex 3D geometries to attain more devices per wafer. However, with the shift to devices with even more complex 3D geometries, conventional methods for generating metal silicide are no longer be the best choice because of the inhomogeneous coverage issue and surface roughness issue via the current self-aligned silicidation process.

Thus, this PhD thesis has aimed at developing a chemical colloidal approach for metal silicide layer, which is followed by the annealing process to optimize the electrical properties with applicable fabrication process. This thesis has successfully established the synthesis and characterization of nickel silicide layer using the metal precursor of  $\text{Ni(COD)}_2$  and  $\text{Ni[N(SiMe}_3\text{)(2,6-iPr}_2\text{C}_6\text{H}_3\text{)]}_2$  as well as the cobalt silicide layer using  $\text{Co}_2(\text{CO})_8$  as the metal precursor. The methodology used for this work focused on the one-pot reaction of the metal precursor and silane with the hydrogen-terminated Si wafer in toluene. After reaction, the as-synthesized layer has been investigated by the transmission electron microscopy and atomic force microscopy for the observation of layer thickness and surface roughness. Meanwhile, spectroscopic techniques, such as Fourier transform infrared spectroscopy, X-ray photoelectron spectroscopy, and X-ray absorption spectroscopy have also been conducted for the understanding of the chemical structure. The electrical property of the targeted layer has then been revealed by the I-V characteristics, which are measured by the four-point probe measurement.

Overall, this thesis has developed the new technique for the generation of metal silicide layer on the Si substrate, which is based on the chemical colloidal approach with the detailed characterizations. It has shown that the conformal metal silicide layer with low resistivity and low surface roughness could be obtained on the Si

wafer, leading a breakthrough of future semiconductor industry with the scalable process.

## **Zusammenfassung**

Die Verkleinerung von integrierten Schaltkreisen ist heutzutage eine zentrale Herausforderung für die Verbesserung von deren Leistungsfähigkeit. Moderne Transistoren mit komplexen Geometrien erreichen eine höhere Leistungsfähigkeit und Energieeffizienz und übertreffen damit die Grenzen im Nanobereich. Dieser Durchbruch bringt jedoch auch Verarbeitungsherausforderungen in jedem wichtigen Schritt der Herstellung von Hochleistungsgeräten mit sich. Metallsilizide, die für die Mikroelektronikindustrie von großem Interesse sind, werden üblicherweise in Stromhalbleitervorrichtungen als Kontakte zwischen Halbleitersubstrat und Metallleitungen verwendet, um die besten elektronischen Eigenschaften zu erzielen. Heute bedient sich die Halbleiterindustrie kleinen und komplexen 3D-Geometrien, um mehr Bauelemente pro Wafer zu erhalten und damit dem Moore'schen Gesetz zu folgen. Mit der Umstellung auf Geräte mit noch komplexeren 3D-Geometrien sind herkömmliche Verfahren zur Erzeugung von Metallsilizid jedoch nicht mehr die beste Wahl, da Probleme wie inhomogene Abdeckung und Oberflächenrauigkeit durch den aktuellen selbstjustierten Silizidierungsprozess auftreten.

Diese Dissertation befasst sich damit einen chemischen kolloidalen Herstellungsprozess für die Metallsilizidschicht zu entwickeln, an den sich der Glühprozess anschließt, um die elektrischen Eigenschaften mit dem Herstellungsprozess zu optimieren. Diese Dissertation beschreibt darüber hinaus auch die erfolgreiche Etablierung der Synthese und Charakterisierung der Nickelsilizidschicht unter Verwendung der Metallvorstufen  $\text{Ni}(\text{COD})_2$  und  $\text{Ni}[\text{N}(\text{SiMe}_3)(2,6\text{-iPr}_2\text{C}_6\text{H}_3)]_2$  sowie der Kobaltsilizidschicht mit  $\text{Co}_2(\text{CO})_8$  als Metallvorstufe. Die für diese Arbeit verwendete Methodik konzentrierte sich auf die Eintopfreaktion der Metallvorstufe und des Silans mit dem wasserstoffterminierten Si-Wafer in Toluol. Nach der Reaktion wurde die so synthetisierte Schicht mittels Transmissionselektronenmikroskopie und Rasterkraftmikroskopie zur Messung der Schichtdicke und Oberflächenrauigkeit untersucht. Zudem wurden auch spektroskopische Techniken wie Fourier-Transformations-Infrarotspektroskopie, Röntgen-Photoelektronenspektroskopie und Röntgenabsorptionsspektroskopie verwendet, um bessere Einblicke in die chemische Oberflächenstruktur zu erhalten. Die elektrischen Eigenschaften der synthetisierten Schicht wurden dann durch die I-V-Charakteristika, die durch Vierpunktsondenmessung gemessen wurden, untersucht.

Insgesamt wurde in dieser Arbeit eine neue Technik zur Erzeugung von Metallsilizidschichten auf einem Si-Substrat entwickelt, die auf dem chemischen kolloidalen Ansatz und detaillierten Charakterisierungen beruht. Es hat sich gezeigt, dass eine konforme Metallsilizidschicht mit niedrigem spezifischen Widerstand und geringer Oberflächenrauigkeit auf dem Si-Wafer erhalten werden kann, was zu einem Durchbruch für die Halbleiterindustrie mit einem skalierbaren Prozess führt.

# Chapter 1:

## Introduction

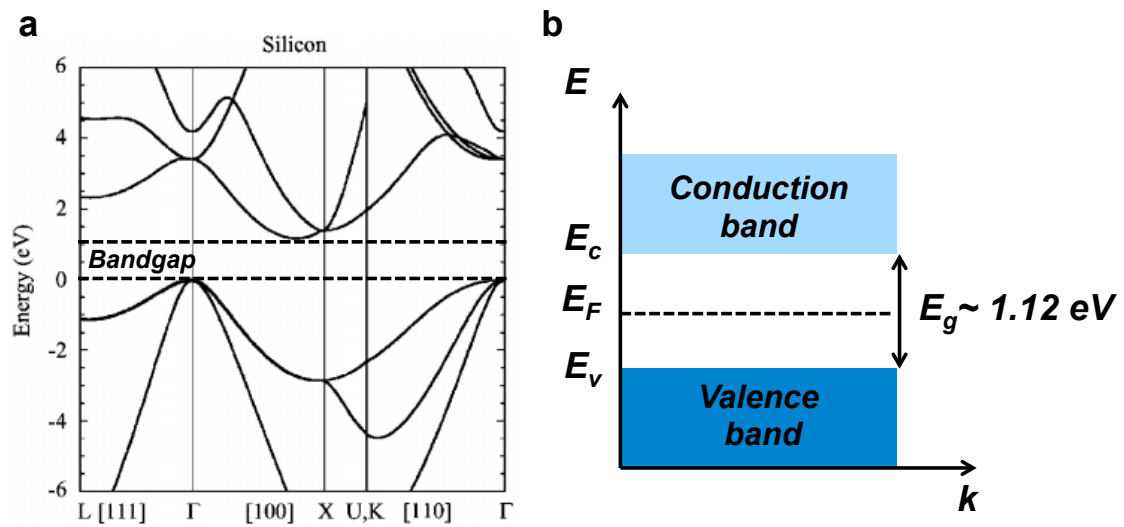
The semiconductor industry has grown steadily since 60's to become the \$400 billion economy<sup>1</sup> and has changed the world in terms of calculations, communication, and data processing. In the first quarter of 2018, the total semiconductor sales are \$111 billion, which are around 20% higher than the sales in 2017.<sup>2</sup> It implies that the semiconductor industry is still in great demand and keeps expanding significantly. To start with, semiconductor means the material with bandgap less than  $\sim 3$  eV.<sup>3</sup> When applying adequate current or voltage into it, the semiconductor shows the rectification property, allowing for the application related to rectifiers, amplifiers, sensors, etc. There are many different semiconductors' materials used in modern electronics, such as Si, Ge, GaAs, InP, and others.<sup>3</sup> Of these materials, Si-based semiconductor is the most commonly used in the industry with a well-developed fabrication system. Nowadays, most of electronic devices in our daily life are composed of various kinds of Si-based semiconductor devices for its operation. Among the whole processes of Si-based semiconductor fabrication, metal silicide formation serves as one of the most important steps for the high current efficiency in the device. However, conventional methods for metal silicide formation are limited to apply on the modern semiconductor 3D structures due to the poor coverage issue. Thus, in this thesis, we will focus on developing a new methodology of forming the metal silicide layer with desired conformality and electrical properties on the Si wafer. In the beginning, in order to have a better understanding of the semiconductor material, the definition of bandgap, electrons and holes, intrinsic and extrinsic semiconductors, and band bending will be described as follows.

### *1.1. Basics of Semiconductor*

#### *1.1.1. Energy Band Diagram (Bandgap)*

Si-Si bond is formed by the overlap of two  $sp^3$  hybrid orbitals of each Si atom, and each Si-Si bond possesses two spin-paired electrons as the orbital diagram. The valence band (VB) is composed of electrons in the overlapped bonding orbitals, while the conduction band (CB) contains electrons with higher energies from the overlapped anti-bonding orbitals. The energy difference between VB and CB is called bandgap, normally noted as  $E_g$ , which is known as the minimum energy for the electron in the

VB to be promoted to the CB. The calculated energy band diagram of bulk Si is shown in Figure 1.1a, for which the y-axis indicates the electron energy and the x-axis is assigned to the wavenumber. Generally, it is plotted with three parts, including CB, VB, and bandgap for easier understanding as shown in Figure 1.1b. Besides, there is another hypothetical energy level, e.g. Fermi level, lying between VB and CB, which is denoted as  $E_F$  in Figure 1.1b. The Fermi level is defined as the energy level, for which the probability of being occupied by electrons is 50%;<sup>4</sup> it lies in the middle of VB and CB in the case of intrinsic semiconductors (vide infra).



**Figure 1.1.** (a) Band diagram of bulk Si. Reproduced from the work of Richard et al.<sup>5</sup> (b) Schematic illustration of the energy band diagram of the intrinsic semiconductor. (copyright 2004 Physical Review B)

### 1.1.2. Electrons and Holes in Semiconductors

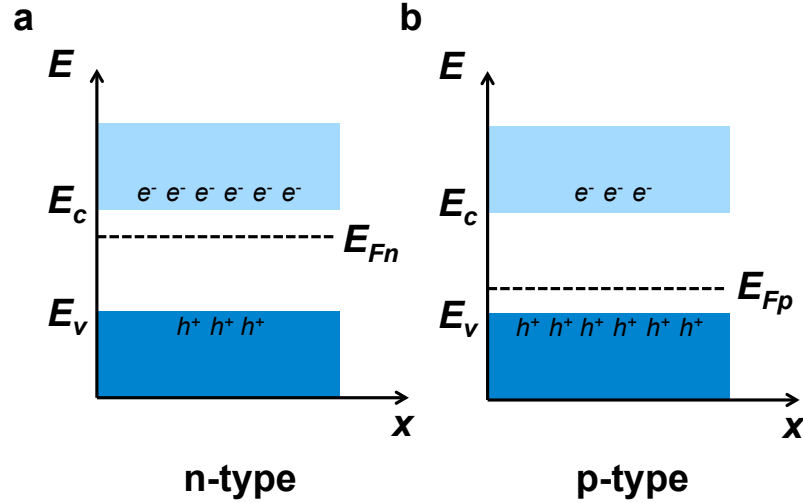
For an ideal crystal of Si, Si atoms are bonded together as a diamond structure without impurities and defects inside. The Si-Si bond would be broken if there is a sufficient thermal vibration energy from the environment, so that the free electron would be induced into the crystal. Meanwhile, the vacancy resulting from the missing electron is so-called “hole”, which is positively charged. The electrons and holes always appear in the form of the electron-hole pair, e.g. excitons, arising from the thermal vibration from the environment. When applying adequate electric field, the electron-hole pair could be separated, so that the electron and hole would wander around the crystal, inducing an electrical current in the material.

### ***1.1.3. Intrinsic Semiconductor***

An intrinsic semiconductor is a semiconductor material possessing equal amounts of electron and hole concentrations, e.g. no impurities in the crystal structure. In addition, the defects in the crystal might trap electrons and induce different concentrations of electrons and holes. As a result, an intrinsic semiconductor is also associated with a pure material with no defects in the crystal.

### ***1.1.4. Extrinsic Semiconductors***

Extrinsic semiconductors, however, are prepared by inserting a certain amount of impurity atoms into a pure Si crystal, e.g. dopant activation process, which leads to an increase in conductivity. For instance, adding phosphorus as impurities leads to a higher concentration of electrons than holes because this element has 5 valence electrons (one more than Si that can populate the conduction band). This kind of semiconductor is so-called n-type semiconductor, where “n-type” comes from the negative charge of electrons. On the other hand, when adding trivalent boron impurities, the concentration of holes becomes higher than this of electrons, which results in the higher probability for the holes to enter the valence band. The boron here acts as an acceptor and this semiconductor is a p-type semiconductor, for which “p-type” means positive charge of holes. The energy band diagrams of the n-type and p-type semiconductors are illustrated in Figure 1.2a and Figure 1.2b.

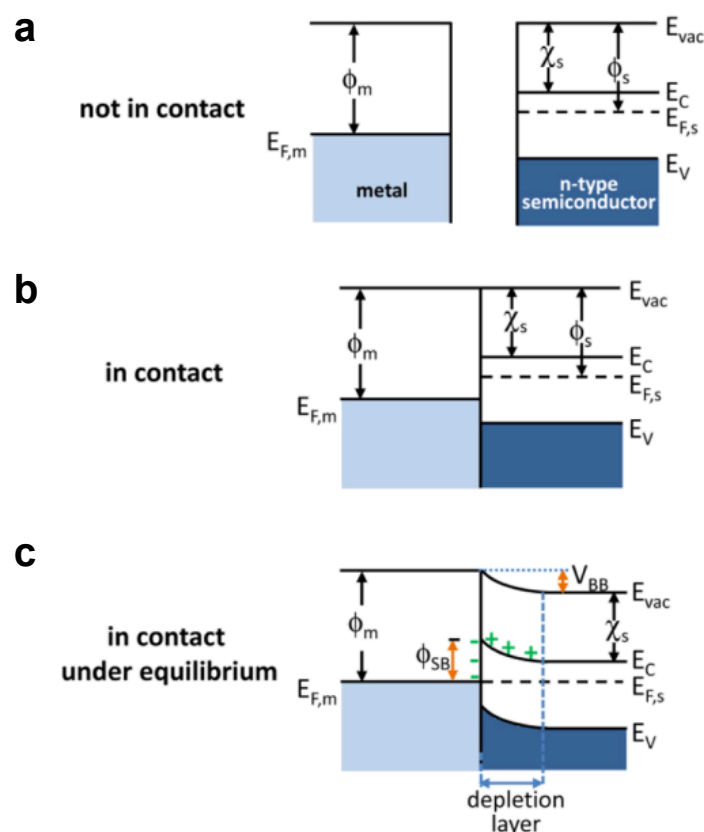


**Figure 1.2.** Schematic illustration of the energy band diagram of (a) n-type semiconductors and (b) p-type semiconductors.

#### 1.1.5. Band bending

In 1939, Schottky and Mott have first developed the concept of band bending for the explanation of the rectifying effect of the metal-semiconductor contacts.<sup>6</sup> In case of the contact between a n-type Si semiconductor and the a Cu metal wire, for which the work function is higher by  $\sim 0.63$  eV<sup>7</sup> as shown in Figure 1.3. The electron will transfer from the semiconductor to the metal until the alignment of Fermi levels of semiconductor and metal as shown in Figure 1.3c. This alignment of Fermi levels induces so-called band bending at the interface of metal and semiconductor with the energy barrier, e.g. Schottky barrier. Moreover, the band bending also exhibits in the contact of the p-type and n-type semiconductors, e.g. pn junction. The concept of pn junction provides the theoretical basis of the modern semiconductor devices, which are composed of several pn junctions in one semiconductor device, providing desired rectifying properties.



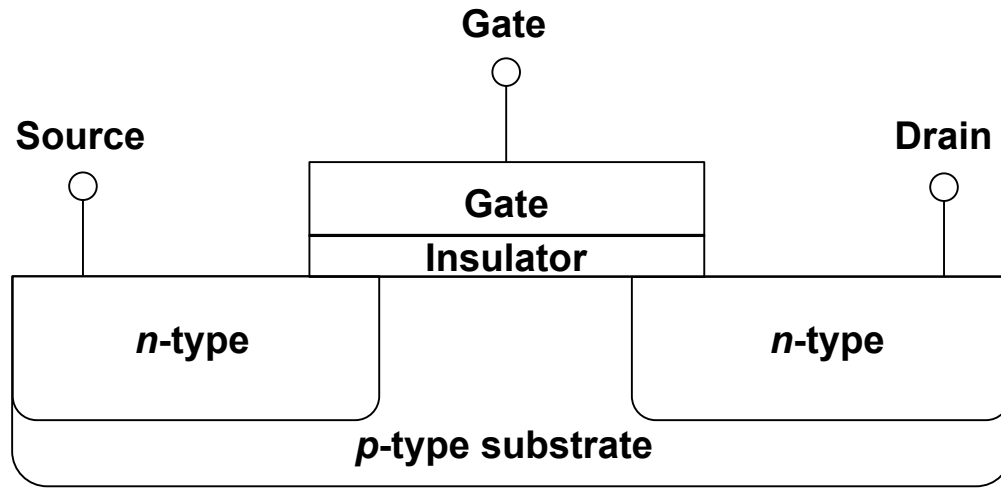


**Figure 1.3.** Energy band diagram of metal and n-type semiconductor contacts.  $E_{vac}$ , vacuum energy;  $E_c$ , energy of conduction band minimum;  $E_v$ , energy of valence band maximum;  $\phi_m$ , metal work function;  $\phi_s$ , semiconductor work function;  $\chi_s$ , electron affinity of the semiconductor. Reproduced from the work of Zhang and Yates, Jr.<sup>8</sup> (copyright 2012 Chemical Reviews)

## 1.2. Transistors

Generally, a transistor is composed of three terminals with a combination of n-type and p-type semiconductors as shown in Figure 1.4. When applying adequate voltages on the device, it would induce a responding current flow, e.g. the electronic signal, which can be then transferred out via the metal wire. It allows a weak signal to be amplified due to the capability to provide the voltage or current gains under operation. In addition, it can also be used as a switch for certain applications. Generally, there are two major types of transistors,<sup>4,9</sup> which are bipolar junction transistors (BJTs) and field effect transistors (FETs). Among them, FET has the advantage of fast switching speed and capability for being manufactured in a small volume, which is especially of great importance for the downscaling trend of modern integrated circuits. Thus,

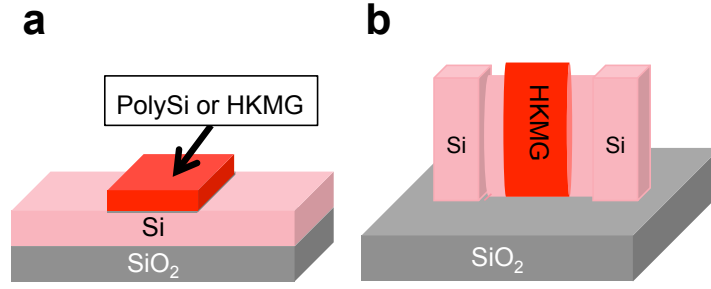
nowadays, most of the chips in the advanced electronic devices are composed of FETs, which are majorly metal oxide semiconductor FETs, namely MOSFETs (Figure 1.4).



**Figure 1.4.** Semiconductor structure of the n-channel MOSFET.

### ***1.3. Metal-Silicon Alloys in Microelectronics***

Since last four decades, metal silicon alloys, i.e., silicides, have grown as a fundamental material for the fabrication of smaller and faster semiconductor devices. They are often used to reduce the source, drain, and gate sheet resistances of submicron MOSFETs,<sup>10, 11</sup> and are nowadays mandatory in current technologies, such as fully-depleted silicon-on-insulator (FDSOI) FETs (Figure 1.5a) or FinFETs (Figure 1.5b).<sup>12, 13</sup> To increase the selectivity of highly-doped silicon contacts, silicides have been preferred to pure metals because of the stability of their contacts with Si and their self-passivating nature in an oxygen-rich environment.<sup>10</sup>



**Figure 1.5.** State-of-the-art device structures and beyond – (a) FDSOI FET – (b) FinFET –HKMG stands for High-K Metal Gate stack.

### 1.3.1. *Historical Development of Metal Silicide*

At the end of 1970s, the metallic silicides were introduced in microelectronics for the first time in order to improve the contact of MOS devices on the polysilicon gate.<sup>14</sup> MoSi<sub>2</sub> was the first metal silicide to be used (Polycidation process) and was replaced by WSi<sub>2</sub> since the 1980s, due to its lower resistivity (ca. 100  $\mu\Omega\cdot\text{cm}$  vs. ca. 70  $\mu\Omega\cdot\text{cm}$ ). However, the device miniaturization was followed by an increase in series resistance in the source and drain region. Metallic silicide layer with lower resistivity at both the gate / source and the drain regions was thus necessary to reduce the access resistance. Hence, the self-aligned silicidation process (Salicidation process) was then investigated and applied on the microelectronics during the 1990s for the preparation of sub-1 $\mu\text{m}$  technological nodes (vide infra for the introduction of Salicidation process).

### 1.3.2. *Titanium silicide*

Titanium silicide (TiSi<sub>2</sub>) was the first silicide applied on the transistors via the conventional self-aligned process as the C54 crystalline phase shows a low resistivity (10–15  $\mu\Omega\cdot\text{cm}$ ). The polymorphic transformation, required to form C54, is controlled by the nucleation of the grain boundaries. The nucleation becomes difficult when the dimensions of the silicide regions are scaled down.<sup>15</sup> For this reason, from 0.25  $\mu\text{m}$  nodes downwards, TiSi<sub>2</sub> was replaced by cobalt silicide (CoSi<sub>2</sub>) that has a lower resistivity and with less preparation issues.

### 1.3.3. *Cobalt Silicide*

Of all metal silicides, cobalt silicide has the lowest resistivity, and also exhibits thermal stability and high compatibility to Si substrate. However, limitations in the

use of cobalt silicide also appeared for devices smaller than 0.1  $\mu\text{m}$  using the conventional Salicidation process due to the consumption of large amounts of silicon upon the formation of  $\text{CoSi}_2$  (1 nm of Co consumes approximately 3.6 nm of Si to form  $\sim 3.5$  nm of  $\text{CoSi}_2$ <sup>16</sup>); this makes  $\text{CoSi}_2$  incompatible with the recent minimized devices with ultra-shallow junctions.

#### ***1.3.4. Nickel Silicide***

More recently, based on the Salicidation process, nickel silicide (NiSi) has become the silicide of reference for the 65 nm node for CMOS on planar silicon substrates,<sup>17</sup> such as bulk or SOI substrates.<sup>18</sup> Compared to its predecessors  $\text{TiSi}_2$  and  $\text{CoSi}_2$ , NiSi has many advantages: its formation does not consume much silicon after Salicidation process (1 nm of Ni consumes  $\sim 1.8$  nm of Si to form  $\sim 2.2$  nm of NiSi<sup>16</sup>) and it is formed at relatively low temperatures ( $\sim 350$ -500  $^\circ\text{C}$ ). Also, the resistivity of NiSi is similar to that of  $\text{CoSi}_2$  ( $\sim 15$ -20  $\mu\Omega\cdot\text{cm}$ ), so that based on the conventional processing methods, it remains the optimum metal silicide for the most advanced technologies nowadays.<sup>19</sup>

#### ***1.4. Salicidation Process for Metal Silicide***

Conventionally, metal silicide thin films are deposited using solid-state reactions of a metal species with silicon such as Physical Vapor Deposition (PVD), Chemical Vapor Deposition (CVD) and Atomic Layer Deposition (ALD), which have a common disadvantage of silicon consumption; other details of each method are described as below.

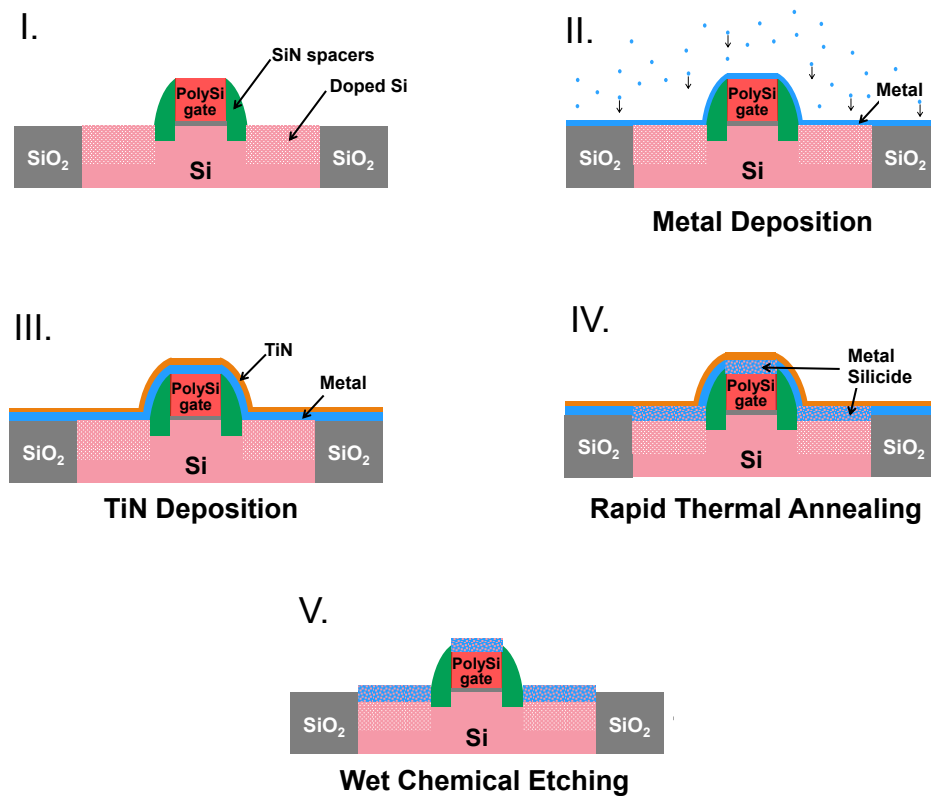
##### ***1.4.1. Standard Silicidation Technique : the self-aligned silicidation process (Salicidation process)***

As described above, the device miniaturization required lower resistivity of the drain and source contacts, which lead to the introduction of the salicidation process for sub- $1\mu\text{m}$  technological nodes during the 1990s. The main step of the process is the intrusion in the silicon of a metal that was previously deposited on the surface as illustrated in Figure 1.6.<sup>20</sup>

Metallic layers are generally deposited under vacuum at room temperature by PVD techniques such as sputtering or evaporation, CVD or nowadays magnetron sputtering (Figure 1.6 – steps I to II). The metallic thickness required for sub-65 nm technology

is less than or equal to a dozen nanometers. The metal sputtering is usually followed by the deposition of a titanium nitride-capping layer (TiN, Figure 1.6 – steps II to III). The TiN is formed to protect the metal layer from oxidization during the exposure to air that precedes the charging in the annealing equipment.

Then, the annealing step is performed by *Rapid Thermal Annealing* (RTA) technique under inert gas (Figure 1.6 – steps III to IV), for less than 120 s, and leads to the complete diffusion of metal into silicon to form metal silicide. The temperature for the RTA process is in the range of 500 °C to 900 °C, depending on the targeted phase of metal silicides. In the end, the TiN and remained metal layer would be removed via a wet chemical etching process (Figure 1.6 – steps IV to V), which is selective toward the metal silicide, leaving the targeted metal silicide on the surface.



**Figure 1.6.** Schematic diagrams of successive self-aligned silicidation process steps (Salicide) applied to a planar SOI MOS transistor.<sup>21</sup>

#### 1.4.2. Current Device Trends and Motivation for New Methodologies

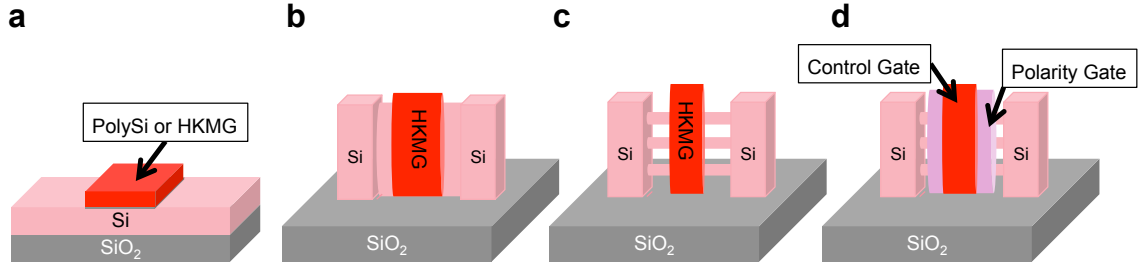
Nowadays, microelectronics industry is leveraging the use of complex 3D device geometries in order to provide a better electrostatic control over the channel. Indeed, ultra-thin and narrow channels are seen as the ideal architecture to handle the leakage

current at 22 nm technology node and below. Recently, novel tri-gate transistors using a fin shaped geometry (Figure 1.7b) have been proven to be capable of high volume manufacturing for high performance systems.<sup>22, 23</sup> As of previous structures, these devices exploit silicides at the source and drain contacts to minimize the access resistance. Nevertheless, the structure of these regions radically changed from planar to 3D-structure increasing the difficulty of a precise silicidation of the regions.

Such trend towards the reduction of device size is expected to go even further with transistors exploiting nanowires for the channel region.<sup>24, 25</sup> These devices are considered as the ultimate extension of FinFET transistors, as they exploit gate-all-around structure and 1D channel geometries (Figure 1.7c).

In recent years, Schottky-barrier FETs have been investigated as an alternative to conventional MOSFETs with doped source and drain contacts at ultimately scale.<sup>26</sup> Beyond the reduction of access resistances as compared to highly-doped silicon, using Schottky contacts can be useful to suppress variability arising from channel doping,<sup>27</sup> and induce a better control of the short channel effects (SCE) with atomically sharp junctions.<sup>28</sup> Moreover, the use of fully silicided source/drain regions appeared as a promising approach to reduce variability.<sup>29</sup> As a result, it is worthy pointing out that the silicide operation itself is source of variability with the current fabrication methods,<sup>18, 30-33</sup> therefore requiring special care on the film quality. The interest of Schottky contacts also applies on nanowires to provide better S/D regions.<sup>34</sup> Schottky-barrier nanowire transistors can also be grown vertically,<sup>35-37</sup> leading to new opportunities to realize logic operations within the metal layers of a chip.<sup>38</sup>

In order to further explore novel devices architectures with promising electrical properties, such as Tunnel FETs<sup>39</sup> or Controllable-Polarity FETs (Figure 1.7d),<sup>24, 40</sup> which are considered as the most promising to complement or even replace conventional MOSFETs. A common feature of these devices is the need for a precise electrostatic control over the channel, that involves complex geometries (Fin-based or Nanowire-based), coupled to a Schottky interface. In such a process, the need for a precise conformal silicide formation is especially crucial, as silicidation does not simply mean an enhancement of the device performance, but is now key in the device switching mechanism.



**Figure 1.7.** State-of-the-art device structures and beyond – (a) FDSOI FET – (b) FinFET – (c) Single-gate vertically-stacked nanowire FET – (d) Double-gate vertically stacked nanowire FET with controllable-polarity.

### 1.5. Thesis Objectives

Traditional routes for the realization of silicides on planar surfaces rely on an initial deposition of a metal layer whose conformality is limited by the step coverage of deposition processes such as sputtering or evaporation, e.g. Physical Vapor Deposition (PVD) methods. With the emergence of non-planar geometries in the recent years, the semiconductor industry was recently forced to develop new techniques to form silicides on complex geometries with high aspect ratio and ensure good deposition (and therefore silicidation) quality for current electronic devices and beyond.

Chemical Vapor Deposition (CVD) methods provide a solution for complex geometric concern because of the anisotropically deposition direction on the substrate. By CVD method, continuous gas flow containing vapor-phase chemical reactants is necessary so that high temperature is typically used to vaporize the metal precursor in the CVD chamber. The largest difference between PVD and CVD lies on the ability to form a homogeneous layer on the 3D structure. While PVD method provides Ni layers with good stability, the isotropic deposition is limiting when it comes to 3D-structures. On the other hand, CVD method benefits from gas-phase reaction, leading to an improvement of the layer aspect ratio. However, CVD method is typically carried out at relatively high temperature (ex:  $\sim 300$  °C for PECVD), which limits the choices of metal precursor.

As another alternative deposition technique, Atomic Layer Deposition (ALD) method is considered as one of the most promising methods to form a silicide layer in atomic level with controlled coverage ability. In contrast to CVD, the precursors in ALD are

inserted sequentially to form an atomic-level thin film.<sup>41-43</sup> While it shows promising results, as in CVD, the challenge of the thermal instability and the choice of molecular precursors, especially for Co and Ni, limits its usage.<sup>44</sup> Another approach proposes to use a plasma generated from a metal precursor to deposit a conformal metal-containing layer.<sup>45</sup> Finally, techniques based on different non-conformal deposition of materials can lead to conformal silicides. In particular, it has been proposed that by using a non-conformal diffusion barrier in conjunction with a similarly deposited non-conformal siliciding material, a substantially uniform and conformal silicide can be formed on a 3D structure such as FinFETs.<sup>46</sup>

Nevertheless, none of these techniques can be extended to more complex geometries that will be found in future devices such as vertically-stacked silicon nanowires.<sup>24, 25</sup> In this thesis, we aim at establishing an applicable technique for the silicidation of semiconductor devices with complex 3D geometries, by leveraging the interest of a chemical colloidal approach.

## **1.6. Strategy and Thesis Outline**

Recent studies on the preparation of colloidal nanoparticles have shown that it was possible to synthesize alloyed nanoparticles under the mild conditions (20-55 °C) using organometallic compounds as metal sources. A variety of nanoparticle structures and compositions have been indeed synthesized using this low temperature technique: various metals such as Pt,<sup>47-49</sup> Pd,<sup>50, 51</sup> Ru,<sup>52-54</sup> Ni,<sup>55</sup> Cu<sup>56</sup> and Au<sup>57</sup>, reacted with organo-Si or -Sn compounds. More specifically, amorphous nickel silicide (a-Ni<sub>3</sub>Si<sub>2</sub>) nanoparticles were obtained by reaction of a Ni(0) precursor with organosilane (RSiH<sub>3</sub>) at 55 °C.<sup>55</sup> In addition, using chemically similar Pt(0) and organotin precursors, crystalline Pt<sub>3</sub>Sn nanoparticles were even obtained at 20 °C.<sup>47</sup> Using the same approach, bimetallic PtPd alloys could also be readily prepared.<sup>51</sup> These findings opened new avenues to prepare metal silicide with the advantage of: (i) low temperature procedure (20-55 °C); (ii) possible conformal deposition of silicide on complex devices thanks to the liquid phase approach; (iii) the use of high purity and reasonable cost of the metal and silicon precursors; (iv) extension to cobalt silicides (CoSi<sub>x</sub>), which is not used anymore in industry due to the issue of Si consumption.



This thesis aims at developing an alternative approach to generate metal silicides using colloidal nanoparticles synthesis, with the goal to combine advantages mentioned above.

In chapter 2, a low-temperature colloidal approach by the reaction of  $\text{Ni(COD)}_2$  and  $\text{SiH}_4$  in toluene for the conformal nickel silicide layer on Si (100) wafer is developed. A 175-nm metal rich layer on Si (100) wafer was observed by electron microscopy (STEM-EDX), but XPS spectroscopy showed the presence of some carbon contamination. However, high temperature post-treatment leads to a decrease in carbon content and a lower surface roughness ( $R_{\text{rms}}=10.2$  nm) according to AFM, inducing a lower value of resistivity ( $\rho =170 \mu\Omega.\text{cm}$ ) measured by 4-point probe measurement. In addition to forming the  $\text{NiSi}_x$  layer onto the flat Si (100) surface, the method was applied to 3D-patterned wafers, in which the TEM results showed that a promising aspect ratio could be obtained.

In chapter 3, by utilizing the molecular-tailored Ni precursor, e.g.  $\text{Ni[N(SiMe}_3\text{)(2,6-}i\text{Pr}_2\text{C}_6\text{H}_3\text{)]}_2$ , in the colloidal approach, there is a uniform  $\text{NiSi}_x$  layer formed on the Si (100) wafer with a lower residual carbon contamination after reaction. However, it still shows typical Schottky characteristic from I-V measurement due to the embedded hydrocarbon ligands. After the post-treatment at high temperature under  $\text{H}_2$ , the I-V characteristic shows a combination of the Ohmic behaviour and Schottky behaviour based on the model fitting with the fitting value of resistivity of  $24 \mu\Omega.\text{cm}$ . Thus, it indicates that by using the Ni precursor with ligands that undergo cleaner decomposition, it is potential to obtain the conductive  $\text{NiSi}_x$  layer with a low amount of residual carbon.

In chapter 4, in parallel to the nickel silicide investigation, we have studied the application of this colloidal approach for another metal silicide deposition. Cobalt silicide is targeted in this chapter due to its lowest resistivity among all metal silicides. The reason why it is not widely used in the industry is due to high surface roughness, induced by the severe Si consumption during the conventional process. Using the colloidal approach, after reaction of  $\text{Co}_2(\text{CO})_8$  and  $\text{SiH}_4$  in toluene at low temperature, a 20-nm Co-rich layer on Si (100) wafer is observed by electron microscopy, and X-ray diffraction results indicate the formation of single crystalline  $\text{CoSi}_2$  with a low surface roughness ( $R_{\text{rms}}=5.3$  nm) after a thermal vacuum treatment ( $\sim 10^{-5}$  mbar). Then,

this layer exhibits a metallic conductive behavior (Ohmic behavior) with a low resistivity ( $\rho = 11.6 \mu\Omega\cdot\text{cm}$ ). Moreover, it shows a highly conformal cobalt silicide layer on the trench-structure even after the thermal vacuum treatment.

Overall, this work has established an alternative methodology to form metal silicide layers via the colloidal approach with the following advantages: (i) Direct metal silicide formation with lower surface roughness; (ii) Conformal and epitaxial deposition on 3D structure with desired electrical properties; (iii) Extension to cobalt silicide layer formation with a low resistivity.

### 1.7. References

1. Rosso, D. *Annual Semiconductor Sales Increase 21.6 Percent, Top \$400 Billion for First Time*; Semiconductor Industry Association: 5. Feb., 2018.
2. McGrath, D., Chip Sales Running 20% Above 2017 Pace. *Electronic Engineering Times* 3. May, 2018.
3. Kasap, S.; Capper, P.; Koughia, C., *Springer Handbook of Electronic and Photonic Materials*. Springer: 2006.
4. Kasap, S. O., *Principles of Electronic Materials and Devices*. McGraw-Hill: 2006.
5. Richard, S.; Aniel, F.; Fishman, G., Energy-band structure of Ge, Si, and GaAs: A thirty-band k-p method. *Phys. Rev. B* **2004**, 70 (23), 235204.
6. Schottky, W., Zur Halbleitertheorie der Sperrschicht- und Spitzengleichrichter. *Zeitschrift für Physik* **1939**, 113 (5), 367-414.
7. Kar, S., Determination of Si-metal work function differences by MOS capacitance technique. *Solid-State Electron.* **1975**, 18 (2), 169-181.
8. Zhang, Z.; Yates, J. T., Band Bending in Semiconductors: Chemical and Physical Consequences at Surfaces and Interfaces. *Chem. Rev.* **2012**, 112 (10), 5520-5551.
9. Chang, C. Y.; Sze, S. M., *ULSI Devices*. Wiley: 2000.
10. Murarka, S. P., *Silicides for VLSI Applications*. 1983.
11. Deng, F.; Johnson, R. A.; Asbeck, P. M.; Lau, S. S.; Dubbelday, W. B.; Hsiao, T.; Woo, J., Salicidation process using NiSi and its device application. *J. Appl. Phys.* **1997**, 81 (12), 8047-8051.
12. Kedzierski, J.; Meikei, I.; Kanarsky, T.; Ying, Z.; Wong, H. S. P., Fabrication of metal gated FinFETs through complete gate silicidation with Ni. *Electron Devices, IEEE Trans.* **2004**, 51 (12), 2115-2120.

13. Kuhn, K. J.; Avci, U.; Cappellani, A.; Giles, M. D.; Haverty, M.; Seiyon, K.; Kotlyar, R.; Manipatruni, S.; Nikonov, D.; Pawashe, C.; Radosavljevic, M.; Rios, R.; Shankar, S.; Vedula, R.; Chau, R.; Young, I. In *The ultimate CMOS device and beyond*, Electron Devices Meeting (IEDM), 2012 IEEE International, 10-13 Dec. 2012; 2012; pp 8.1.1-8.1.4.
14. Iwai, H.; Ohguro, T.; Ohmi, S.-i., NiSi salicide technology for scaled CMOS. *Microelectron. Eng.* **2002**, *60* (1), 157-169.
15. Gambino, J. P.; Colgan, E. G., Silicides and ohmic contacts. *Mater. Chem. and Phys.* **1998**, *52* (2), 99-146.
16. Maex, K.; van Rossum, M., *Properties of metal silicide (EMIS Data reviews)*. INSPEC: London, 1995; Vol. 14.
17. Froment, B.; Carron, V., Optimized Nickel Silicide Formation Process for High Performance Sub-65nm CMOS Nodes. In *Advanced short-time thermal processing for Si-based CMOS devices 2nd.; International Symposium*, PV, P.-E. s., Ed. ECS, , Pennington, NJ: : 2004; Vol. 1, pp 191-202.
18. Strane, J.; Brown, D.; Lavoie, C.; Suenaga, J.; Haran, B.; Press, P.; Besser, P.; Flaitz, P.; Gribelyuk, M.; Kammler, T.; Peidous, I.; Huajie, C.; Waidmann, S.; Frye, A.; DeHaven, P.; Domenicucci, A.; Murray, C.; Knarr, R.; Engelmann, H. J.; Streck, C.; Kahlert, V.; Deshpande, S.; Leobandung, E.; Pellerin, J.; Jagannathan, J. In *Implementation of Robust Nickel Alloy Salicide Process for High-Performance 65nm SOI CMOS Manufacturing*, VLSI Technology, Systems and Applications, 2007. VLSI-TSA 2007. International Symposium on, 23-25 April 2007; 2007; pp 1-2.
19. ITRS International Technology Roadmap for Semiconductors (ITRS).
20. Lau, C. K.; See, Y. C.; Scott, D. B.; Bridges, J. M.; Perna, S. M.; Davies, R. D., Titanium disilicide self-aligned source/drain+gate technology. *International Electron Devices Meeting. Technical Digest* **1982**, 714-717.
21. Le Tiec, Y., *Chemistry in Microelectronics*. ISTE Ltd: London, 2013.
22. Auth, C.; Allen, C.; Blattner, A.; Bergstrom, D.; Brazier, M.; Bost, M.; Buehler, M.; Chikarmane, V.; Ghani, T.; Glassman, T.; Grover, R.; Han, W.; Hanken, D.; Hattendorf, M.; Hentges, P.; Heussner, R.; Hicks, J.; Ingerly, D.; Jain, P.; Jaloviar, S.; James, R.; Jones, D.; Jopling, J.; Joshi, S.; Kenyon, C.; Liu, H.; McFadden, R.; McIntyre, B.; Neiryneck, J.; Parker, C.; Pipes, L.; Post, I.; Pradhan, S.; Prince, M.; Ramey, S.; Reynolds, T.; Roesler, J.; Sandford, J.; Seiple, J.; Smith, P.; Thomas, C.; Towner, D.; Troeger, T.; Weber, C.; Yashar, P.; Zawadzki, K.; Mistry, K. In *A 22nm*

*high performance and low-power CMOS technology featuring fully-depleted tri-gate transistors, self-aligned contacts and high density MIM capacitors*, VLSI Technology (VLSIT), 2012 Symposium on, 12-14 June 2012; 2012; pp 131-132.

23. Jan, C. H.; Bhattacharya, U.; Brain, R.; Choi, S. J.; Curello, G.; Gupta, G.; Hafez, W.; Jang, M.; Kang, M.; Komeyli, K.; Leo, T.; Nidhi, N.; Pan, L.; Park, J.; Phoa, K.; Rahman, A.; Staus, C.; Tashiro, H.; Tsai, C.; Vandervoorn, P.; Yang, L.; Yeh, J. Y.; Bai, P. In *A 22nm SoC platform technology featuring 3-D tri-gate and high-k/metal gate, optimized for ultra low power, high performance and high density SoC applications*, Electron Devices Meeting (IEDM), 2012 IEEE International, 10-13 Dec. 2012; 2012; pp 3.1.1-3.1.4.

24. De Marchi, M.; Sacchetto, D.; Frache, S.; Zhang, J.; Gaillardon, P.-E. J. M.; Leblebici, Y.; De Micheli, G., Polarity Control in Double-Gate, Gate-All-Around Vertically Stacked Silicon Nanowire FETs. In International Electron Devices Meeting (IEDM), San Francisco, California, USA, 2012.

25. Ernst, T.; Dupre, x; C.; Isheden, C.; Bernard, E.; Ritzenthaler, R.; Maffini-Alvaro, V.; Barbe, J. C.; De Crecy, F.; Toffoli, A.; Vizioz, C.; Borel, S.; Andrieu, F.; Delaye, V.; Lafond, D.; Rabille, G.; Hartmann, J. M.; Rivoire, M.; Guillaumot, B.; Suhm, A.; Rivallin, P.; Faynot, O.; Ghibaudo, G.; Deleonibus, S. In *Novel 3D integration process for highly scalable Nano-Beam stacked-channels GAA (NBG) FinFETs with HfO<sub>2</sub>/TiN gate stack*, Electron Devices Meeting, 2006. IEDM '06. International, 11-13 Dec. 2006; 2006; pp 1-4.

26. Knoch, J.; Min, Z.; Mantl, S.; Appenzeller, J., On the performance of single-gated ultrathin-body SOI Schottky-barrier MOSFETs. *Electron Devices, IEEE Trans.* **2006**, 53 (7), 1669-1674.

27. Weber, O.; Faynot, O.; Andrieu, F.; Buj-Dufournet, C.; Allain, F.; Scheiblin, P.; Foucher, J.; Daval, N.; Lafond, D.; Tosti, L.; Brevard, L.; Rozeau, O.; Fenouillet-Beranger, C.; Marin, M.; Boeuf, F.; Delprat, D.; Bourdelle, K.; Nguyen, B. Y.; Deleonibus, S. In *High immunity to threshold voltage variability in undoped ultra-thin FDSOI MOSFETs and its physical understanding*, Electron Devices Meeting, 2008. IEDM 2008. IEEE International, 15-17 Dec. 2008; 2008; pp 1-4.

28. Larson, J. M.; Snyder, J. P., Overview and status of metal S/D Schottky-barrier MOSFET technology. *Electron Devices, IEEE Trans.* **2006**, 53 (5), 1048-1058.

29. Hutin, L.; Vinet, M.; Poiroux, T.; Le Royer, C.; Previtali, B.; Vizioz, C.; Lafond, D.; Morand, Y.; Rivoire, M.; Nemouchi, F.; Carron, V.; Billon, T.; Deleonibus, S.;

- Faynot, O. In *Dual metallic source and drain integration on planar Single and Double Gate SOI CMOS down to 20nm: Performance and scalability assessment*, Electron Devices Meeting (IEDM), 2009 IEEE International, 7-9 Dec. 2009; 2009; pp 1-4.
30. Feste, S. F.; Zhang, M.; Knoch, J.; Zhang, S. L.; Mantl, S. In *Variability in SOI Schottky barrier MOSFETs*, Ultimate Integration of Silicon, 2008. ULIS 2008. 9th International Conference on, 12-14 March 2008; 2008; pp 27-30.
31. Min, Z.; Knoch, J.; Zhang, S.-L.; Feste, S.; Schroter, M.; Mantl, S., Threshold Voltage Variation in SOI Schottky-Barrier MOSFETs. *Electron Devices, IEEE Trans.* **2008**, 55 (3), 858-865.
32. Matsukawa, T.; Yongxun, L.; Endo, K.; Tsukada, J.; Ishikawa, Y.; Yamauchi, H.; O'Uchi, S.; Sakamoto, K.; Masahara, M., Variability Origins of Parasitic Resistance in FinFETs With Silicided Source/Drain. *Electron Device Lett., IEEE* **2012**, 33 (4), 474-476.
33. Seger, J.; Hellstrom, P. E.; Lu, J.; Malm, B. G.; von Haartman, M.; Ostling, M.; Zhang, S. L., Lateral encroachment of Ni-silicides in the source/drain regions on ultrathin silicon-on-insulator. *Appl. Phys. Lett.* **2005**, 86 (25), 253507-3.
34. Tan, E. J.; Pey, K. L.; Singh, N.; Lo, G. Q.; Chi, D. Z.; Chin, Y. K.; Tang, L. J.; Lee, P. S.; Ho, C. K. F., Nickel-Silicides Schottky Junction CMOS Transistors With Gate-All-Around Nanowire Channels. *Electron Device Lett., IEEE* **2008**, 26 (8).
35. Goldberger, J.; Hochbaum, A. I.; Fan, R.; Yang, P., Silicon Vertically Integrated Nanowire Field Effect Transistors. *Nano Lett.* **2006**, 6 (5), 973-977.
36. Schmidt, V.; Riel, H.; Senz, S.; Karg, S.; Riess, W.; Gösele, U., Realization of a Silicon Nanowire Vertical Surround-Gate Field-Effect Transistor. *Small* **2006**, 2 (1), 85-88.
37. Tomioka, K.; Yoshimura, M.; Fukui, T., A III-V nanowire channel on silicon for high-performance vertical transistors. *Nature* **2012**, 488 (7410), 189-192.
38. Gaillardon, P. E.; Ben-Jamaa, H.; Morel, P.; Noel, J.; Clermidy, F.; O'Connor, I. In *Can we go towards true 3-D architectures?*, Design Automation Conference (DAC), 2011 48th ACM/EDAC/IEEE, 5-9 June 2011; 2011; pp 282-283.
39. Leonelli, D.; Vandooren, A.; Rooyackers, R.; Verhulst, A. S.; De Gendt, S.; Heyns, M. M.; Groeseneken, G., Silicide Engineering to Boost Si Tunnel Transistor Drive Current. *Jpn. J. Appl. Phys.* **2011**, 50 (4).

40. Sacchetto, D.; Leblebici, Y.; De Micheli, G., Ambipolar Gate-Controllable SiNW FETs for Configurable Logic Circuits With Improved Expressive Capability. *IEEE Electron Device Lett.*, **IEEE** **2012**, *33* (2), 143-145.
41. Bernal-Ramos, K.; Saly, M. J.; Kanjolia, R. K.; Chabal, Y. J., Atomic Layer Deposition of Cobalt Silicide Thin Films Studied by in Situ Infrared Spectroscopy. *Chem. Mater.* **2015**, *27* (14), 4943-4949.
42. K.-M. Lee, C. Y. K., C. K. Choi, S.-W. Yun, J.-B. Ha, J.-H. Lee, and J. Y. Lee, Interface properties of nickel-silicide films deposited by using plasma-assisted atomic layer deposition. *J. Korean Phys. Soc.* **2009**, *55* (3), 1153-1157.
43. Kang, H.-S.; Ha, J.-B.; Lee, J.-H.; Choi, C. K.; Lee, J. Y.; Lee, K.-M., Effect of catalyst for nickel films for NiSi formation with improved interface roughness. *Thin Solid Films* **2011**, *519* (20), 6658-6661.
44. Kim, H., Atomic layer deposition of transition metals for silicide contact formation: Growth characteristics and silicidation. *Microelectron. Eng.* **2013**, *106* (0), 69-75.
45. Hasegawa, T.; Tada, K.; Yamasaki, H.; O'Meara, D. L.; Leusink, G. J. Method of forming conformal metal silicide films. U.S. patent 2013023303, **2013**.
46. Ozcan, A.; Lavoie, C. Forming uniform silicide on 3D structure. U.S. patent 20110001169, **2011**.
47. Boualleg, M.; Baudouin, D.; Basset, J.-M.; Bayard, F.; Candy, J.-P.; Jumas, J.-C.; Veyre, L.; Thieuleux, C., Unexpected, spontaneous and selective formation of colloidal Pt<sub>3</sub>Sn nanoparticles using organometallic Pt and Sn complexes. *Chem. Commun.* **2010**, *46* (26), 4722-4724.
48. Boualleg, M.; Basset, J. M.; Candy, J. P.; Delichere, P.; Pelzer, K.; Veyre, L.; Thieuleux, C., Regularly Distributed and Fully Accessible Pt Nanoparticles in Silica Pore Channels via the Controlled Growth of a Mesosstructured Matrix around Pt Colloids. *Chem. Mat.* **2009**, *21* (5), 775-777.
49. Boualleg, M.; Norsic, S.; Baudouin, D.; Reine, S.; Basset, J.-M.; Candy, J.-P.; Delichere, P.; Pelzer, K.; Veyre, L.; Thieuleux, C., Selective localisation of Pt nanoparticles in the pores/walls of an ordered oxide via hydrophobic/hydrophilic interactions: Application to the synthesis of highly active and well defined heterogeneous catalysts for hydrogenation reactions. *J. Catal.* **2011**, *284* (2), 184-193.
50. Boualleg, M., *PhD thesis, University of Lyon, France* **2010**, .
51. Laurent, P., *PhD thesis, University of Lyon, France* **2012**, .

52. Pan, C.; Pelzer, K.; Philippot, K.; Chaudret, B.; Dassenoy, F.; Lecante, P.; Casanove, M. J., Ligand-stabilized ruthenium nanoparticles: Synthesis, organization, and dynamics. *J. Am. Chem. Soc.* **2001**, *123* (31), 7584-7593.
53. Pelzer, K.; Candy, J. P.; Bergeret, G.; Basset, J. M., Ru nanoparticles stabilized by organosilane fragments: Influence of the initial Si/Ru ratio and thermal stability. *Eur. Phys. J. D* **2007**, *43* (1-3), 197-200.
54. Pelzer, K.; Laleu, B.; Lefebvre, F.; Philippot, K.; Chaudret, B.; Candy, J. P.; Basset, J. M., New Ru nanoparticles stabilized by organosilane fragments. *Chem. Mat.* **2004**, *16* (24), 4937-4941.
55. Baudouin, D.; Szeto, K. C.; Laurent, P.; De Mallmann, A.; Fenet, B.; Veyre, L.; Rodemerck, U.; Copéret, C.; Thieuleux, C., Nickel–Silicide Colloid Prepared under Mild Conditions as a Versatile Ni Precursor for More Efficient CO<sub>2</sub> Reforming of CH<sub>4</sub> Catalysts. *J. Am. Chem. Soc.* **2012**, *134* (51), 20624-20627.
56. Roussey, A., *PhD thesis, University of Lyon, France* **2011**, .
57. Boualleg, M.; Guillois, K.; Istria, B.; Burel, L.; Veyre, L.; Basset, J. M.; Thieuleux, C.; Caps, V., Highly efficient aerobic oxidation of alkenes over unsupported nanogold. *Chem. Commun.* **2010**, *46* (29), 5361-5363.

## **Chapter 2:**

# **Low Temperature Wet Conformal Nickel Silicide Deposition for Transistor Technology via a Molecular Approach**

Individual contributions:

Adapted from “T-H, Lin, T. Margossian, M. D. Marchi, M. Thammasack, D. Zemlyanov, S. Kumar, J. Jagielski, L. Zheng, C-J. Shih, R. Zenobi, G. D. Micheli, D. Baudouin, P-E. Gaillardon and C. Copéret, ACS Appl. Mater. Interfaces, 2017, 9, 4948-4955. ”

T-H. Lin, T. Margossian, P-E. Gaillardon and C. Copéret designed all experiments. T-H. Lin developed and characterized all materials. T-H. Lin, M. D. Marchi, and M. Thammasack prepared samples and conducted TEM-EDS analysis. D. Zemlyanov performed XPS analysis. S. Kumar conducted the Au electrode evaporation. L. Zheng carried out AFM analysis. All authors contribute to the scientific discussions.



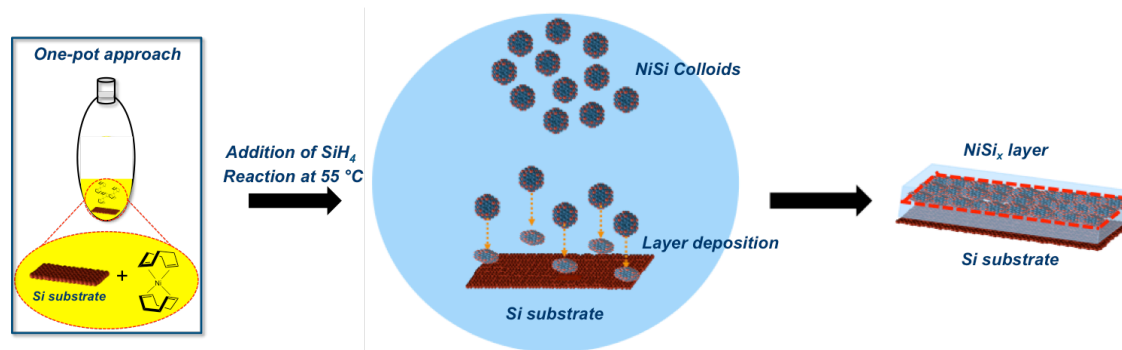
## 2.1. Introduction

For more than four decades, significant research efforts have been dedicated to the miniaturization of semiconductor devices in order to increase the amounts of transistors per  $\text{cm}^2$  and enhance the performance of integrated circuits<sup>1-5</sup> with gate lengths of modern transistor technologies going down to 14 nm.<sup>6-8</sup> This evolution, namely the fastest in the history of modern industries, has also revealed that, in the near future, Moore's law<sup>9</sup> would be strongly challenged for the concern about processing and fabrication of the device with gate length below 14 nm. Recently, complex device structures with 3D geometries<sup>2</sup> have established themselves as the solution for the advanced generations of semiconductor devices.

Forming metal silicides, which are indispensable materials involved in the fabrication of all field effect transistors,<sup>10, 11</sup> has been identified as one of the major steps in modern process flows to reduce the contact resistance of the source and drain regions. Of metal silicides, nickel silicide ( $\text{NiSi}_x$ ) is widely used by the industry because of its low resistivity, material compatibility, and good stability.<sup>12-15</sup> Several methods are employed to deposit nickel silicide thin films, which are generally formed using solid-state reactions of a metal species with silicon, such as *Physical Vapor Deposition* (PVD),<sup>13</sup> *Chemical Vapor Deposition* (CVD)<sup>16, 17</sup> and *Atomic Layer Deposition* (ALD).<sup>18</sup> However, with the shift to devices with even more complex 3D geometries,<sup>19</sup> conventional PVD method may no longer be the best choice for generating nickel silicide because of its lack of conformity leading to the formation of inhomogeneous layers.<sup>12</sup> CVD and ALD are more promising candidates owing to the better aspect ratio attained compared with PVD method. Nevertheless, many challenges come from the thermal instability of nickel molecular precursors in gas-phase reaction, which limits the choices.<sup>18, 20</sup>

Thus, forming homogeneous silicides in devices using complex 3D geometries is challenging by classical silicidation process. With this information in mind, we have investigated the use of an alternative technique based on a wet chemical deposition method towards conformal and homogeneous deposition. This methodology takes advantage of recent developments in nickel-based colloidal nanoparticles production as catalysts for reforming applications,<sup>21-23</sup> where  $\text{NiSi}_x$

colloids were obtained by reaction of Bis(1,5-cyclooctadiene)nickel(0) [Ni(COD)<sub>2</sub>] and octylsilane at 55 °C.<sup>24</sup> Here, acutely aware of the application to microelectronic device fabrication, octylsilane was replaced by silane (SiH<sub>4</sub>) in order to minimize the possible sources of organic contaminations in the layer. Based on this one-pot approach (Scheme 2.1), a homogeneous 200 nm Ni-rich layer was formed on the flat Si(100) substrate according to Transmission electron microscopy (TEM) equipped with *Energy Dispersive Spectroscopy* (EDS). The layer was characterized by X-ray photoelectron spectroscopy (XPS) and Atomic force microscopy (AFM), which showed the formation of a homogeneous Ni-rich film along with carbon deposit, that was mostly removed by annealing under H<sub>2</sub> flow to a level similar to what is found for the pristine Si wafer (< 9%). The annealing step generates NiSi<sub>2</sub> and an improvement of series resistance by 2 orders down to 8.5 Ω, or 170 μΩ.cm for resistivity. According to these results and the isotropic nature of wet deposition, the disclosed processing approach may offer a solution for conformal nickel silicide formation on Si devices with complex 3D geometries, which is vital for modern semiconductor technologies.

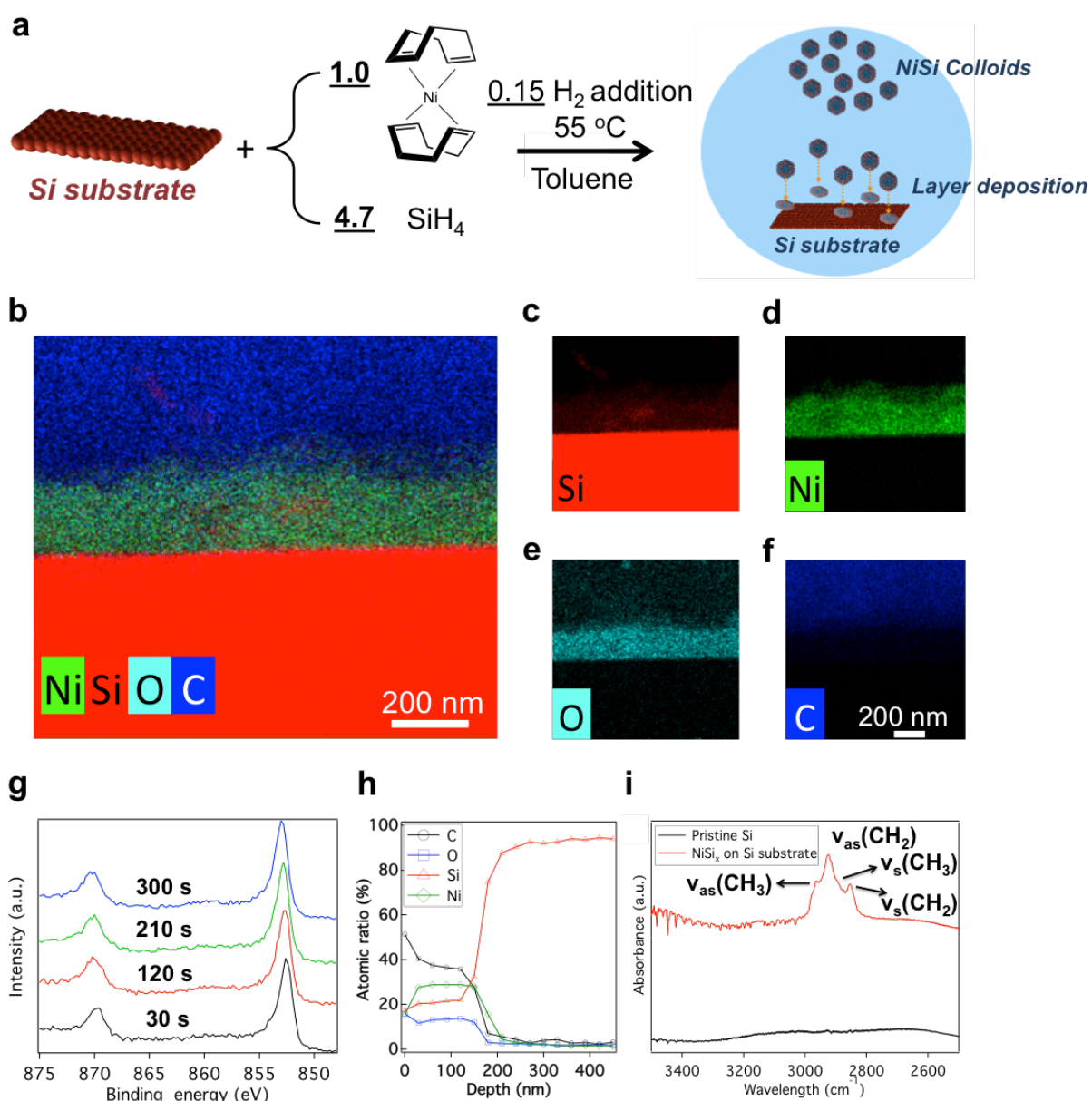


**Scheme 2.1.** Schematic representation of one-pot synthesis of NiSi<sub>x</sub> layer on Si substrate in this work.

## 2.2. Results and discussion

**NiSi<sub>x</sub> layer deposited on Si wafer by a chemical approach.** A 40% HF treated (100) Si wafer (Figure 2.1a) was immersed in a dry and degassed solution of 0.07 mmol Ni(COD)<sub>2</sub> in toluene. The air-tight container was then filled with 0.33 mmol SiH<sub>4</sub> and 0.01 mmol H<sub>2</sub> and let to react at 55 °C for 16 h under gentle stirring, yielding a homogeneous *ca.* 200 nm layer on top of the substrate along with a deep black

solution (Figure 2.1b). The film was characterized by *Energy-Dispersive X-ray Spectroscopy* (EDS) and XPS. Sample was exposed to air during transfers. EDS mapping shows that the layer contained Si (Figure 2.1c) and Ni (Figure 2.1d) along with oxygen (Figure 2.1e) and carbon (Figure 2.1f), *vide infra* for further discussions. The Ni core level was characterized by a binding energy around 853.2 eV, corresponding to the oxidized Ni ( $\text{Ni}^+$  or  $\text{Ni}^{2+}$ ) in the layer. In addition, the XPS depth profile (Figure 2.1h) shows the presence of carbon and oxygen (Si, Ni, C and O atomic ratio are averagely 23 at%, 28 at%, 36 at%, and 13 at% in the first 150 nm) in the Ni-rich layer, which is consistent with the observation from EDS mapping (Figure 2.1b). However, the major peak for Si 2p at 103.2 eV (Figure A.2.1) indicates that Si is partially oxidized in this layer, probably in the form of  $\text{NiSi}_x\text{O}_y$  formed upon exposure to air during the ex-situ transferring to the XPS chamber (see Appendix). To understand the origin of contaminations, the XPS analysis of a pristine wafer was conducted to serve as a background reference (Figure A.2.2). Its depth profile analysis shows that the average surface atomic ratio of oxygen is  $\sim 5$  at% (Table A.2.1), which is consistent with the formation of surface oxide. However, the surface atomic ratio of carbon on the pristine wafer is  $\sim 18$  at%, which is much less than in the as-synthesized thin film. It can hence be concluded that the presence of oxygen mainly results from the exposure to air during the ex-situ transferring to the XPS chamber, while carbon probably comes from the synthetic approach, as shown by transmission Fourier transform infrared spectroscopy (FTIR) carried out under inert conditions (Figure 2.1i). After the one-pot chemical reaction, signals of C-H bands were observed in the  $2800\text{-}3000\text{ cm}^{-1}$  region in agreement that the carbon contamination observed in XPS (single C 1s peak at 284.8 eV) was mostly present as alkyl groups. It probably originates from the hydrosilylation reaction of  $\text{SiH}_4$  and the olefinic group of the cyclooctadiene ligand of  $\text{Ni}(\text{COD})_2$ , which forms Si-C bonds.<sup>25</sup>

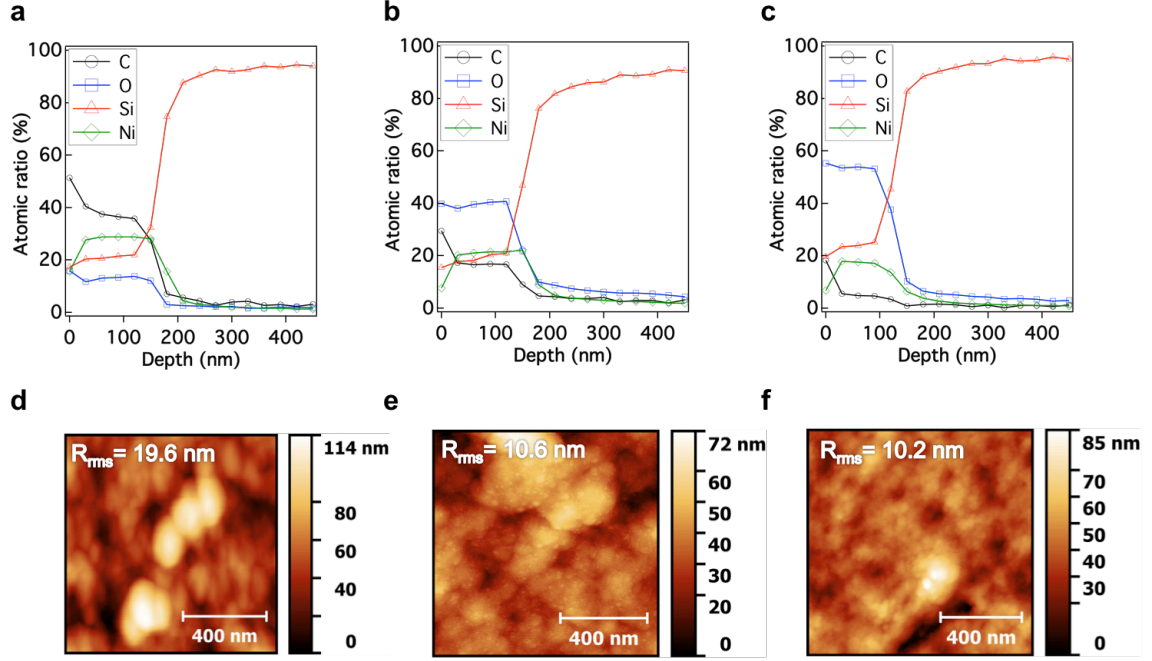


**Figure 2.1.** (a) Reaction scheme for one-pot synthesis, and the condition is as below:  $\text{Ni(COD)}_2/\text{die}$ ,  $110000 \text{ Ni.nm}^{-2}$ ,  $\text{SiH}_4/\text{Ni}=4.7$  with  $0.01 \text{ mmol H}_2$ , toluene,  $55^\circ \text{C}$  for 16 h. (b) EDS mapping image of the Ni-rich layer on the Si substrate. (c), (d), (e), (f) Si, Ni, O, and C EDS mapping images of the Ni-rich layer on the Si substrate, respectively. The wafer was exposed to air prior to EDS analysis. (g) X-ray photoelectron spectra of Ni 2p at different sputtering times, and (h) XPS depth profile quantization on the as-synthesized wafer. (i) Transmission FTIR spectra of the NiSi<sub>x</sub> layer on the as-synthesized wafer (red line), and the pristine Si wafer (black line).

**Annealing under H<sub>2</sub>.** Because of the presence of residual alkyl groups, a post-treatment under H<sub>2</sub> flow at high temperature was performed. After post-treatment, XPS depth profiling (Figure 2.2b and 2.2c) reveals that carbon amount decreased with increasing temperature of post-treatment; from 36 at% to 17 at% and 5 at% at 350 °C and 700 °C, respectively (Table 2.1). Worthy of note, after post-treatment at 700 °C, the amounts of carbon dropped down to ~5 at% which corresponds to the background level (Figure A.2.2a). In parallel, this layer became thinner (Figure 2.2c) and the Si/Ni ratio was increased from 0.8 to 1.8, consistent with the formation of NiSi<sub>2</sub> (*vide infra* for characterization of the layer). This change is resulted from the diffusion of Ni atoms into Si substrate along with Si atoms diffusing out at higher temperatures, thus inducing the phase transformation.<sup>14</sup> Note that there is a sharply increase of Si content with a decrease of Ni content in the interface (depth ~150 nm) for all samples, after which the values are associated with bulk Si substrate.

Concerning the presence of oxygen, it increases with increasing temperature of post-treatment and parallels the decrease amount of carbons. As discussed in the previous part, it is likely related to the oxidation of the layer upon transferring of the wafer to the XPS chamber.

To correlate this composition difference to surface morphology, AFM was conducted, which showed the value of root mean square roughness ( $R_{\text{rms}}$ ) of as-synthesized wafer is 19.6 nm (Figure 2.2d). However, samples after post-treatment showed  $R_{\text{rms}}$  equaled to 10.6 nm (Figure 2.2e) and 10.2 nm (Figure 2.2f) at 350 °C and 700 °C, respectively. Combined with XPS results, post-treatment under H<sub>2</sub> flow at high temperature effectively decreased the carbon amount down to the level similar with pristine Si wafer and allowed for the formation of a homogeneous NiSi<sub>2</sub>-like layer by the increasing Si/Ni ratio to 1.8 (Table 2.1), which will be further analyzed and proved by the X-ray absorption spectroscopy (XAS) on a model of Si(0) nanoparticles in the following part.



**Figure 2.2.** XPS depth profiles of Ni-rich layer on the Si substrate: (a) as-synthesized wafer; (b) wafer with post-treatment at 350 °C in H<sub>2</sub> flow; (c) wafer with post-treatment at 700 °C in H<sub>2</sub> flow. The atomic ratio was calculated in the first ~120 nm. AFM images of Ni-rich layer on the Si substrate: (d) as-synthesized wafer in the scale of 1  $\mu\text{m}^2$ ,  $R_{\text{rms}}$ =19.6 nm; (e) wafer with post-treatment at 350 °C in the scale of 1  $\mu\text{m}^2$ ,  $R_{\text{rms}}$ =10.6 nm; (f) wafer with post-treatment at 700 °C in the scale of 1  $\mu\text{m}^2$ ,  $R_{\text{rms}}$ =10.2 nm.

**Table 2.1.** Quantitative XPS depth profiles of Ni-rich layer on the Si substrate.

Condition	Nickel [at %]	Silicon [at %]	Carbon [at %]	Oxygen [at %]
As-syn <sup>a)</sup>	28	23	36	13
PO_350 <sup>b)</sup>	21	19	17	40
PO_700 <sup>c)</sup>	16	29	5	50

<sup>a)</sup>As-synthesized sample; <sup>b)</sup>sample after post-treatment at 350 °C; <sup>c)</sup>sample after post-treatment at 700 °C. All atomic ratios were averaged in the first 120 nm

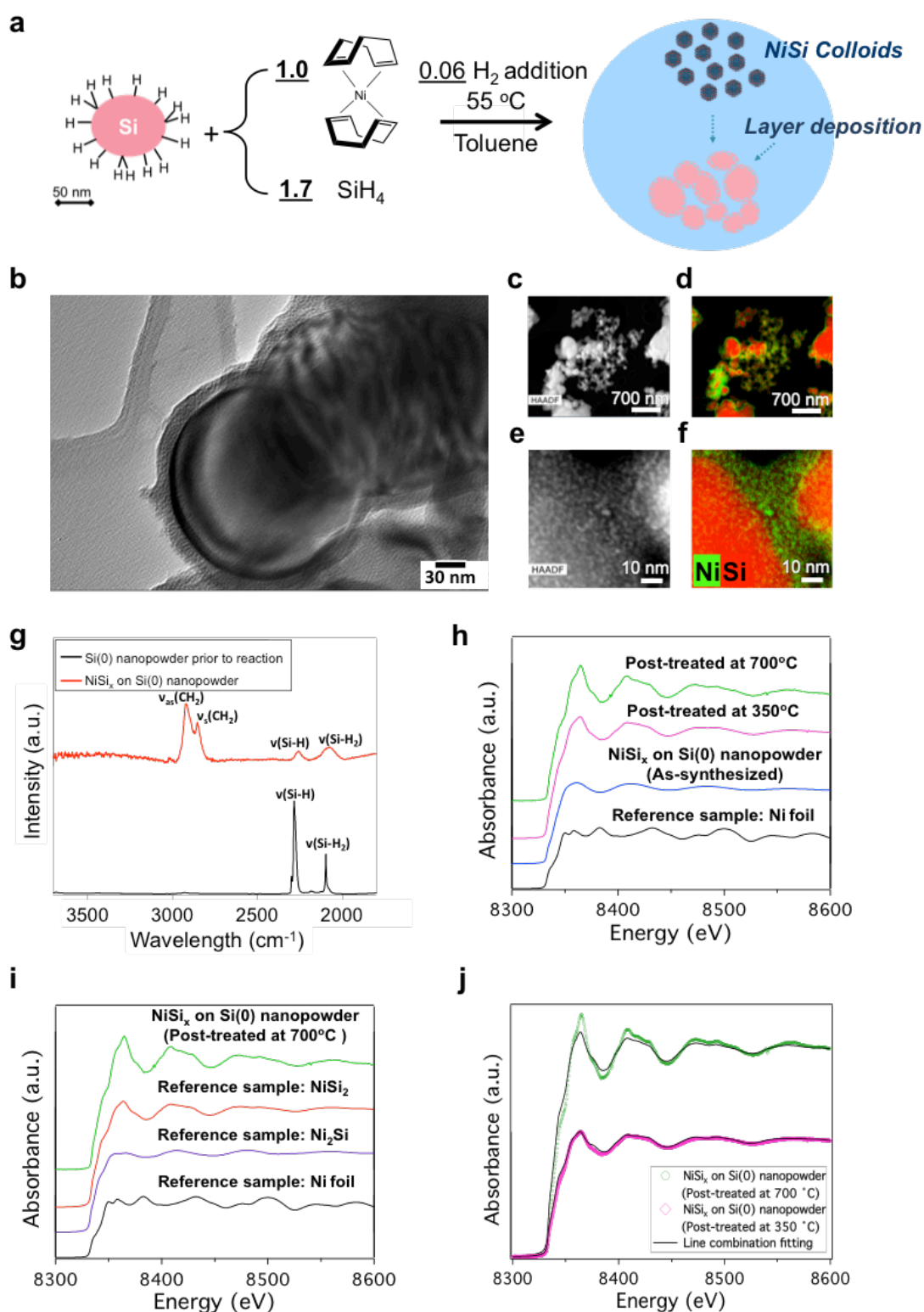
**Characterization of NiSi<sub>x</sub> layer using Si nanoparticles as a model.** In order to further clarify the nature of the layer on top of Si wafer, Si(0) nanoparticles were used as a model in order to broaden the surface characterization by FTIR<sup>26</sup> and XAS.

The one-pot chemical approach described above was used on Si(0) nanoparticles, which were previously treated at 900 °C under H<sub>2</sub> to provide a surface solely terminated by Si-H as for wafers (Figure A.2.3). The targeted surface Ni loading was lower than that for the wafer: 350 Ni.nm<sup>-2</sup> instead of 110'000 Ni.nm<sup>-2</sup>. The reaction of Ni(COD)<sub>2</sub> and SiH<sub>4</sub> with the addition of H<sub>2</sub> at 55 °C on the Si(0) nanoparticles (Figure 2.3a) also leads to the formation of a homogeneous layer throughout the surface of these spherical nanoparticles, whose thickness was ca. 15 nm according to high-resolution TEM (HRTEM) (Figure 2.3b). EDS mapping of high magnification (Figure 2.3f) showed this layer was composed of Ni and Si and covered on the entire surface of Si(0) nanoparticles, which was consistent with the layer formed on the Si wafer in the previous part. FTIR analysis was carried out on the as-synthesized sample after proper washing under inert condition and drying under high vacuum (~10<sup>-5</sup> mbar). While, before reaction, there is an intense peak at 2280 cm<sup>-1</sup> and 2100 cm<sup>-1</sup> associated with Si-H and Si-H<sub>2</sub> on top of the Si(0) nanoparticles (black line of Figure 2.3g), this band mostly disappears after the deposition of NiSi<sub>x</sub> (red line of Figure 2.3g), consistently with the consumption of the Si-H bonds. FTIR also showed that C-H signals appeared on the surface after reaction. These bands at 3000 cm<sup>-1</sup> to 2800 cm<sup>-1</sup> correspond to alkyl groups, which are presumably originated from the

COD ligand of  $\text{Ni}(\text{COD})_2$  and possibly through the hydrosilylation of COD.<sup>25</sup> Combined with HRTEM and EDS mapping images (Figure 2.3b, 2.3f), these data indicate that a homogeneous Ni-rich layer was formed on the surface of  $\text{Si}(0)$  nanoparticles. All the data are consistent with what is observed on wafers.

To understand the nature of the  $\text{NiSi}_x$  layer formed on the surface, Ni K-edge XAS was carried out under Ar, and the corresponding spectrum for as-synthesized Ni-rich layer on  $\text{Si}(0)$  nanopowder (blue curve, Figure 2.3h) presents significantly different constructive and destructive interferences compared with  $\text{Ni}(0)$  foil reference (black curve, Figure 2.3h). Combined with XPS results, the observed edge shift of 0.4 eV at the Ni K-edge with respect to  $\text{Ni}(0)$  foil indicates that this film is composed of  $\text{NiSi}_x$  instead of  $\text{Ni}(0)$ , and the energy shift is attributed to the charge redistribution for the  $\text{NiSi}_x$  formation.<sup>27</sup> For the samples after post-treatment at 350 and 700 °C (Figure 2.3h), the observed edge shifts are 0.9 eV and 1.8 eV with respect to  $\text{Ni}(0)$  foil, which revealed that the Ni went through the phase transformation to higher oxidative state. Furthermore, linear combination fitting of XAS was conducted on  $\text{NiSi}_x$  after 350 °C and 700 °C post-treatment and compared with the reference samples of  $\text{NiSi}_2$ ,  $\text{Ni}_2\text{Si}$ , and  $\text{Ni}(0)$  foil (Figure 2.3i, 2.3j). It showed that for the sample post-treated at 350 °C, the fit is consistent with the presence of ca. 95%  $\text{NiSi}_2$  and 5%  $\text{Ni}(0)$ ; while after post-treatment at 700 °C, the data perfectly fit to  $\text{NiSi}_2$  reference sample. The fitting results confirm the observation from previous XPS results (Figure 2.2) that phase transformation occurred during post-treatment and that this Ni-rich layer was mainly composed of  $\text{NiSi}_2$  after post-treatment at 700 °C.





**Figure 2.3.** (a) Reaction scheme of the one-pot synthesis for Ni-rich layer. (b) HRTEM analysis of  $\text{NiSi}_x$  on the  $\text{Si}(0)$  nanopowder ( $(\text{Ni}(\text{COD})_2)_{350}$   $\text{Ni}/\text{nm}^2$ ,  $\text{SiH}_4/\text{Ni}=1.7$ , toluene,  $55^\circ\text{C}$ , without post-treatment). (c) High-angle annular dark-field (HAADF) image of  $\text{NiSi}_x$  on the  $\text{Si}(0)$  nanopowder with (d) Ni and Si maps. (e)

Zoom-in HAADF image of NiSi<sub>x</sub> on the Si(0) nanopowder with (f) Ni and Si maps. (g) FTIR analysis of nanopowder: Black: Si(0) after H<sub>2</sub> regeneration; Red: NiSi<sub>x</sub> on the surface after one-pot synthesis. (h) X-ray absorption spectra of samples of NiSi<sub>x</sub> on Si(0) nanopowder and Ni (0) foil as the reference (black line). (i) X-ray absorption spectra of Si(0) nanopowder after 700 °C post-treatment and references. (j) Linear combination fitting of NiSi<sub>x</sub> on Si(0) nanopowder after 350 °C (pink curve) and 700 °C (green curve) post-treatment with the reference of Ni(0), NiSi<sub>2</sub>, and Ni<sub>2</sub>Si.

### **I-V characteristics of NiSi<sub>x</sub> on Si(100) wafer.**

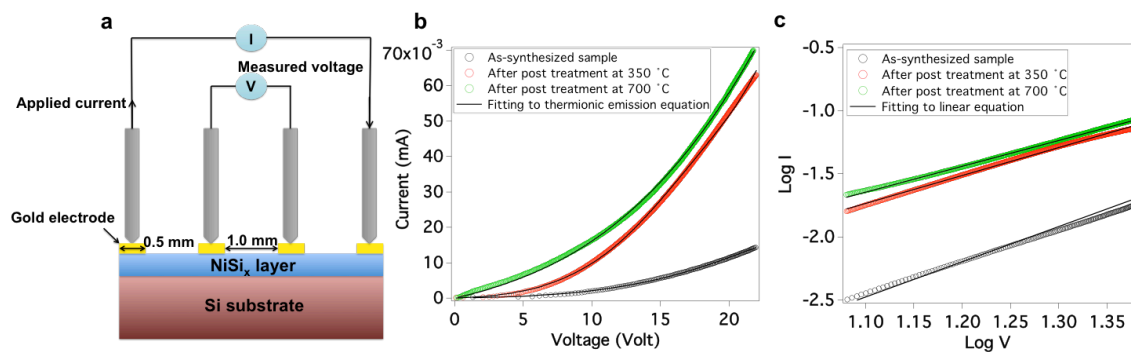
In order to gain insight into the NiSi<sub>x</sub> layer, the current (I) - voltage (V) characteristics were measured by the four-point probe setup, as shown in Figure 2.4a and I-V curve in Figure 2.4b. Rather than the Ohmic behavior, the I-V curve is reminiscent of a non-ideal diode, which suggests a Schottky barrier with the rectifying behavior in the layer, presumably resulted from the ensemble of junctions between the individual NiSi<sub>x</sub> nanoparticles (Figure A.2.4). Accordingly, the thermionic emission model (1)<sup>28,29</sup> was adopted to fit the positive part of I-V characteristics, given by:

$$I_a = AA_0 T^2 e^{-\frac{\Phi_n}{k_B T}} \left[ e^{-\frac{e_0(V - R_s I_a)}{\eta k_B T}} - 1 \right], \quad (1)$$

where  $I_a$  is applied current (A),  $V$  is measured voltage (V),  $A$  is active area ( $7.8 \times 10^{-7} \text{ m}^2$ ),  $A_0$  is effective Richardson constant ( $1.20 \times 10^6 \text{ A.m}^{-2}\text{K}^{-2}$ ),  $T$  is temperature of the junction (298K),  $k_B$  is the Boltzmann constant ( $8.62 \times 10^{-5} \text{ eV/K}$ ),  $\Phi_n$  is Schottky barrier height (eV),  $\eta$  is the ideality factor, and  $R_s$  is the series resistance ( $\Omega$ ). (See Appendix for calculation method)

For the as-synthesized sample, the fitted Schottky barrier height and the series resistance are 0.51 eV and 371.8  $\Omega$ , respectively, with the ideality factor of 157 (Table 2.2). Following the same fitting procedure, Schottky barrier heights after post-treatment at 350 and 700 °C significantly decrease to 0.49 and 0.41 eV; similarly, the series resistances decrease to 130.9 and 8.5  $\Omega$ . The ideality factors, on the other hand, remain within the same order of magnitude (107 and 394), indicating a non-ideal I-V behavior for NiSi<sub>2</sub> prepared by the chemical method. The higher barrier and series resistance of as-synthesized wafer are probably resulted from the presence of organic residue and the amorphous layer formed by the chemical method. The post-treatment

at high temperature eliminates the organic residues, decreases the carbon content and improves surface roughness as shown by the XPS and AFM results (Figure 2.2), thus allowing a lower series resistance down to  $8.5 \Omega$  ( $170 \mu\Omega\cdot\text{cm}$  for resistivity). However, compared with the reported resistivity of  $\text{NiSi}_2$  layer by CVD method ( $36 \mu\Omega\cdot\text{cm}$ ),<sup>11</sup> the higher resistivity and ideality factor suggest the presence of more resistive domains, possibly voids, between  $\text{NiSi}_2$  nanoparticles, resulted from the removal of carbon contamination and the diffusion of Ni atoms by the post-treatment. This phenomenon can be also evidenced by the XPS depth profile (Figure 2.2a-2.2c). After post-treatment at 350 and 700 °C, the oxygen ratio increases from 13% to 40% and 50%, respectively (Figure 2.2b and 2.2c). However, voids are formed upon removal of carbon contamination (carbon content decreases from 36 at% to 5 at%), allowing more oxygen to diffuse in this layer. In the same time, due to the diffusion of Ni atoms into the substrate (Ni content decrease from 28 at% to 16 at%), the layer becomes thinner with more voids, as shown by the TEM-EDS mapping image (Figure A.2.5). Thus, the  $\text{NiSi}_2$  layer is composed of the intercalation of nanoparticles as electron traps and resistive domains, in which the current conduction comes from charges jumping over barriers in between these nanoparticles. This is corroborated by the behavior of space charge limited current, proved by the ratio of  $\text{Log } I / \text{Log } V$  is close to 2 in Figure 2.4c,<sup>30</sup> which leads to an overall higher resistance and ideality factor of the  $\text{NiSi}_2$  material prepared by the chemical method.



**Figure 2.4.** (a) Schematic device for the four-point probe measurement (b) I-V characteristics of  $\text{NiSi}_x$  layer on the Si(100) wafer fitting to thermionic emission equation. Black circles: As-synthesized wafer; red circles: sample after 350 °C post-treatment; green circles: sample after 700 °C post-treatment; black lines: thermionic

emission equation fitting curves. (c) The logarithmic plots are acquired by the I-V curve in Figure 4 (b) and fitted to a linear equation.

**Table 2.2.** I-V characteristics of NiSi<sub>x</sub> on the Si(100) wafer

Condition	$\Phi_n$ [eV]	$R_s$ [ $\Omega$ ]	$\eta$	Log I/ Log V
As-syn <sup>a)</sup>	0.51	371.8	156.7	2.8
PO_350 <sup>b)</sup>	0.49	130.9	106.7	2.2
PO_700 <sup>c)</sup>	0.41	8.5	393.8	2.1

<sup>a)</sup>As-synthesized sample; <sup>b)</sup>sample after post-treatment at 350 °C; <sup>c)</sup>sample after post-treatment at 700 °C

### 2.3. Conclusion

In this study, a one-pot chemical approach was developed to deposit NiSi<sub>2</sub> layer on Si wafer with competitive Schottky barrier and resistivity. This NiSi<sub>2</sub> layer was formed in two steps through (1) the formation of a homogeneous nickel silicide layer upon reaction of Ni(COD)<sub>2</sub> and SiH<sub>4</sub> with the wafer surface at low temperature, here 55 °C, followed by (2) a post-treatment under H<sub>2</sub> at 700 °C yielding a NiSi<sub>2</sub> layer according to XPS and XAS analysis. This post-treatment removes organic residues and allows a lower Schottky barrier of 0.41 eV and resistivity of 170  $\mu\Omega$ .cm. Furthermore, using trenched Si wafer and the same one-pot synthetic approach (Figure A.2.6), TEM-EDS mapping of the as-synthesized sample shows the deposition of an homogeneous layer on top of the trenched structure with the step coverage of 0.74, which is comparable to what is obtain by CVD method, thus showing that this method can be applied on more complex structure. In summary, this method provides another route for the deposition of metal silicide at low temperature, and it has the advantage to be easily applied to 3D structures by conformal deposition on state-of-the-art semiconductor devices.

## 2.4. Experimental details

**General information.** The experiments were carried out by Schlenk techniques and in a mBraun LABstar glovebox under argon atmosphere. Toluene was dried and collected using a mBraun SBS-800 purification system and degassed by Schlenk techniques (vacuum to  $10^{-1}$  mbar and sparge with dry Ar for 10 times). 40% HF solution was purchased from VWR. Si(0) nanopowder was purchased from US-nano with the size between 20-30 nm and with 98% purity. Ni(COD)<sub>2</sub> were purchased from Strem and used as received. 1% SiH<sub>4</sub> (N5.0) in helium was purchased from PanGas. Pure H<sub>2</sub> (N5.0) gas was also purchased from PanGas. Every glassware was oven-dried for at least 4 h prior to use at temperatures greater than 150 °C.

**Nickel silicide colloidal nanoparticle synthesis on Si wafer (One-pot synthesis).** Double-side polished p-type 4" Si wafers with (100) orientations were diced into 2 cm × 1 cm dies and cleaned by 40% HF solution for 60 s. The diced wafers were then dried under high vacuum ( $\sim 10^{-5}$  mbar) at room temperature for 12 h.

A HF-treated diced Si-wafer and 20 mg Ni(COD)<sub>2</sub> (0.07 mmol) were placed in a 325 mL Fischer-Porter bottle in a glovebox and dissolved in toluene (10 mL). The reactor was then pressurized under 2.7 bars of 1% SiH<sub>4</sub> in He (0.33 mmol). Then, 2.7 bars of 1% SiH<sub>4</sub> (0.33 mmol) were put into the reactor at room temperature and 0.01 mmol H<sub>2</sub> were put in the reactor and heated to 55 °C for 16 h, during which a layer was formed on top of the Si-wafer accompanied by a dark solution (colloids formation). The colloidal solution was cannulated out of the reactor and the Si-wafer was washed 2 times with 10 mL of toluene. Prior storage inside glovebox, the as-synthesized wafer was dried under vacuum ( $\sim 10^{-2}$  mbar) for 3 h.

**Nickel silicide colloidal nanoparticle synthesis on Si(0) nanopowder (One-pot synthesis).** First, Si(0) nanopowders were treated with 900 °C in H<sub>2</sub> flow for 12 h to remove the surface silica and regenerate Si-H bond on it (Figure A.2.3).

Secondly, 50 mg of Si(0) nanopowders and 73 mg Ni(COD)<sub>2</sub> (0.27 mmol) were put in the 325 mL reactor in the glovebox. Then, the reactor was connected with Schlenk line and 10 mL toluene was injected into the reactor at room temperature until all Ni(COD)<sub>2</sub> were dissolved under stirring. Then, 3.5 bars of 1% SiH<sub>4</sub> (0.45 mmol) were put into the reactor under room temperature and 0.01 mmol H<sub>2</sub> were put in the reactor.

After that, the temperature was raised to 55 °C. After 16 h, the solution was composed of dispersed silicon nanopowders and black colloidal solution (sub-10nm nanoparticles). The reactor was transferred into the glovebox and the silicon nanopowders were washed with 10 mL of dry toluene and filtered for 3 times. Then, the as-synthesized nanopowders were dried in high vacuum ( $\sim 10^{-5}$  mbar) for 3 h.

**Post-treatment condition.** As-synthesized wafer/nanopowders was treated at high temperature (350 °C or 700 °C) under pure H<sub>2</sub> flow at 950 mbar for 12 h.

**Characterization Techniques.** TEM and EDS images were taken with a FEI Tecnai Orisis ultrahigh vacuum transmission electron microscope. The AFM measurements were conducted on a commercial AFM system (BioScope Catalyst, Bruker Nano, Santa Barbara, California) that is mounted onto an inverted confocal laser-scanning microscope (FluoView FV500, Olympus, Center Valley, Pennsylvania). The images shown in this study were obtained using tapping mode AFM with CT300R-25 cantilever probes (Nanoscience, USA). The AFM images are 1  $\mu\text{m}$  in size, with a resolution of  $256 \times 256$  pixels, and a scan rate of 0.2 Hz. FTIR spectra of wafers were recorded in transmission mode on Thermo Scientific, Nicolet 6700, in which the measurements were performed under inert condition with a deuterated triglycine sulfate (DTGS) detector with 1000 averaged scans to achieve an optimal signal-to-noise ratio. FTIR spectra of nanopowders were recorded in transmission mode on a Bruker ALPHA-T FTIR spectrophotometer under inert condition.

XPS depth profiles were obtained using a Kratos Axis Ultra DLD spectrometer with monochromic Al K $\alpha$  radiation (1486.6 eV). A commercial Kratos charge neutralizer was used to avoid non-homogeneous electric charge and to achieve better resolution. The resolution measured as full width at half maximum of the curve fitted photoemission peaks was approximately 1 eV. Binding energy (BE) values refer to the Fermi edge and the energy scale was calibrated using Au 4f<sub>7/2</sub> at 84.0 eV and Cu 2p<sub>3/2</sub> at 932.67 eV. Samples were attached to a stainless steel sample holder bar using a double-sided sticking Cu tape. XPS data were analyzed with CasaXPS software version 2313 Dev64 ([www.casaxps.com](http://www.casaxps.com)). The C-C component of the C 1s peak was set to a binding energy of 284.8 eV to correct for charge on each sample. Curve-fitting was performed following a linear or Shirley background subtraction using Gaussian/Lorentzian peak shapes. The atomic concentrations of the elements in the

near-surface region were estimated taking into account the corresponding Scofield atomic sensitivity factors and inelastic mean free path (IMFP) of photoelectrons using standard procedures in the CasaXPS software. Depth profiling was conducted by step by step sputtering of a sample with a Kratos polyatomic sputtering gun operating in Ar mode at 5 keV,  $I_{\text{ion}} \approx 1 \mu\text{A}$ . Thickness of the layers was calibrated using the TEM measured thickness.

Ni 2p and Si 2p XPS spectra were acquired by an ESCA KRATOS AXIS ULTRA, which were performed using a monochromatic Al  $K_{\alpha}$  (1486.6 eV) X-ray source (chamber under high vacuum). XPS spectra were fitted by the Gaussian-Lorentzian function after subtraction of baseline (Shirley baseline).

XAS data were carried out at the X10DA (Super XAS) beamline at the Swiss Light Source, Villigen, Switzerland. Spectra were collected on pressed pellets optimized to 1 absorption length at the Ni K-edge in transmission mode. The beamline energy axis was calibrated with a Ni reference foil, in which energies are measured at the inflexion point(s) of the absorption signal, and the precision on the energy of the edge is  $\pm 0.5$  eV in the (8303-8373 eV) area. The spectra were background-corrected using the Athena software package. Linear combination fits were performed by the routine of Athena software<sup>31</sup> over the range of 8300 to 8600 eV using reference spectra of Ni(0) foil, Ni<sub>2</sub>Si, and NiSi<sub>2</sub>.

For four-point probe measurement, four 100 nm gold (Au) electrodes were evaporated to a circle-shape layer (0.25 mm in radius; separate with each one by 1 mm) with a deposition rate of  $5 \pm 2 \text{ \AA} \cdot \text{s}^{-1}$  by thermal evaporation of Au ingots under high vacuum ( $\sim 10^{-5}$  mbar). The Au ingots (99.999%) were supplied by Kurt J. Lesker. A MBraun glovebox integrated MBraun vacuum thermal evaporator was used for the Au evaporation. The probe station used for I-V characteristic measurement is a Signatone S1160, and the I-V data were acquired by a Keysight B1500 with B1510A High Power source/monitor unit (HPSMU).

### **TEM sample preparation by tripod method**

The as-synthesized wafer was cleaved into two pieces of  $2.5 \times 1.8$  mm. These 2 pieces were then glued face-to-face with a Gatan G2 epoxy glue, in which the face to be observed was in the middle.

The procedure to complete polishing had two steps. First, the specimen was mounted on the side of a tripod polisher using Quickstick at 100 °C. A polishing of one side to remove most of the bulk materials was processed by a series of plastic diamond lapping films, with grains of decreasing sizes (30 µm, 15 µm, 6 µm, 1 µm, 0.5 µm, and 0.1 µm) and a final step was done on a soft felt covered disc impregnated with silica of 25 nm grain size.

Secondly, the specimen was mounted on the bottom of a tripod polisher using Quickstick at 100 °C. In this step, the glass support has to be perfectly flat polished to ensure a correct 0.6° angle of the wedge shape of the specimen. The flat polishing of the glass also prevented from bubble formation in the Quickstick that would break the specimen when the thickness is down to 100 nm. Also, this step was processed by a series of plastic diamond lapping films, with grains of decreasing sizes (30 µm, 15 µm, 6 µm, 1 µm, 0.5 µm, and 0.1 µm) and a final step was done on a soft felt covered disc impregnated with silica of 25 nm grain size. The specimen is ready when interference fringes can be observed on it, proving its electron transparency.

Finally, the specimen was glued on a Mo grid with a diameter adapted to the holder of the microscope. After one night of drying, the grid was detached from the tripod using acetone to dissolve the Quickstick, and the specimen was cleaned by acetone.

## 2.5. References

1. Hisamoto, D.; Wen-Chin, L.; Kedzierski, J.; Takeuchi, H.; Asano, K.; Kuo, C.; Anderson, E.; Tsu-Jae, K.; Bokor, J.; Chenming, H., FinFET-a self-aligned double-gate MOSFET scalable to 20 nm. *IEEE Tran. Electron Devices* **2000**, *47* (12), 2320-2325.
2. Jung-Suk, G.; Qi, X.; Takamura, Y.; Haihong, W.; Pan, J.; Arasnia, F.; Paton, E. N.; Besser, P.; Sidorov, M. V.; Adem, E.; Lochtefeld, A.; Braithwaite, G.; Currie, M. T.; Hammond, R.; Bulsara, M. T.; Ming-Ren, L., Scalability of strained-Si nMOSFETs down to 25 nm gate length. *IEEE Electron Device Lett.* **2003**, *24* (5), 351-353.
3. Iwai, H., Roadmap for 22 nm and beyond. *Microelectron. Eng.* **2009**, *86* (7–9), 1520-1528.
4. Ng, H. T.; Han, J.; Yamada, T.; Nguyen, P.; Chen, Y. P.; Meyyappan, M., Single Crystal Nanowire Vertical Surround-Gate Field-Effect Transistor. *Nano Lett.* **2004**, *4* (7), 1247-1252.



5. Xiang, J.; Lu, W.; Hu, Y.; Wu, Y.; Yan, H.; Lieber, C. M., Ge/Si nanowire heterostructures as high-performance field-effect transistors. *Nature* **2006**, *441* (7092), 489-493.
6. Lin, C. H.; Greene, B.; Narasimha, S.; Cai, J.; Bryant, A.; Radens, C.; Narayanan, V.; Linder, B.; Ho, H.; Aiyar, A.; Alptekin, E.; An, J. J.; Aquilino, M.; Bao, R.; Basker, V.; Breil, N.; Brodsky, M.; Chang, W.; Clevenger, L.; Chidambarrao, D.; Christiansen, C.; Conklin, D.; DeWan, C.; Dong, H.; Economikos, L.; Engel, B.; Fang, S.; Ferrer, D.; Friedman, A.; Gabor, A.; Guarin, F.; Guan, X.; Hasanuzzaman, M.; Hong, J.; Hoyos, D.; Jagannathan, B.; Jain, S.; Jeng, S. J.; Johnson, J.; Kannan, B.; Ke, Y.; Khan, B.; Kim, B.; Koswatta, S.; Kumar, A.; Kwon, T.; Kwon, U.; Lanzerotti, L.; Lee, H. K.; Lee, W. H.; Levesque, A.; Li, W.; Li, Z.; Liu, W.; Mahajan, S.; McStay, K.; Nayfeh, H.; Nicoll, W.; Northrop, G.; Ogino, A.; Pei, C.; Polvino, S.; Ramachandran, R.; Ren, Z.; Robison, R.; Saraf, I.; Sardesai, V.; Saudari, S.; Schepis, D.; Sheraw, C.; Siddiqui, S.; Song, L.; Stein, K.; Tran, C.; Utomo, H.; Vega, R.; Wang, G.; Wang, H.; Wang, W.; Wang, X.; Wehelle-Gamage, D.; Woodard, E.; Xu, Y.; Yang, Y.; Zhan, N.; Zhao, K.; Zhu, C.; Boyd, K.; Engbrecht, E.; Henson, K.; Kaste, E.; Krishnan, S.; Maciejewski, E.; Shang, H.; Zamdmer, N.; Divakaruni, R.; Rice, J.; Stiffler, S.; Agnello, P. In *High performance 14 nm SOI FinFET CMOS technology with 0.0174  $\mu\text{m}^2$  embedded DRAM and 15 levels of Cu metallization*, IEEE International Electron Devices Meeting, Dec.; IEEE: 2014; pp 3.8.1-3.8.3.
7. Natarajan, S.; Agostinelli, M.; Akbar, S.; Bost, M.; Bowonder, A.; Chikarmane, V.; Chouksey, S.; Dasgupta, A.; Fischer, K.; Fu, Q.; Ghani, T.; Giles, M.; Govindaraju, S.; Grover, R.; Han, W.; Hanken, D.; Haralson, E.; Haran, M.; Heckscher, M.; Heussner, R.; Jain, P.; James, R.; Jhaveri, R.; Jin, I.; Kam, H.; Karl, E.; Kenyon, C.; Liu, M.; Luo, Y.; Mehandru, R.; Morarka, S.; Neiberg, L.; Packan, P.; Paliwal, A.; Parker, C.; Patel, P.; Patel, R.; Pelto, C.; Pipes, L.; Plekhanov, P.; Prince, M.; Rajamani, S.; Sandford, J.; Sell, B.; Sivakumar, S.; Smith, P.; Song, B.; Tone, K.; Troeger, T.; Wiedemer, J.; Yang, M.; Zhang, K. In *A 14 nm logic technology featuring 2nd-generation FinFET, air-gapped interconnects, self-aligned double patterning and a 0.0588  $\mu\text{m}^2$  SRAM cell size*, IEEE International Electron Devices Meeting, Dec.; IEEE: 2014; pp 3.7.1-3.7.3.
8. Wu, S. Y.; Lin, C. Y.; Chiang, M. C.; Liaw, J. J.; Cheng, J. Y.; Yang, S. H.; Chang, S. Z.; Liang, M.; Miyashita, T.; Tsai, C. H.; Chang, C. H.; Chang, V. S.; Wu, Y. K.;

- Chen, J. H.; Chen, H. F.; Chang, S. Y.; Pan, K. H.; Tsui, R. F.; Yao, C. H.; Ting, K. C.; Yamamoto, T.; Huang, H. T.; Lee, T. L.; Lee, C. H.; Chang, W.; Lee, H. M.; Chen, C. C.; Chang, T.; Chen, R.; Chiu, Y. H.; Tsai, M. H.; Jang, S. M.; Chen, K. S.; Ku, Y. In *An enhanced 16nm CMOS technology featuring 2nd generation FinFET transistors and advanced Cu/low-k interconnect for low power and high performance applications*, IEEE International Electron Devices Meeting, Dec.; IEEE: 2014; pp 3.1.1-3.1.4.
9. Moore, G. E., Cramming More Components Onto Integrated Circuits. *Proc. IEEE* **1998**, *86* (1), 82-85.
10. Zhang, H.; Duchaine, J.; Torregrosa, F.; Liu, L.; B. Holländer; Breuer, U.; Mantl, S.; Zhao, Q. T. In *Improved NiSi contacts on Si by CF<sub>4</sub> plasma immersion ion implantation for 14nm node MOSFETs*, 2015 IEEE International Interconnect Technology Conference and 2015 IEEE Materials for Advanced Metallization Conference (IITC/MAM), May; IEEE: 2015; pp 187-190.
11. Peter, A. P.; Meersschaut, J.; Richard, O.; Moussa, A.; Steenbergen, J.; Schaekers, M.; Tókei, Z.; Van Elshocht, S.; Adelman, C., Phase Formation and Morphology of Nickel Silicide Thin Films Synthesized by Catalyzed Chemical Vapor Reaction of Nickel with Silane. *Chem. Mater.* **2015**, *27* (1), 245-254.
12. Kedzierski, J.; Meikei, I.; Kanarsky, T.; Ying, Z.; Wong, H. S. P., Fabrication of metal gated FinFETs through complete gate silicidation with Ni. *IEEE Tran. Electron Devices* **2004**, *51* (12), 2115-2120.
13. Iwai, H.; Ohguro, T.; Ohmi, S.-i., NiSi silicide technology for scaled CMOS. *Microelectron. Eng.* **2002**, *60* (1-2), 157-169.
14. Lavoie, C.; d'Heurle, F. M.; Detavernier, C.; Cabral Jr, C., Towards implementation of a nickel silicide process for CMOS technologies. *Microelectron. Eng.* **2003**, *70* (2-4), 144-157.
15. Tang, W.; Picraux, S. T.; Huang, J. Y.; Gusak, A. M.; Tu, K.-N.; Dayeh, S. A., Nucleation and Atomic Layer Reaction in Nickel Silicide for Defect-Engineered Si Nanochannels. *Nano Lett.* **2013**, *13* (6), 2748-2753.
16. Wang, H.; Zhang, Z.; Wong, L. M.; Wang, S.; Wei, Z.; Li, G. P.; Xing, G.; Guo, D.; Wang, D.; Wu, T., Shape-Controlled Fabrication of Micro/Nanoscale Triangle, Square, Wire-like, and Hexagon Pits on Silicon Substrates Induced by Anisotropic Diffusion and Silicide Sublimation. *ACS Nano* **2010**, *4* (5), 2901-2909.

17. Li, Z.; Gordon, R. G.; Li, H.; Shenai, D. V.; Lavoie, C., Formation of Nickel Silicide from Direct-Liquid-Injection Chemical-Vapor-Deposited Nickel Nitride Films. *J. Electrochem. Soc.* **2010**, *157* (6), H679-H683.
18. Kang, H.-S.; Ha, J.-B.; Lee, J.-H.; Choi, C. K.; Lee, J. Y.; Lee, K.-M., Effect of catalyst for nickel films for NiSi formation with improved interface roughness. *Thin Solid Films* **2011**, *519* (20), 6658-6661.
19. Dupre, C.; Hubert, A.; Becu, S.; Jublot, M.; Maffini-Alvaro, V.; Vizioz, C.; Aussenac, F.; Arvet, C.; Barnola, S.; Hartmann, J. M.; Garnier, G.; Allain, F.; Colonna, J. P.; Rivoire, M.; Baud, L.; Pauliac, S.; Loup, V.; Chevolleau, T.; Rivallin, P.; Guillaumot, B.; Ghibaud, G.; Faynot, O.; Ernst, T.; Deleonibus, S. In *15nm-diameter 3D stacked nanowires with independent gates operation: FET*, 2008 IEEE International Electron Devices Meeting, Dec.; IEEE: 2008; pp 1-4.
20. K.-M. Lee, C. Y. K., C. K. Choi, S.-W. Yun, J.-B. Ha, J.-H. Lee, and J. Y. Lee, Interface prop-erties of nickel-silicide films deposited by using plasma-assisted atomic layer deposition. *J. Korean Phys. Soc.* **2009**, *55* (3), 1153-1157.
21. Ashcroft, A. T.; Cheetham, A. K.; Green, M. L. H.; Vernon, P. D. F., Partial oxidation of methane to synthesis gas using carbon dioxide. *Nature* **1991**, *352* (6332), 225-226.
22. Huber, G. W.; Shabaker, J. W.; Dumesic, J. A., Raney Ni-Sn Catalyst for H<sub>2</sub> Production from Biomass-Derived Hydrocarbons. *Science* **2003**, *300* (5628), 2075-2077.
23. Besenbacher, F.; Chorkendorff, I.; Clausen, B. S.; Hammer, B.; Molenbroek, A. M.; Nørskov, J. K.; Stensgaard, I., Design of a Surface Alloy Catalyst for Steam Reforming. *Science* **1998**, *279* (5358), 1913-1915.
24. Baudouin, D.; Szeto, K. C.; Laurent, P.; De Mallmann, A.; Fenet, B.; Veyre, L.; Rodemerck, U.; Copéret, C.; Thieuleux, C., Nickel–Silicide Colloid Prepared under Mild Conditions as a Versatile Ni Precursor for More Efficient CO<sub>2</sub> Reforming of CH<sub>4</sub> Catalysts. *J. Am. Chem. Soc.* **2012**, *134* (51), 20624-20627.
25. Marciniak, B., *Hydrosilylation of Alkenes and Their Derivatives*. Springer Netherlands: Dordrecht, 2009; p 3-51.
26. Alphazan, T.; Mathey, L.; Schwarzwälder, M.; Lin, T.-H.; Rossini, A. J.; Wischert, R.; Enyedi, V.; Fontaine, H.; Veillerot, M.; Lesage, A.; Emsley, L.; Veyre, L.; Martin, F.; Thieuleux, C.; Copéret, C., Monolayer Doping of Silicon through

Grafting a Tailored Molecular Phosphorus Precursor onto Oxide-Passivated Silicon Surfaces. *Chem. Mater.* **2016**, 28 (11), 3634-3640.

27. Naftel, S. J.; Coulthard, I.; Sham, T. K.; Das, S. R.; Xu, D. X., Structural and electronic property evolution of nickel and nickel silicide thin films on Si(100) from multicore x-ray-absorption fine-structure studies. *Phys. Rev. B* **1998**, 57 (15), 9179-9185.

28. Park, J. Y.; Lee, H.; Renzas, J. R.; Zhang, Y.; Somorjai, G. A., Probing Hot Electron Flow Generated on Pt Nanoparticles with Au/TiO<sub>2</sub> Schottky Diodes during Catalytic CO Oxidation. *Nano Lett.* **2008**, 8 (8), 2388-2392.

29. Lee, H.; Keun Lee, Y.; Nghia Van, T.; Young Park, J., Nanoscale Schottky behavior of Au islands on TiO<sub>2</sub> probed with conductive atomic force microscopy. *Appl. Phys. Lett.* **2013**, 103 (17), 173103.

30. Rose, A., Space-Charge-Limited Currents in Solids. *Phys. Rev.* **1955**, 97 (6), 1538-1544.

31. Ravel, B.; Newville, M., ATHENA, ARTEMIS, HEPHAESTUS: data analysis for X-ray absorption spectroscopy using IFEFFIT. *J. Synchrotron Rad.* **2005**, 12 (4), 537-541.

## **Chapter 3:**

# **Nickel Silicide Layer Deposition on Si Wafer for the Transistor Technology via a Molecular-Tailored Nickel Precursor in a Colloidal Approach**

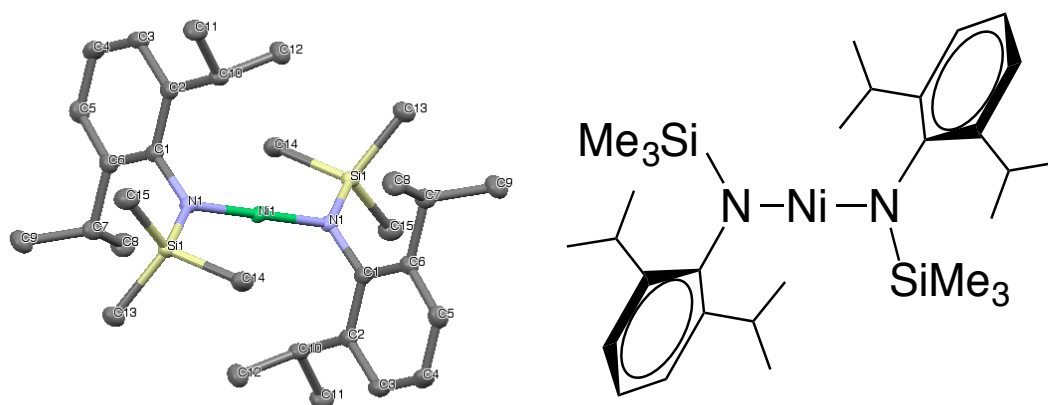
Individual contributions:

T-H. Lin, P-E. Gaillardon and C. Copéret designed all experiments. T-H. Lin developed and characterized all materials. T-H. Lin prepared samples and conducted TEM-EDS analysis with the help of ScopeM. S. Kumar conducted the Au electrode evaporation. L. Zheng carried out AFM analysis.

### 3.1. Introduction

Metal silicide formation has been considered as one of the most important steps in the whole fabrication processes of modern transistors.<sup>1-4</sup> It is used to be the buffer layer between metal wire and Si substrate, which leads to the improvement of current efficiency. Among metal silicides, nickel silicide has been utilized widely in the industry due to its low resistivity and good thermal stability on Si substrate. However, with the trend to use Si substrates with nanometric size and 3D geometry<sup>5-8</sup>, there are some processing limitations according to the current methods. First, the conventional physical vapor deposition (PVD) method relies on hitting a Ni target with high-energy ions, which allows evaporation and depositions of Ni on the Si substrate. However, as mentioned before, sputtering methods are not ideal to build 3D structure because of poor coverage ability on complex structures. This induces ohmic loss during the transport of electrons. Similarly, although chemical vapor deposition (CVD) and atomic layer deposition (ALD) methods provide a potential solution for complex geometric features, they are typically carried out at relatively high temperature (ex: ~300 °C for PECVD), which limits the choices of metal precursors. Moreover, all the current deposition methods are based on a three-step nickel silicide formation, which includes metal deposition, annealing, and wet etching, leading to a high surface roughness. Recently, it is shown that homogeneous nickel silicides layer can be directly deposited on the Si (100) wafer via a low-temperature wet chemical approach by the one-pot reaction between  $\text{Ni(COD)}_2$  and  $\text{SiH}_4$ .<sup>9</sup> However, the hydrocarbon species embedded in the layer after reaction significantly affected the current-voltage (I-V) characteristics, which showed a highly resistive as-synthesize layer. These embedded hydrocarbon species are mostly resulted from the nickel precursor, e.g.  $\text{Ni(COD)}_2$ , i.e. polymerization of COD under reaction conditions. Therefore, by carefully selecting the precursor with easily decomposed ligands, it is expected that the carbon contamination would be largely decreased, helping to obtain better electrical properties. Recent advances have shown that around 3.4 nm nickel colloids can be formed via the reaction of the molecular-tailored Ni precursor, e.g.  $\text{Ni[N(SiMe}_3\text{)(2,6-}i\text{Pr}_2\text{C}_6\text{H}_3\text{)]}_2$ , and  $\text{H}_2$  at 55 °C,<sup>10</sup> indicating that this Ni precursor with amido ligands has a good reactivity and can likely be further applied to the formation of nickel silicide.

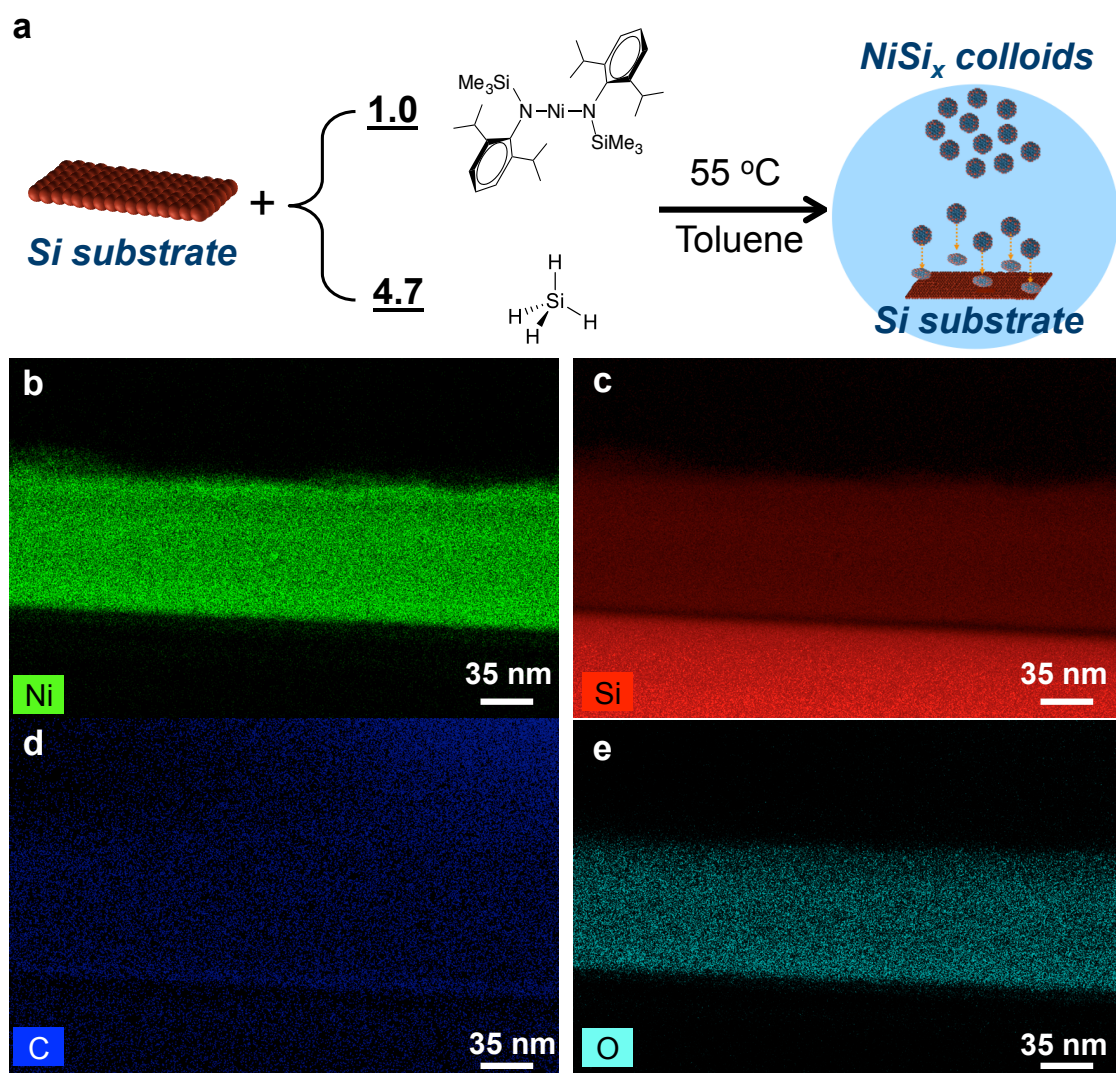
Herein, we show that by utilizing this nickel precursor,  $\text{Ni}[\text{N}(\text{SiMe}_3)(2,6\text{-iPr}_2\text{C}_6\text{H}_3)]_2$  (Figure 3.1),<sup>11</sup> and low temperature in-situ deposition conditions ( $\text{SiH}_4$  at 55 °C in toluene with Si (100) wafer), a homogeneous and conformal nickel silicide layer can be deposited on Si substrates. It displays the Schottky behavior and has a series resistance of 5.4  $\Omega$  (46  $\mu\Omega\cdot\text{cm}$  for resistivity) based on a model fitting. After thermal annealing under  $\text{H}_2$  flow, this layer shows a lower series resistance of 3.2  $\Omega$  (24  $\mu\Omega\cdot\text{cm}$  for resistivity) and an energy barrier height of 0.4 eV with the surface roughness of 3.2 nm.



**Figure 3.1.** Molecular structure of  $\text{Ni}[\text{N}(\text{SiMe}_3)(2,6\text{-iPr}_2\text{C}_6\text{H}_3)]_2$ .

### 3.2. Results and discussion

Reaction of  $\text{Ni}[\text{N}(\text{SiMe}_3)(2,6\text{-iPr}_2\text{C}_6\text{H}_3)]_2$  (0.07 mmol) and  $\text{SiH}_4$  (0.33 mmol) in toluene at 55 °C lead to an homogeneous 85 nm Ni-rich layer deposited on the Si (100) wafer (Figure 3.2a) along with 2.9 nm colloids remaining in solution (Figure A.3.1a-A.3.1b). Energy-Dispersive X-ray Spectroscopy (EDS) mapping shows that the layer contains a homogeneous composition of Ni and Si along with some amounts of carbon and oxygen (Figure 3.2b-e). The presence of carbon is probably resulted from the embedded ligands of the layer after reaction as well as the exposure to the air during the ex-situ transfer. The presence of oxygen is majorly resulted from the formation of  $\text{NiSi}_x\text{O}_y$  species upon exposure to air during the ex-situ transfer (vide infra).

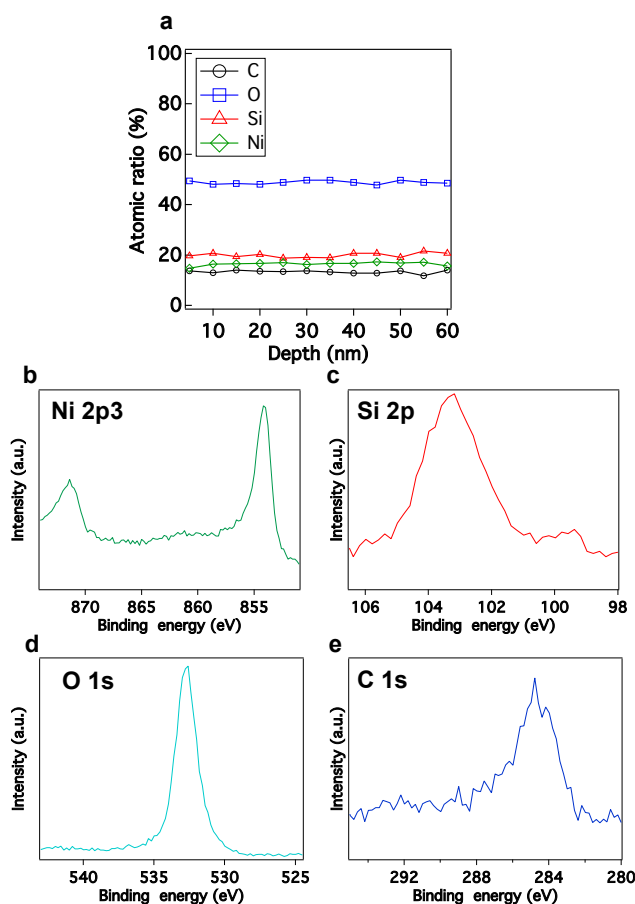


**Figure 3.2.** (a) Reaction scheme for one-pot synthesis; the condition is as below:  $\text{Ni}[\text{N}(\text{SiMe}_3)(2,6\text{-iPr}_2\text{C}_6\text{H}_3)]_2/\text{die}$ ,  $110000 \text{ Ni.nm}^{-2}$ ,  $\text{SiH}_4/\text{Ni}=4.7$  with toluene at  $55^\circ\text{C}$  for 16 h. (b) EDS mapping image of the Ni-rich layer on the Si substrate. (c-e) Si, C, and O EDS mapping images of the Ni-rich layer on the Si substrate, respectively.

X-ray photoelectron spectroscopy (XPS) depth profile (Figure 3.3a) confirms the homogeneous composition of the Ni-rich layer, which is composed of similar amounts of Ni and Si (average 16% and 19% respectively), along with 13% carbon and 49% oxygen, consistent with EDS results discussed above. The surface carbon ratio in the reference pristine Si wafer is  $\sim 9\%$  (Figure A.3.2), indicating that only a small amount of hydrocarbon species in the layer arises from the molecular precursor. Within the depth of 30 nm (detailed XPS data of whole depth in Figure A.3.3), Ni 2p<sub>3/2</sub> XPS spectra (Figure 3.3b) show a peak around 853.0 eV, indicating the presence of oxidized nickel species in this layer, and this nickel species are majorly composed of



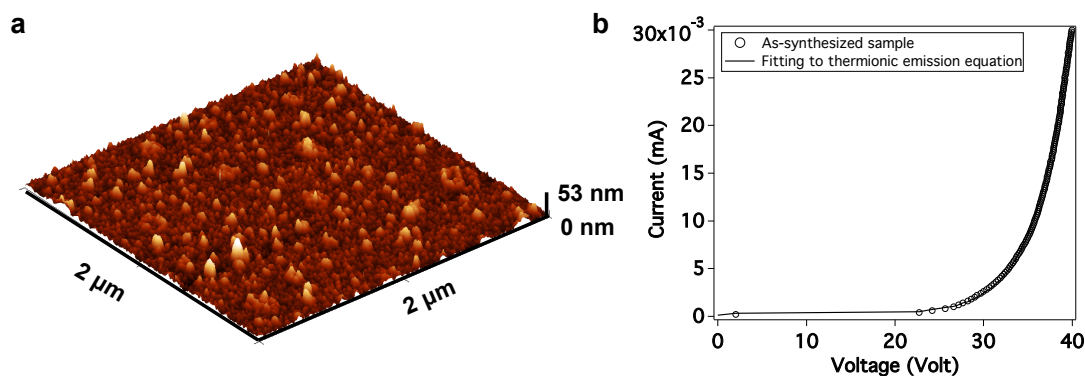
Ni<sub>2</sub>Si.<sup>12, 13</sup> The main Si 2p peak is at ~103 eV (Figure 3.3c) and O 1s peak is at ~532.5 eV (Figure 3.3d), indicating the formation of NiSi<sub>x</sub>O<sub>y</sub> species as discussed above (Figure 3.2).<sup>14, 15</sup> The presence of another broad peak at ~99.3 eV shows that there are reduced silicon species in the layer. Combined with the XPS data on Ni 2p<sub>3/2</sub> signal indicates that this species is mostly Ni<sub>2</sub>Si.<sup>12</sup> From C 1s spectra (Figure 3.3e), there is a broad carbon signal centered at 284.5, which probably originates from the embedded hydrocarbon ligands of Ni[N(SiMe<sub>3</sub>)(2,6-iPr<sub>2</sub>C<sub>6</sub>H<sub>3</sub>)]<sub>2</sub> and also from the carbon contamination due to the ex-situ transfer.



**Figure 3.3.** (a) XPS depth profile quantization on the as-synthesized coated wafer. (b) Ni 2p<sub>3/2</sub>, (c) Si 2p, (d) O 1s and (e) C 1s XPS spectra at the sputtering depth of 30 nm.

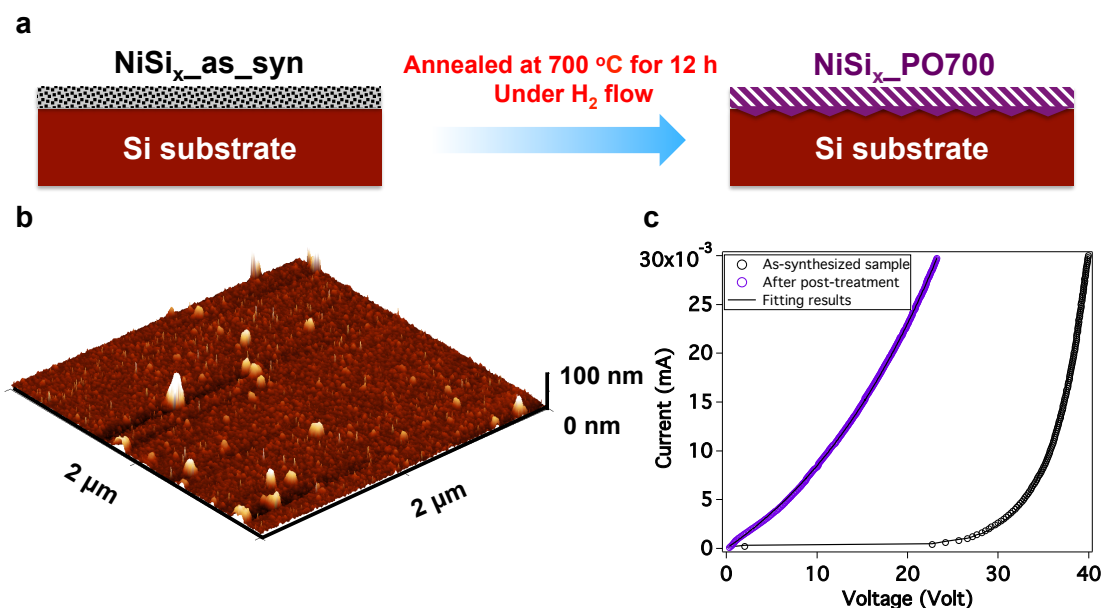
Atomic force microscopy (AFM) image reveals that the as-synthesized NiSi<sub>x</sub> layer contains a series of domains (Figure 3.4a) likely resulting from the aggregation of NiSi<sub>x</sub> nanoparticles on the substrate. The root mean square roughness ( $R_{\text{rms}}$ ) is equal to 5.2 nm. Further characterization of the NiSi<sub>x</sub> layer by four-point probe measurement – the current (I) – voltage (V) behavior is shown in Figure 3.4b – shows

a typical Schottky characteristics, with a barrier height of 0.64 eV and series resistance of 5.4  $\Omega$  (46  $\mu\Omega\cdot\text{cm}$  for resistivity) with an ideality factor of 149, obtained by using the thermionic emission model fitting (see Appendix).<sup>16</sup> This high ideality factor and the barrier height is consistent with the presence of voids or ligands between amorphous nanoparticles, which inhibits electron transport.



**Figure 3.4.** (a) AFM image from as-synthesized sample,  $R_{\text{rms}} = 5.2$  nm. (b) I-V characteristics of  $\text{NiSi}_x$  layer on the Si(100) wafer fitting to thermionic emission equation.

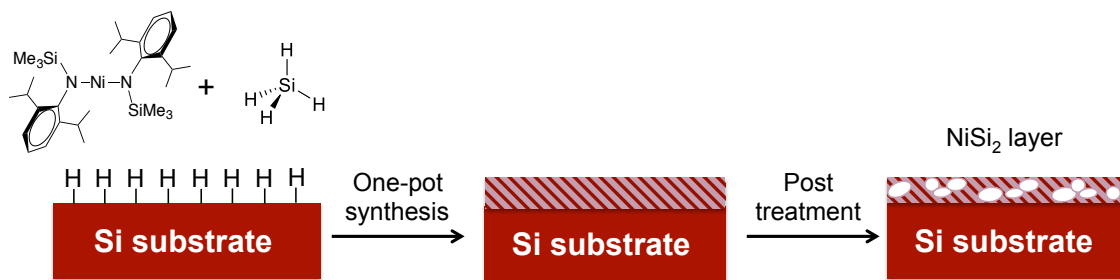
In order to remove residual hydrocarbon ligands, the post-treatment has been conducted by treating the as-synthesized sample at 700  $^{\circ}\text{C}$  under  $\text{H}_2$  flow for 12 h (Figure 3.5a). HAADF image (Figure A.3.3) displays that after the post-treatment, the layer thickness is  $\sim 75$  nm, and it remains a homogeneous distribution, which contained Ni (Figure A.3.4) and Si (Figure A.3.5) as well as carbon (Figure A.3.6) and oxygen (Figure A.3.7) contaminations due to the ex-situ transfer. AFM image shows that  $R_{\text{rms}}$  decrease to 3.2 nm after post-treatment, revealing the improvement of surface roughness compared to the as-synthesized sample (Figure 3.5b). Moreover, the I-V characteristics are significantly improved showing a better ohmic characteristic compared to the as-synthesized materials (Figure 3.5c). However, it still shows a partial Schottky behavior based on the fitting results, which show that this layer exhibits a barrier height of 0.40 eV and a series resistance of 3.2  $\Omega$  (24  $\mu\Omega\cdot\text{cm}$  for resistivity) with a high ideality factor of 723. The low barrier height and low resistance are likely resulted from the removal of embedded ligands upon thermal annealing. However, the high ideality factor implies a large deviation from typical Schottky behavior, consistent with that it exhibits mostly ohmic characteristics.



**Figure 3.5.** (a) Scheme of the annealing process in this work; the condition as below: As-synthesize sample was annealed at 700 °C for 12 h under H<sub>2</sub> flow. (b) AFM image from sample after post-treatment,  $R_{\text{rms}} = 3.2$  nm. (c) I-V characteristics of the NiSi<sub>x</sub> layer deposited on a Si(100) wafer: Purple line: sample after 700 °C post-treatment under H<sub>2</sub> flow; black line: as-synthesized NiSi<sub>x</sub> sample.

### 3.3. Conclusion

This work has allowed for the direct deposition of the NiSi<sub>x</sub> layer on a Si (100) substrate via the reaction of Ni[N(SiMe<sub>3</sub>)(2,6-iPr<sub>2</sub>C<sub>6</sub>H<sub>3</sub>)]<sub>2</sub> and SiH<sub>4</sub> in toluene at 55 °C. Post-treatment under H<sub>2</sub> generates a layer with a low surface roughness ( $R_{\text{rms}}=3.2$  nm) and displays a low series resistance of 3.2 Ω (24 μΩ.cm for resistivity) from the model fitting. However, since there are still certain amounts of embedded ligands inside the as-synthesized layer, it leads to the presence of remaining of voids in the layer after the ligands removal via thermal annealing (Figure 3.6). In summary, this work shows that molecular-tailored Ni precursor can be utilized for the nickel silicide formation via the colloidal approach, while by appropriately design, it is expected that the nickel silicide layer with pure ohmic behavior can be prepared via this system.



**Figure 3.6.** Scheme of the colloidal approach to form the  $\text{NiSi}_x$  layer in this work.

### 3.4. Experimental details

**General information.** The experiments were carried out using Schlenk techniques. Toluene was dried and collected using a mBraun SBS-800 purification system and degassed by Schlenk techniques (vacuum to  $10^{-1}$  mbar and purged with dry Ar for 10 times). 40% HF solution was purchased from VWR. Si(0) nanopowder was purchased from US-nano with the size between 20-30 nm and with 98% purity.  $\text{Ni}[\text{N}(\text{SiMe}_3)(2,6\text{-iPr}_2\text{C}_6\text{H}_3)]_2$  was synthesized according to reported procedures.<sup>11</sup> 1%  $\text{SiH}_4$  (N5.0) in helium was purchased from PanGas.  $\text{H}_2$  was purified over R3-11 BASF catalyst / MS 4 Å before use.

#### Nickel silicide colloidal nanoparticle synthesis on Si wafer (One-pot synthesis).

Double side polished p-type 4" Si wafers with (100) orientations were diced into 2 cm  $\times$  1 cm dies, cleaned by a 40% HF solution for 60 s, and washed with DI water to remove excess HF. The diced wafers were then dried under high vacuum ( $\sim 10^{-5}$  mbar) at room temperature for 12 h.

A HF-treated diced Si-wafer and 12.4 mg  $\text{Ni}[\text{N}(\text{SiMe}_3)(2,6\text{-iPr}_2\text{C}_6\text{H}_3)]_2$  (0.07 mmol) were placed in a 325 mL Fischer-Porter bottle in a glovebox and dissolved in toluene (10 mL). The reactor was then pressurized under 2.7 bars of 1%  $\text{SiH}_4$  in He (0.33 mmol) and heated to 55 °C for 16 h, during which a layer was formed on top of the Si-wafer accompanied by a dark solution (colloids formation). The colloidal solution was cannulated out of the reactor and the Si-wafer was washed 2 times with 10 mL of toluene. Prior storage inside glovebox, the as-synthesized wafer was dried under vacuum ( $\sim 10^{-2}$  mbar) for 3 h.

**Nickel silicide colloidal nanoparticle synthesis on Si(0) nanopowder (One-pot synthesis).** 2.0 g of Si(0) nanopowder were reduced under a flow of pure hydrogen

(100 mL.min<sup>-1</sup>) at 900 °C (1 °C.min<sup>-1</sup>) for 12 h to obtain a pristine Si-H surface (Figure S3). 50 mg of Si(0) nanopowders and 46.5 mg Ni[N(SiMe<sub>3</sub>)(2,6-iPr<sub>2</sub>C<sub>6</sub>H<sub>3</sub>)]<sub>2</sub> (0.07 mmol) were placed in a 325 mL Fischer-Porter reactor in a glovebox and dissolved in toluene (10 mL). The reactor was then pressurized under 2.7 bar of 1% SiH<sub>4</sub> in He (0.45 mmol) and heated to 55 °C for 16 h, during which the solution color turned to black. Inside a glovebox, the Si-powder was separated from the solution using a filter and consecutively washed for 3 times with 10 mL of toluene. The Si-powder was dried under high vacuum (~10<sup>-5</sup> mbar) for 3 h.

**Post-treatment condition.** As-synthesized wafer or nanopowders were treated under H<sub>2</sub> flow at 700 °C (1 °C.min<sup>-1</sup>) for 12 h.

### **Characterization Techniques.**

#### Transmission Electron Microscopy (TEM)

TEM images were taken with a FEI Tecnai Orisis ultrahigh vacuum transmission electron microscope. Energy-dispersive (EDS) detector was attached onto the FEI Tecnai Orisis for elemental mapping analysis.

#### TEM sample preparation by a tripod method

The as-synthesized wafer was cleaved into two pieces of 2.5 × 1.8 mm, which were glued face-to-face using a Gatan G2 epoxy glue. The specimen was then mounted on the side of a tripod polisher, which was heated at 100 °C. To remove most of the Si-bulk wafer, the polishing procedure was conducted using a series of plastic diamond lapping films, with grains of decreasing sizes (30 μm, 15 μm, 6 μm, 1 μm, 0.5 μm, and 0.1 μm) and a final step was polished on a felt-covered disc using the slurry of silica with 25 nm grain size. The specimen was then mounted on the bottom of a tripod polisher, which was heated at 100 °C. The glass support was perfectly flat polished to ensure a correct 0.6° angle of the wedge shape specimen. The same polishing procedure was used for the bottom part leading to appearance of interference fringes (electron transparency), and then the specimen was glued on a Mo grid. After 12 h of drying, the grid was detached from the tripod using acetone to dissolve the glue, and the specimen was cleaned by acetone.

### TEM sample preparation by focus-ion-beam (FIB) method

A TEM lamella was prepared by the in-situ lift-out technique on a Zeiss NVision 40 FIB-SEM. The lamella was thinned using 30 kV Ga<sup>+</sup>. For the 5 kV showering to reduce the thickness of the damage layer the lamella was tilted 10° into the beam.

### Atomic Force Microscopy

The AFM measurements were conducted on a commercial AFM system (BioScope Catalyst, Bruker Nano, Santa Barbara, California) that is mounted onto an inverted confocal laser-scanning microscope (FluoView FV500, Olympus, Center Valley, Pennsylvania). The images shown in this study were obtained using tapping mode AFM with CT300R-25 cantilever probes (Nanoscience, USA). The AFM images are 2  $\mu\text{m}^2$  in size, with a resolution of  $512 \times 512$  pixels, and a scan rate of 0.2 Hz.

### Fourier Transformed Infrared Spectroscopy (FTIR)

FTIR spectra of wafers were recorded in transmission mode on Thermo Scientific, Nicolet 6700, in which the measurements were performed under inert condition with a deuterated triglycine sulfate (DTGS) detector with 1000 averaged scans to achieve an optimal signal-to-noise ratio. FTIR spectra of nanopowders were recorded in transmission mode on a Bruker ALPHA-T FTIR spectrophotometer under inert condition.

### X-ray Photon Spectroscopy (XPS)

XPS depth profiles were recorded using a Kratos Axis Ultra DLD spectrometer with monochromic Al K $\alpha$  radiation (1486.6 eV). A commercial Kratos charge neutralizer was used to avoid non-homogeneous electric charge and to achieve better resolution. The resolution measured as full width at half maximum of the curve fitted photoemission peaks was approximately 1 eV. Binding energy (BE) values refer to the Fermi edge and the energy scale was calibrated using Au 4f<sub>7/2</sub> at 84.0 eV and Cu 2p<sub>3/2</sub> at 932.67 eV. Samples were attached to a stainless-steel sample holder bar using a double-sided sticking Cu tape. XPS data were analyzed with CasaXPS software version 2313 Dev64. The C-C component of the C 1s peak was set to a binding energy of 284.8 eV to correct for the charging effect on each sample. The atomic

concentrations of the elements in the near-surface region were estimated taking into account the corresponding Scofield atomic sensitivity factors and Inelastic Mean Free Path (IMFP) of photoelectrons using standard procedures in the CasaXPS software. Depth profiling was conducted by step by step sputtering of a sample with a Kratos polyatomic sputtering gun operating in Ar mode at 5 keV,  $I_{\text{ion}} \approx 1 \mu\text{A}$ . Thickness of the layers was calibrated using the TEM measured thickness.

#### Electrical performance evaluation.

For four-point probe measurement, four 100 nm gold (Au) electrodes were deposited to a circle-shape layer (0.25 mm in radius; separate with each one by 1 mm) with a deposition rate of  $5 \pm 2 \text{ \AA} \cdot \text{s}^{-1}$  by thermal evaporation of Au ingots under high vacuum ( $\sim 10^{-5}$  mbar). The Au ingots (99.999%) were supplied by Kurt J. Lesker. A MBraun glovebox integrated MBraun vacuum thermal evaporator was used for the Au evaporation. The probe station used for I-V characteristic measurement is a Signatone S1160, and the I-V data were acquired by a Keysight B1500 with B1510A High Power source/monitor unit (HPSMU).

### **3.5. References**

1. Nicolet, M.-A.; Lau, S. S., Chapter 6 - Formation and Characterization of Transition-Metal Silicides. In *VLSI Electronics Microstructure Science*, Einspruch, N. G.; Larrabee, G. B., Eds. Elsevier: 1983; Vol. 6, pp 329-464.
2. Zaima, S.; Nakatsuka, O., 17 - Silicide and germanide technology for interconnections in ultra-large-scale integrated (ULSI) applications. In *Silicon–Germanium (SiGe) Nanostructures*, Woodhead Publishing: 2011; pp 456-469.
3. Reader, A. H.; Ommen, A. H. v.; Weijs, P. J. W.; Wolters, R. A. M.; Oostra, D. J., Transition metal silicides in silicon technology. *Reports on Progress in Physics* **1993**, 56 (11), 1397.
4. Zhang, S. L.; Zhang, Z., 6 - Metal silicides in advanced complementary metal-oxide-semiconductor (CMOS) technology. In *Metallic Films for Electronic, Optical and Magnetic Applications*, Woodhead Publishing: 2014; pp 244-301.
5. IBM breakthrough leads to first 5-nm chip. *C&EN Global Enterprise* **2017**, 95 (24), 11-11.

6. Hisamoto, D.; Wen-Chin, L.; Kedzierski, J.; Takeuchi, H.; Asano, K.; Kuo, C.; Anderson, E.; Tsu-Jae, K.; Bokor, J.; Chenming, H., FinFET-a self-aligned double-gate MOSFET scalable to 20 nm. *IEEE Tran. Electron Devices* **2000**, *47* (12), 2320-2325.
7. Ilatikhameneh, H.; Ameen, T.; Novakovic, B.; Tan, Y.; Klimeck, G.; Rahman, R., Saving Moore's Law Down To 1 nm Channels With Anisotropic Effective Mass. *Scientific Reports* **2016**, *6*, 31501.
8. Trivedi, V.; Fossum, J. G.; Chowdhury, M. M., Nanoscale FinFETs with gate-source/drain underlap. *IEEE Transactions on Electron Devices* **2005**, *52* (1), 56-62.
9. Lin, T.-H.; Margossian, T.; De Marchi, M.; Thammasack, M.; Zemlyanov, D.; Kumar, S.; Jagielski, J.; Zheng, L.-Q.; Shih, C.-J.; Zenobi, R.; De Micheli, G.; Baudouin, D.; Gaillardon, P.-E.; Copéret, C., Low-Temperature Wet Conformal Nickel Silicide Deposition for Transistor Technology through an Organometallic Approach. *ACS Appl. Mater. Interfaces* **2017**, *9* (5), 4948-4955.
10. Margossian, T.; Larmier, K.; Kim, S. M.; Krumeich, F.; Müller, C.; Copéret, C., Supported Bimetallic NiFe Nanoparticles through Colloid Synthesis for Improved Dry Reforming Performance. *ACS Catalysis* **2017**, *7* (10), 6942-6948.
11. Lipschutz, M. I.; Tilley, T. D., Synthesis and reactivity of a conveniently prepared two-coordinate bis(amido) nickel(ii) complex. *Chemical Communications* **2012**, *48* (57), 7146-7148.
12. Grunthaner, P. J.; Grunthaner, F. J.; Mayer, J. W., XPS study of the chemical structure of the nickel/silicon interface. *Journal of Vacuum Science and Technology* **1980**, *17* (5), 924-929.
13. Grosvenor, A. P.; Biesinger, M. C.; Smart, R. S. C.; McIntyre, N. S., New interpretations of XPS spectra of nickel metal and oxides. *Surf. Sci.* **2006**, *600* (9), 1771-1779.
14. Asakawa, T.; Tanaka, K.; Toyoshima, I., Interaction of nickel with silicon oxide or silica formed on silicon(111) and carbon monoxide adsorption inhibition in nickel/silicon oxide/n-silicon(111) studied by XPS and AES. *Langmuir* **1988**, *4* (3), 521-526.
15. Lu, B.; Kawamoto, K., Transition metal-rich mesoporous silicas and their enhanced catalytic properties. *Catalysis Science & Technology* **2014**, *4* (12), 4313-4321.



16. Lee, H.; Keun Lee, Y.; Nghia Van, T.; Young Park, J., Nanoscale Schottky behavior of Au islands on TiO<sub>2</sub> probed with conductive atomic force microscopy. *Appl. Phys. Lett.* **2013**, *103* (17), 173103.

## **Chapter 4:**

# **Conformal Deposition of Conductive Single-Crystalline Cobalt Silicide Layer on Si Wafer via a Molecular Approach**

Individual contributions:

Adapted from “T-H. Lin, T. Margossian, L. Zheng, S. Kumar, I. Marozau, O. Sereda, D. Zemlyanov, C-J. Shih, R. Zenobi, D. Baudouin, G. D. Micheli, P-E. Gaillardon and C. Copéret, *Chem. Mater.*, 2018, 30, 2168-2173. ”

T-H. Lin, P-E. Gaillardon and C. Copéret designed all experiments. T-H. Lin developed and characterized all materials. T-H. Lin prepared samples and conducted TEM-EDS analysis with the help of ScopeM. S. Kumar conducted the Au electrode evaporation. L. Zheng carried out AFM analysis. D. Zemlyanov performed XPS analysis. I. Marozau and O. Sereda performed XRD measurement. All authors contribute to the scientific discussions.

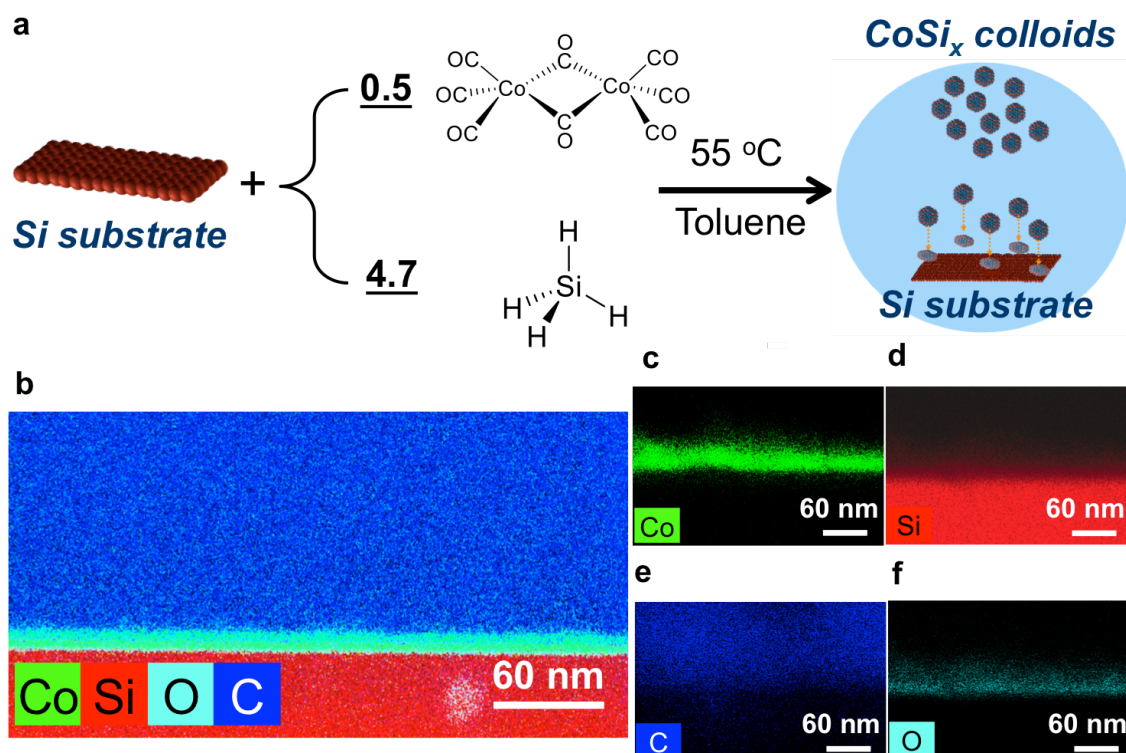
#### 4.1. Introduction

The downscaling trend in microelectronics has led to the decrease of gate length in modern transistors down to values of 10 nm and below.<sup>1-5</sup> In parallel, 3D-transistor structures have been designed to optimize the electrostatic control and maximize the density of integration.<sup>6-10</sup> However, these advances point to the need of alternative route in most of the fabrication steps in order to achieve an optimum performance in 3D-structured devices. This applies to metal silicides, which are needed to decrease the transistor contact resistivity. Of all metal silicides, cobalt silicide ( $\text{CoSi}_2$ ) display several advantages such as having a small lattice mismatch on Si substrate ( $\sim 1.2\%$ ), single crystallinity with epitaxial growth on Si, high thermal stability and lower relative resistivity.<sup>11, 12</sup> However, it is not widely used in industry due to the high roughness issue ( $R_{\text{rms}}$  is always higher than 10 nm)<sup>13</sup> resulting from large amounts of Si consumption during its formation with conventional physical methods, e.g. rapid thermal annealing after metal evaporation or sputtering.<sup>11</sup> Additionally, conventional physical methods result in limited conformality, i.e. limited homogeneity of the deposited layer throughout the targeted surface. As a result, atomic layer deposition (ALD) has been widely investigated because it yields a better conformality under low-temperature process.<sup>14-16</sup> Nevertheless, the thermal instability of cobalt molecular precursors in gas-phase reaction is still a major challenge, which limits its applicability.<sup>14</sup> Recently, various electronic devices have been established based on the synthesis of nanoparticles via the colloidal approach.<sup>17-19</sup> Recent advances have shown that the metal silicides can be prepared at low temperatures<sup>20</sup> and that this approach can be used for the direct and conformal formation of nickel silicide via a low-temperature wet chemical approach.<sup>21</sup> However, this nickel silicide displays ill-defined electrical properties due to the presence of resistive domains that cannot be removed upon annealing.

Here, we show that by selecting an appropriate cobalt precursor,  $\text{Co}_2(\text{CO})_8$ , and low temperature in-situ deposition conditions ( $\text{SiH}_4$  at 55 °C in toluene with Si (100) wafer), a homogeneous and conformal cobalt silicide layer can be grown on Si substrates. After thermal annealing under vacuum, this layer contains a single crystalline  $\text{CoSi}_2$  phase and displays the desired metallic conductive properties, showing an Ohmic behavior with a low resistivity (11.7  $\mu\Omega\cdot\text{cm}$ ; for comparison, the resistivity of bulk  $\text{Co}(0)$  metal equals to 11.1  $\mu\Omega\cdot\text{cm}$ ).<sup>22</sup>

## 4.2. Results and discussion

The reaction of  $\text{Co}_2(\text{CO})_8$  (0.035 mmol) and  $\text{SiH}_4$  (0.33 mmol) in toluene at 55 °C with Si (100) wafer (Figure 4.1a) leads to the homogeneous deposition of ca. 20 nm Co-rich layer on the Si (100) wafer (Figure 4.1b) along with 3.5 nm colloids remaining in solution (Figure A.4.1a-A.4.1b). The transmission Fourier transform infrared spectroscopy (FT-IR) analysis of the gas phase clearly show the presence of unreacted  $\text{SiH}_4$  ( $2180\text{ cm}^{-1}$ ) and a large amount of CO ( $2140\text{ cm}^{-1}$ ),<sup>23, 24</sup> consistent with the reaction of  $\text{Co}_2(\text{CO})_8$  with presumably  $\text{SiH}_4$  (Figure A.4.1d). Quantification by gas chromatography-mass spectrometry (GC-MS) indicates the release of ca. 7.6 equiv. of CO per  $\text{Co}_2(\text{CO})_8$ . Energy-Dispersive X-ray Spectroscopy (EDS) mapping (Figure 4.1b) shows that the layer homogeneously contains Co (Figure 4.1c) and Si (Figure 4.1d) along with a small amount of carbon (Figure 4.1e) and oxygen (Figure 4.1f). The presence of oxygen likely results from the formation of  $\text{CoSi}_x\text{O}_y$  species upon exposure to air during the ex-situ transfer (vide infra). Further analysis of the deposited layer by FTIR shows the presence of a peak at  $2010\text{ cm}^{-1}$  associated with the presence of remaining CO ligand bound to Co. (Figure A.4.1e)

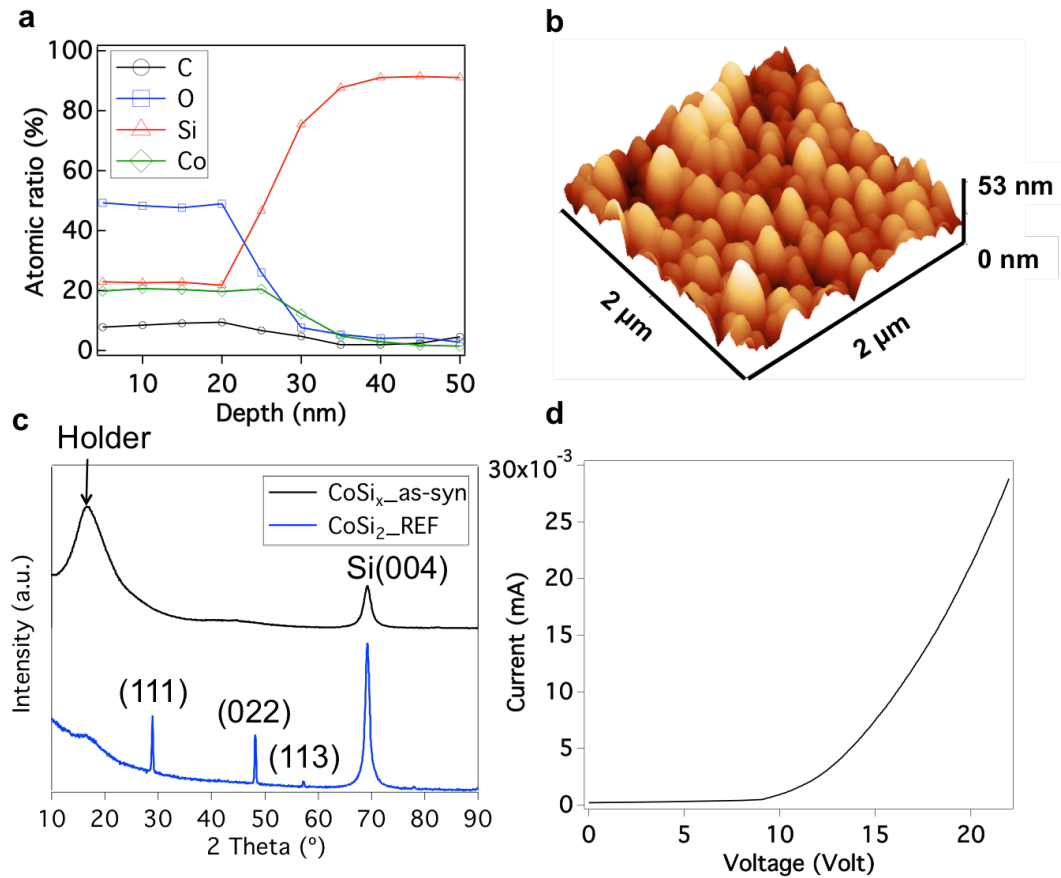


**Figure 4.1.** (a) Reaction scheme for one-pot synthesis; the condition is as below:  $\text{Co}_2(\text{CO})_8/\text{die}$ ,  $110000\text{ Co.nm}^{-2}$ ,  $\text{SiH}_4/\text{Co}=4.7$  with toluene at 55 °C for 16 h. (b) EDS

mapping image of the Co-rich layer on the Si substrate. (c-f) Co, Si, C, and O EDS mapping images of the Co-rich layer on the Si substrate, respectively. The wafer was exposed to air prior to analysis.

X-ray photoelectron spectroscopy (XPS) depth profile (Figure 4.2a) confirms the homogeneous composition of the Co-rich layer, which is composed of similar amounts of Co and Si (average 20% and 23% in the first 20 nm respectively), along with 8% carbon and 49% oxygen, consistent with EDS results discussed above. Within the depth of 20 nm (detailed XPS data of whole depth in Figure A.4.2), Co 2p<sub>3/2</sub> XPS spectra (Figure A.4.2a) show a broad peak around 778.2~778.4 eV, indicating the presence of different oxidized cobalt species in this layer.<sup>25, 26</sup> The main Si 2p peak is at ~103 eV (Figure A.4.2b) and O 1s peak is at ~532.4 eV (Figure A.4.2c), which is significantly different from SiO<sub>2</sub> (103.3 eV for Si 2p and 532.7 for O 1s),<sup>27, 28</sup> indicating the formation of CoSi<sub>x</sub>O<sub>y</sub> species as discussed above (Figure 4.1f). From C 1s spectra (Figure A.4.2d), a broad carbon signal appears at 284.0~286.0, including sp<sup>2</sup> carbon (284.5 eV) with some sp<sup>3</sup> carbon or oxidized sp<sup>2</sup> carbon (285.4 eV).<sup>29</sup> It probably originates from the background of the pristine Si wafer, which also exhibits ~9% carbon with the similar peak position (Figure A.4.3), or from the embedded CO ligand from Co precursor (Figure A.4.1e). These XPS data provide evidences of the homogeneous distribution of Co and Si in the layer. X-ray absorption spectroscopy (XAS) analysis was conducted on a model substrate with high surface area, e.g., Si(0) nanoparticles, in place of Si wafer in order to obtain spectroscopic data with better quality, which are consistent with the formation of CoSi<sub>x</sub>. The observed edge shift at the Co K edge with respect to Co(0) foil indicates that this film is composed of CoSi<sub>x</sub> instead of Co(0), and the energy shift is attributed to the charge redistribution for the CoSi<sub>x</sub> formation (Figure A.4.4c). Atomic force microscopy (AFM) image reveals that the as-synthesized CoSi<sub>x</sub> layer is composed of large domains (Figure 4.2b), associated with the aggregation of CoSi<sub>x</sub> colloidal nanoparticles on the substrate, as evidenced by the root mean square roughness ( $R_{\text{rms}}$ ) of 8.5 nm. X-ray diffraction (XRD) on the as-synthesized layer does not show any crystalline domain, consistent with the formation of amorphous CoSi<sub>x</sub> (Figure 4.2c). This CoSi<sub>x</sub> layer was then characterized by four-point probe measurement, and its current (I) – voltage (V) behavior is shown in Figure 4.2d. The IV curve exhibits Schottky characteristics, with a barrier height of 0.54 eV and series resistance of

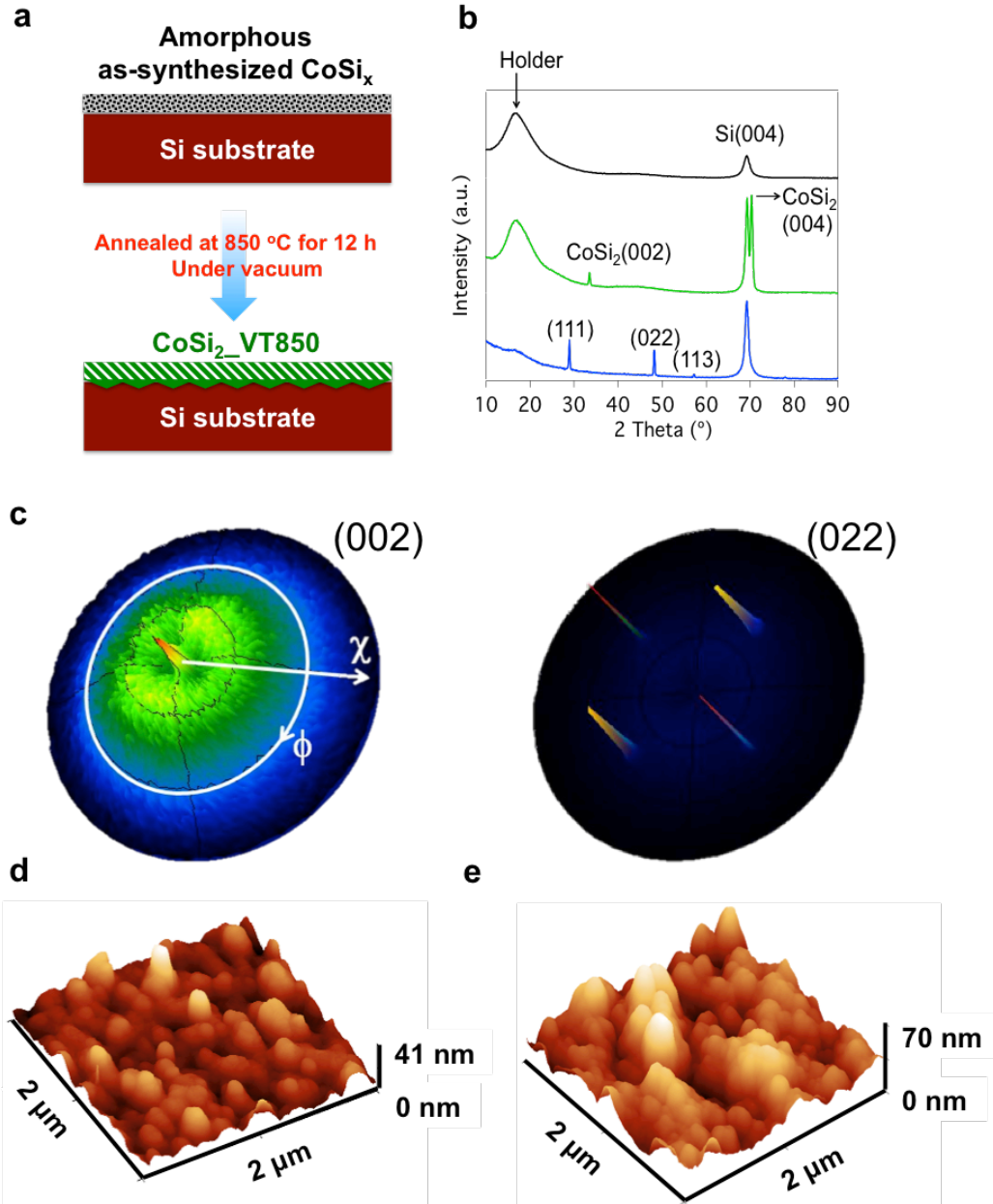
147.1  $\Omega$  with an ideality factor of 115, obtained by using the thermionic emission model fitting (see Appendix).<sup>30</sup> This ill-defined ideality factor, together with high sheet resistance, is the signature of an energy barrier formed due to voids or ligands between amorphous nanoparticles.



**Figure 4.2.** (a) XPS depth profile quantization on the as-synthesized wafer. (b) AFM images of as-synthesized CoSi<sub>x</sub> layer on the Si substrate. (c) X-ray diffraction patterns of CoSi<sub>x</sub> on Si(100) substrate: As-synthesized sample (black curve) and reference CoSi<sub>2</sub> by conventional method (blue curve) with Miller index shown for Si and CoSi<sub>2</sub> crystalline peaks. (d) I-V characteristics of as-synthesized CoSi<sub>x</sub> layer on the Si(100) wafer.

In order to remove the residual carbon (such as CO ligands) and to obtain a crystalline CoSi<sub>x</sub> layer, which should in turn provide the desired electrical properties, a thermal annealing is conducted under vacuum (schematics see Figure 4.3a) and monitored via XRD. While samples treated at various temperatures (350 °C, 500 °C, or 700 °C) under vacuum do not show crystalline CoSi<sub>x</sub> signals (Figure A.4.5), raising the temperature to 850 °C (green curve in Figure 4.3b) leads to the appearance of two

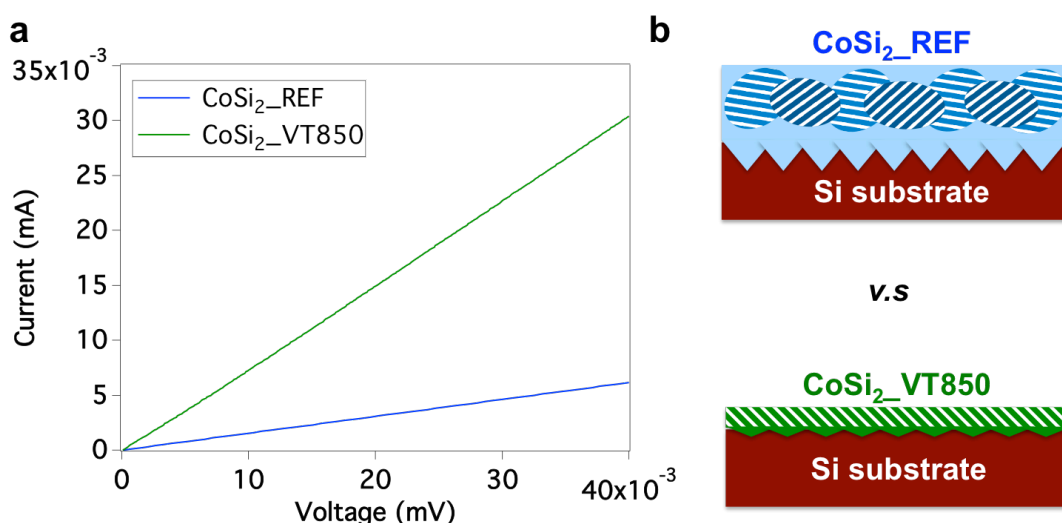
reflections at  $2\theta = 34^\circ$  and  $70^\circ$ , associated with the  $\text{CoSi}_2$  (002) and (004) planes, respectively, thus suggesting the formation of oriented single crystalline  $\text{CoSi}_2$  phase. This contrasts with the  $\text{CoSi}_2$  obtained by the conventional method (blue curve in Figure 4.3b, experimental details in Appendix), which reveals three major reflections at  $2\theta = 29^\circ$ ,  $48^\circ$  and  $57^\circ$ , assigned to  $\text{CoSi}_2$  (111), (022), and (113) planes, respectively consistent with the formation of polycrystalline  $\text{CoSi}_2$ . In order to further study the epitaxial relationship of obtained  $\text{CoSi}_2$  film on Si substrate after annealing at  $850^\circ\text{C}$  under vacuum, pole figures were acquired for the  $\text{CoSi}_2$  (002) and (022) diffraction reflections (Figure 4.3c). (002) pole figure reveals only one peak in the out-of-plane direction (the tilted angle,  $\chi = 0^\circ$ ; the rotation angle,  $\varphi = 0^\circ$ ), proving a preferred  $\{001\}$  orientation in this direction. (022) pole figure reveals four strong peaks at  $\chi = 45^\circ$  and  $\varphi = 45^\circ$ ,  $135^\circ$ ,  $225^\circ$ ,  $315^\circ$ . The observed tilt of  $45^\circ$  perfectly matches to the theoretical angle between (002) and (022) planes for a cubic units cell. The appearance of four discrete peaks at  $\varphi$  increments of  $90^\circ$  indicates a high degree of in-plane orientation of the obtained  $\text{CoSi}_2$  film, suggesting a nearly perfect cube-on-cube epitaxial relationship between the film and Si substrate. XRD results show that single crystalline  $\text{CoSi}_2$  can be formed via this wet deposition method after annealing; the single  $\{100\}$  out-of-plane orientation is probably the result of the excellent epitaxial growth after direct  $\text{CoSi}_x$  formation on Si (100) substrate. The formation of  $\text{CoSi}_2$  after vacuum treatment is further confirmed by XAS based on a Si(0) model (Figure A.4.4c), which reveals the presence of ca. 99.2%  $\text{CoSi}_2$  and 0.8% Co(0). EDS mapping (Figure A.4.7) shows that after the treatment, a homogeneous layer contained Co (Figure A.4.8) and Si (Figure A.4.9) along with some contaminations as described before. Note that Co tends to diffuse into the Si substrate during the thermal treatment<sup>31</sup>, as shown in this case. AFM images of this layer reveals that  $R_{\text{rms}}$  drops to 5.3 nm (Figure 4.3d) after thermal annealing under vacuum, consistent with an improvement of the film homogeneity film in comparison with the as-synthesized  $\text{CoSi}_x$  layer (Figure 4.2b). Further, this value is greatly improved by comparison with  $\text{CoSi}_2$  ( $R_{\text{rms}} = 10.7$  nm, Figure 4.3e) prepared by physical method, which is due to the inter-diffusion of Co(0) metal and Si substrate during the typical rapid thermal annealing (RTA) process.<sup>32</sup>



**Figure 4.3.** (a) Scheme of the annealing process in this work; the condition as below: As-synthesize sample was annealed at 850 °C for 12 h under vacuum. (b) X-ray diffraction patterns of CoSi<sub>x</sub> on Si(100) substrate: As-synthesized sample (black curve), samples after a 850 °C (green curve) thermal vacuum treatment and reference CoSi<sub>2</sub> sample (blue curve) with Miller index shown for Si and CoSi<sub>2</sub> crystalline peaks. (c) Pole figures of (002) and (022) reflections of obtained CoSi<sub>2</sub> film. AFM images of CoSi<sub>x</sub> layer on the Si substrate: (d) sample after vacuum-treatment at 850 °C,  $R_{\text{rms}}=5.3$  nm; (e) conventional CoSi<sub>2</sub> on wafer,  $R_{\text{rms}}=10.7$  nm.

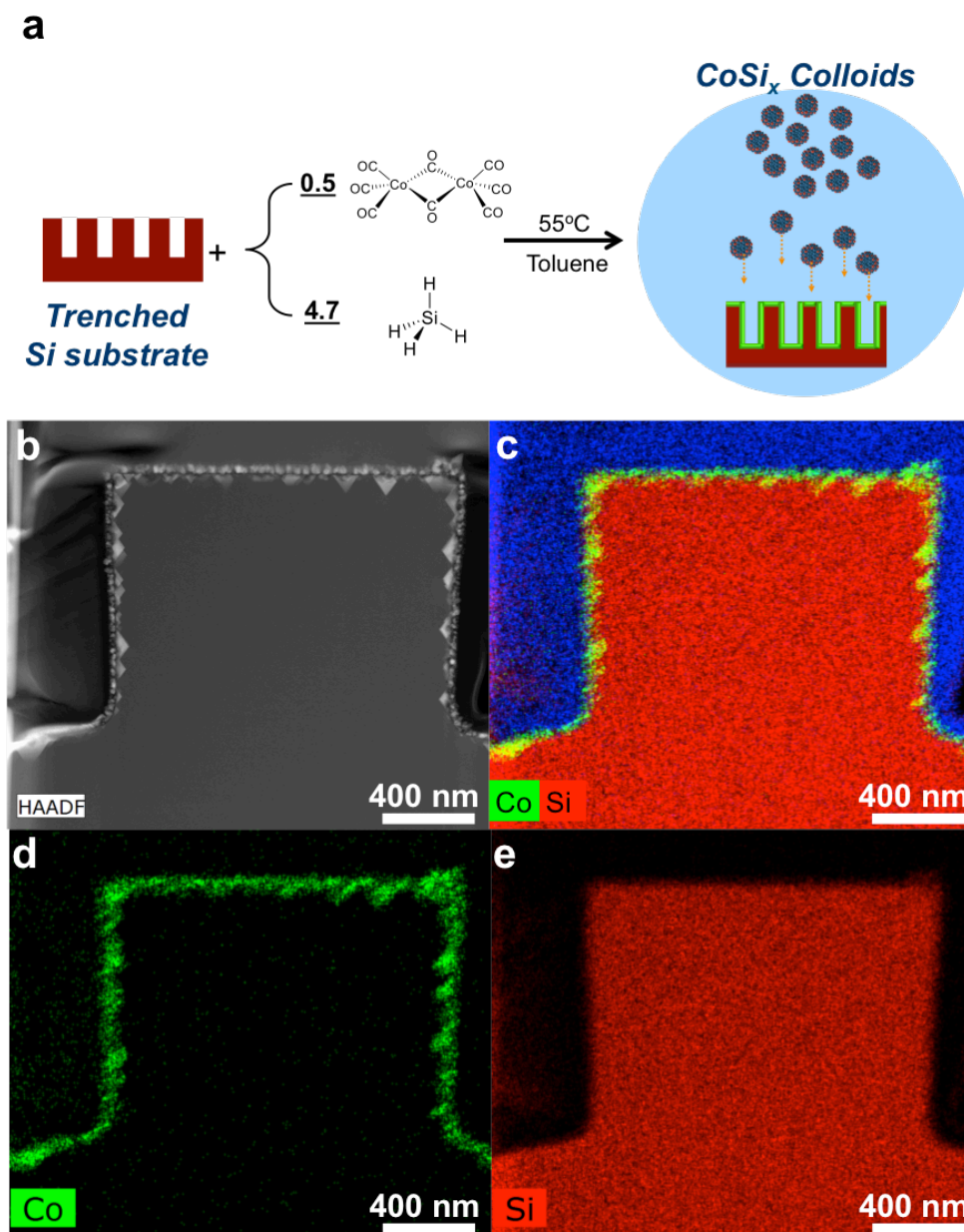


The I-V characteristics are also significantly improved, compared to that in Figure 4.2d. Figure 4.4a presents an Ohmic I-V behavior with a low resistivity of  $11.6 \mu\Omega\cdot\text{cm}$  (green line in Figure 4.4a). The I-V profile for the control  $\text{CoSi}_2$  film prepared by the conventional physical method is also attached (blue line in Figure 4.4a), which only exhibits a resistivity of  $55.6 \mu\Omega\cdot\text{cm}$ . We infer that the low resistivity could be due to the formation of single-crystalline  $\text{CoSi}_2$  (schematics see Figure 4.4b) upon thermal annealing, through healing the voids between amorphous nanoparticles, which directly benefit carrier transport.



**Figure 4.4.** (a) I-V characteristics of the  $\text{CoSi}_2$  layer deposited on a Si(100) wafer: Green line: sample after  $850^\circ\text{C}$  thermal vacuum-treatment; blue line: reference  $\text{CoSi}_2$  sample from conventional method. (b) Scheme of  $\text{CoSi}_2$  from chemical method compared with  $\text{CoSi}_2$  from conventional method.

Furthermore, this chemical method was utilized on trench-structured wafer to evaluate the conformality of this deposition method (reaction scheme shown as Figure 4.5a). The as-synthesized sample exhibited a conformal and homogeneous  $\text{CoSi}_x$  layer from EDS mapping, shown in Figure A.4.13-14. Also, HAADF and EDS mapping of the trenched sample after post-treatment (Figure 4.5b-e) reveals the formation of the conformal  $\text{CoSi}_2$  layer on the substrate (36-37 nm on all sides), illustrating that the post-treatment does not affect the homogenous coverage of the 3D-structure Si substrate. HAADF and EDS mapping also show that Co diffuses into Si substrate to produce nanometric  $\text{CoSi}_2$  pyramids within the interface between the  $\text{CoSi}_2$  layer and the substrate (Figure 4.5a).



**Figure 4.5.** (a) Reaction scheme for one-pot synthesis on trench-structured wafer, and the condition is as below:  $\text{Co}_2(\text{CO})_8/\text{die}$ ,  $110000 \text{ Co.nm}^{-2}$ ,  $\text{SiH}_4/\text{Co}=4.7$  with toluene at  $55^\circ\text{C}$  for 16 h. (b) HAADF and (c) EDS mapping image of the  $\text{CoSi}_2$  layer on the trench-structured Si substrate. (d-e) Co and Si EDS mapping images of the  $\text{CoSi}_2$  layer on the Si substrate, respectively.

### 4.3. Conclusion

In summary, this work has allowed for the conformal deposition of an amorphous  $\text{CoSi}_x$  layer on a Si substrate via the reaction of  $\text{Co}_2(\text{CO})_8$  and  $\text{SiH}_4$  in toluene at  $55^\circ\text{C}$ . Post-deposition thermal annealing under vacuum generates single crystalline

phase of  $\text{CoSi}_2$  with a  $\{001\}$ -preferred orientation onto the  $\text{Si}(100)$  substrate with a good surface roughness ( $R_{\text{rms}}=5.3$  nm), and displays metallic resistivity ( $11.6 \mu\Omega\cdot\text{cm}$ ; for bulk  $\text{Co}(0)$  metal:  $11.1 \mu\Omega\cdot\text{cm}$ ).<sup>22</sup> Therefore, this work establishes that molecular approaches are compatible with modern transistor fabrication technologies, which could also be applied on 3D-structured devices with minimal sizes. We are currently exploring this possibility.

#### **4.4. Experimental details**

**General information.** The experiments were carried out using Schlenk techniques. Toluene was dried and collected using a mBraun SBS-800 purification system and degassed by Schlenk techniques (vacuum to  $10^{-1}$  mbar and purged with dry Ar for 10 times). 40% HF solution was purchased from VWR.  $\text{Si}(0)$  nanopowder was purchased from US-nano with the size between 20-30 nm and with 98% purity.  $\text{Co}_2(\text{CO})_8$  were purchased from Strem and used as received. 1%  $\text{SiH}_4$  (N5.0) in helium was purchased from PanGas.  $\text{H}_2$  was purified over R3-11 BASF catalyst / MS 4 Å before use. Commercial  $\text{CoSi}_2$  (99%) powder was purchased from Alfa Aesar and used as received.

##### **Cobalt silicide colloidal nanoparticle synthesis on Si wafer (One-pot synthesis).**

Double side polished p-type 4" Si wafers with (100) orientations were diced into  $2 \text{ cm} \times 1 \text{ cm}$  dies, cleaned by a 40% HF solution for 60 s, and washed with DI water to remove excess HF. The diced wafers were then dried under high vacuum ( $\sim 10^{-5}$  mbar) at room temperature for 12 h.

A HF-treated diced Si-wafer and 12.4 mg  $\text{Co}_2(\text{CO})_8$  (0.04 mmol) were placed in a 325 mL Fischer-Porter bottle in a glovebox and dissolved in toluene (10 mL). The reactor was then pressurized under 2.7 bars of 1%  $\text{SiH}_4$  in He (0.33 mmol) and heated to  $55^\circ\text{C}$  for 16 h, during which a layer was formed on top of the Si-wafer accompanied by a dark solution (colloids formation). The colloidal solution was cannulated out of the reactor and the Si-wafer was washed 2 times with 10 mL of toluene. Prior storage inside glovebox, the as-synthesized wafer was dried under vacuum ( $\sim 10^{-2}$  mbar) for 3 h.

##### **Cobalt silicide layer via Co evaporation followed by the rapid-thermal-annealing on Si wafer (Conventional method).** Co metal layer was evaporated onto a HF-

treated p-type 4" Si wafer with the (100) orientation. Rapid-thermal-annealing was then conducted at 800 °C for 20 mins under H<sub>2</sub>/N<sub>2</sub> atmosphere, from which the CoSi<sub>2</sub> layer formed between the interface of Co and Si. Remaining Co metal layer was removed by washing in a piranha solution.

**Cobalt silicide colloidal nanoparticle synthesis on Si(0) nanopowder (One-pot synthesis).** 2.0 g of Si(0) nanopowder were reduced under a flow of pure hydrogen (100 mL.min<sup>-1</sup>) at 900 °C (1 °C.min<sup>-1</sup>) for 12 h to obtain a pristine Si-H surface (Figure S4b). 50 mg of Si(0) nanopowders and 46.5 mg Co<sub>2</sub>(CO)<sub>8</sub> (0.14 mmol) were placed in a 325 mL Fischer-Porter reactor in a glovebox and dissolved in toluene (10 mL). The reactor was then pressurized under 2.7 bar of 1% SiH<sub>4</sub> in He (0.45 mmol) and heated to 55 °C for 16 h, during which the solution color turned to black. Inside a glovebox, the Si-powder was separated from the solution using a filter and consecutively washed for 3 times with 10 mL of toluene. The Si-powder was dried under high vacuum (~10<sup>-5</sup> mbar) for 3 h.

**Vacuum-treatment condition.** As-synthesized wafer or nanopowders were treated under high vacuum (10<sup>-5</sup> mbar) at different temperature (350 °C, 500 °C, 700 °C or 850 °C, 1 °C.min<sup>-1</sup>) for 12 h.

### **Characterization Techniques.**

#### Transmission Electron Microscopy (TEM)

TEM images were taken with a FEI Tecnai Orisis ultrahigh vacuum transmission electron microscope. Energy-dispersive (EDS) detector was attached onto the FEI Tecnai Orisis for elemental mapping analysis.

#### TEM sample preparation by a tripod method

The as-synthesized wafer was cleaved into two pieces of 2.5 × 1.8 mm, which were glued face-to-face using a Gatan G2 epoxy glue. The specimen was then mounted on the side of a tripod polisher, which was heated at 100 °C. To remove most of the Si-bulk wafer, the polishing procedure was conducted using a series of plastic diamond lapping films, with grains of decreasing sizes (30 μm, 15 μm, 6 μm, 1 μm, 0.5 μm, and 0.1 μm) and a final step was polished on a felt-covered disc using the slurry of silica with 25 nm grain size. The specimen was then mounted on the bottom of a

tripod polisher, which was heated at 100 °C. The glass support was perfectly flat polished to ensure a correct 0.6° angle of the wedge shape specimen. The same polishing procedure was used for the bottom part leading to appearance of interference fringes (electron transparency), and then the specimen was glued on a Mo grid. After 12 h of drying, the grid was detached from the tripod using acetone to dissolve the glue, and the specimen was cleaned by acetone.

#### TEM sample preparation by focus-ion-beam (FIB) method

A TEM lamella was prepared by the in-situ lift-out technique on a Zeiss NVision 40 FIB-SEM. The lamella was thinned using 30 kV Ga<sup>+</sup>. For the 5 kV showering to reduce the thickness of the damage layer the lamella was tilted 10° into the beam.

#### Atomic Force Microscopy

The AFM measurements were conducted on a commercial AFM system (BioScope Catalyst, Bruker Nano, Santa Barbara, California) that is mounted onto an inverted confocal laser-scanning microscope (FluoView FV500, Olympus, Center Valley, Pennsylvania). The images shown in this study were obtained using tapping mode AFM with CT300R-25 cantilever probes (Nanoscience, USA). The AFM images are 2 μm<sup>2</sup> in size, with a resolution of 512 × 512 pixels, and a scan rate of 0.2 Hz.

#### Fourier Transformed Infrared Spectroscopy (FTIR)

FTIR spectra of wafers were recorded in transmission mode on Thermo Scientific, Nicolet 6700, in which the measurements were performed under inert condition with a deuterated triglycine sulfate (DTGS) detector with 1000 averaged scans to achieve an optimal signal-to-noise ratio. FTIR spectra of nanopowders were recorded in transmission mode on a Bruker ALPHA-T FTIR spectrophotometer under inert condition.

#### X-ray Photon Spectroscopy (XPS)

XPS depth profiles were recorded using a Kratos Axis Ultra DLD spectrometer with monochromic Al K<sub>α</sub> radiation (1486.6 eV). A commercial Kratos charge neutralizer was used to avoid non-homogeneous electric charge and to achieve better resolution. The resolution measured as full width at half maximum of the curve fitted photoemission peaks was approximately 1 eV. Binding energy (BE) values refer to the

Fermi edge and the energy scale was calibrated using Au 4f<sub>7/2</sub> at 84.0 eV and Cu 2p<sub>3/2</sub> at 932.67 eV. Samples were attached to a stainless-steel sample holder bar using a double-sided sticking Cu tape. XPS data were analyzed with CasaXPS software version 2313 Dev64. The C-C component of the C 1s peak was set to a binding energy of 284.8 eV to correct for the charging effect on each sample. The atomic concentrations of the elements in the near-surface region were estimated taking into account the corresponding Scofield atomic sensitivity factors and Inelastic Mean Free Path (IMFP) of photoelectrons using standard procedures in the CasaXPS software. Depth profiling was conducted by step by step sputtering of a sample with a Kratos polyatomic sputtering gun operating in Ar mode at 5 keV, I<sub>ion</sub> ≈ 1 μA. Thickness of the layers was calibrated using the TEM measured thickness.

#### X-ray Absorption Spectroscopy (XAS)

XAS data were carried out at the X10DA (Super XAS) beamline at the Swiss Light Source, Villigen, Switzerland. Spectra were collected on pressed pellets optimized to 1 absorption length at the Co K-edge in transmission mode. The beamline energy axis was calibrated with a Co reference foil, in which energies are measured at the inflexion point(s) of the absorption signal, and the precision on the energy of the edge is ± 0.5 eV in the (7659-7759 eV) area. The spectra were background-corrected using the Athena software package.

#### X-ray Diffraction Spectroscopy (XRD)

Samples were investigated by X-ray diffraction (XRD) using a PANalytical X'Pert Pro MRD diffractometer equipped with a parallel beam mirror and a point detector. XRD measurements in the  $\theta/2\theta$  geometry were performed for the phase analysis of the samples and to evaluate the out-of-plane preferential orientation. An incident angle offset of -0.2° was applied to reduce the contribution of the very strong Si(004) substrate reflection. Pole figure XRD measurements were carried out to study in detail the preferred crystallographic orientation of the samples. The pole figure measurements were performed for the CoSi<sub>2</sub> (002) and (022) reflections at 2 $\theta$  angles of ~33.5° and ~48.0°, respectively.

### Electrical performance evaluation

For four-point probe measurement, four 100 nm gold (Au) electrodes were deposited to a circle-shape layer (0.25 mm in radius; separate with each one by 1 mm) with a deposition rate of  $5 \pm 2 \text{ \AA} \cdot \text{s}^{-1}$  by thermal evaporation of Au ingots under high vacuum ( $\sim 10^{-5}$  mbar). The Au ingots (99.999%) were supplied by Kurt J. Lesker. A MBraun glovebox integrated MBraun vacuum thermal evaporator was used for the Au evaporation. The probe station used for I-V characteristic measurement is a Signatone S1160, and the I-V data were acquired by a Keysight B1500 with B1510A High Power source/monitor unit (HPSMU).

### **4.5. References**

1. Ilatikhameneh, H.; Ameen, T.; Novakovic, B.; Tan, Y.; Klimeck, G.; Rahman, R., Saving Moore's Law Down To 1 nm Channels With Anisotropic Effective Mass. *Scientific Reports* **2016**, *6*, 31501.
2. Franklin, A. D.; Luisier, M.; Han, S.-J.; Tulevski, G.; Breslin, C. M.; Gignac, L.; Lundstrom, M. S.; Haensch, W., Sub-10 nm Carbon Nanotube Transistor. *Nano Lett.* **2012**, *12* (2), 758-762.
3. Service, R. F., Is Silicon's Reign Nearing Its End? *Science* **2009**, *323* (5917), 1000-1002.
4. Yang, Y.; Ding, L.; Han, J.; Zhang, Z.; Peng, L.-M., High-Performance Complementary Transistors and Medium-Scale Integrated Circuits Based on Carbon Nanotube Thin Films. *ACS Nano* **2017**, *11* (4), 4124-4132.
5. Iwai, H., Roadmap for 22 nm and beyond. *Microelectron. Eng.* **2009**, *86* (7-9), 1520-1528.
6. Singh, N.; Agarwal, A.; Bera, L. K.; Liow, T. Y.; Yang, R.; Rustagi, S. C.; Tung, C. H.; Kumar, R.; Lo, G. Q.; Balasubramanian, N.; Kwong, D. L., High-performance fully depleted silicon nanowire (diameter /spl les/ 5 nm) gate-all-around CMOS devices. *IEEE Electron Device Lett.* **2006**, *27* (5), 383-386.
7. Xu, J.; Oksenberg, E.; Popovitz-Biro, R.; Rechav, K.; Joselevich, E., Bottom-Up Tri-gate Transistors and Submicrosecond Photodetectors from Guided CdS Nanowalls. *J. Am. Chem. Soc.* **2017**, *139* (44), 15958-15967.
8. Tomioka, K.; Yoshimura, M.; Fukui, T., A III-V nanowire channel on silicon for high-performance vertical transistors. *Nature* **2012**, *488*, 189.

9. Cress, C. D.; Datta, S., Nanoscale Transistors—Just Around the Gate? *Science* **2013**, *341* (6142), 140-141.
10. Ferain, I.; Colinge, C. A.; Colinge, J.-P., Multigate transistors as the future of classical metal–oxide–semiconductor field-effect transistors. *Nature* **2011**, *479*, 310.
11. Chen, J.; Colinge, J. P.; Flandre, D.; Gillon, R.; Raskin, J. P.; Vanhoenacker, D., Comparison of  $\text{TiSi}_2$ ,  $\text{CoSi}_2$ , and  $\text{NiSi}$  for Thin-Film Silicon-on-Insulator Applications. *J. Electrochem. Soc.* **1997**, *144* (7), 2437-2442.
12. Chiu, S.-P.; Yeh, S.-S.; Chiou, C.-J.; Chou, Y.-C.; Lin, J.-J.; Tsuei, C.-C., Ultralow 1/f Noise in a Heterostructure of Superconducting Epitaxial Cobalt Disilicide Thin Film on Silicon. *ACS Nano* **2017**, *11* (1), 516-525.
13. Zimmermann, S.; Zhao, Q. T.; Höhnemann, H.; Wiemer, M.; Kaufmann, C.; Mantl, S.; Dudek, V.; Gessner, T., Roughness improvement of the  $\text{CoSi}_2/\text{Si}$ -interface for an application as buried silicide. *Microelectron. Eng.* **2007**, *84* (11), 2537-2541.
14. Zaera, F., The Surface Chemistry of Atomic Layer Depositions of Solid Thin Films. *The Journal of Physical Chemistry Letters* **2012**, *3* (10), 1301-1309.
15. George, S. M., Atomic Layer Deposition: An Overview. *Chem. Rev.* **2010**, *110* (1), 111-131.
16. Zaera, F., The surface chemistry of thin film atomic layer deposition (ALD) processes for electronic device manufacturing. *J. Mater. Chem.* **2008**, *18* (30), 3521-3526.
17. Kagan, C. R.; Lifshitz, E.; Sargent, E. H.; Talapin, D. V., Building devices from colloidal quantum dots. *Science* **2016**, *353* (6302).
18. Talapin, D. V.; Lee, J.-S.; Kovalenko, M. V.; Shevchenko, E. V., Prospects of Colloidal Nanocrystals for Electronic and Optoelectronic Applications. *Chem. Rev.* **2010**, *110* (1), 389-458.
19. and, C. B. M.; Kagan, C. R.; Bawendi, M. G., Synthesis and Characterization of Monodisperse Nanocrystals and Close-Packed Nanocrystal Assemblies. *Annual Review of Materials Science* **2000**, *30* (1), 545-610.
20. Baudouin, D.; Szeto, K. C.; Laurent, P.; De Mallmann, A.; Fenet, B.; Veyre, L.; Rodemerck, U.; Copéret, C.; Thieuleux, C., Nickel–Silicide Colloid Prepared under Mild Conditions as a Versatile Ni Precursor for More Efficient  $\text{CO}_2$  Reforming of  $\text{CH}_4$  Catalysts. *J. Am. Chem. Soc.* **2012**, *134* (51), 20624-20627.
21. Lin, T.-H.; Margossian, T.; De Marchi, M.; Thammasack, M.; Zemlyanov, D.; Kumar, S.; Jagielski, J.; Zheng, L.-Q.; Shih, C.-J.; Zenobi, R.; De Micheli, G.;



- Baudouin, D.; Gaillardon, P.-E.; Copéret, C., Low-Temperature Wet Conformal Nickel Silicide Deposition for Transistor Technology through an Organometallic Approach. *ACS Appl. Mater. Interfaces* **2017**, *9* (5), 4948-4955.
22. De Vries, J. W. C., Temperature and thickness dependence of the resistivity of thin polycrystalline aluminium, cobalt, nickel, palladium, silver and gold films. *Thin Solid Films* **1988**, *167* (1), 25-32.
23. Kolomiitsova, T. D.; Savvateev, K. F.; Shchepkin, D. N.; Tokhadze, I. K.; Tokhadze, K. G., Infrared Spectra and Structures of SiH<sub>4</sub> and GeH<sub>4</sub> Dimers in Low-Temperature Nitrogen Matrixes. *The Journal of Physical Chemistry A* **2015**, *119* (11), 2553-2561.
24. London, J. W.; Bell, A. T., Infrared spectra of carbon monoxide, carbon dioxide, nitric oxide, nitrogen dioxide, nitrous oxide, and nitrogen adsorbed on copper oxide. *J. Catal.* **1973**, *31* (1), 32-40.
25. Bernal-Ramos, K.; Saly, M. J.; Kanjolia, R. K.; Chabal, Y. J., Atomic Layer Deposition of Cobalt Silicide Thin Films Studied by in Situ Infrared Spectroscopy. *Chem. Mater.* **2015**, *27* (14), 4943-4949.
26. Sciortino, L.; Giannici, F.; Martorana, A.; Ruggirello, A. M.; Liveri, V. T.; Portale, G.; Casaletto, M. P.; Longo, A., Structural Characterization of Surfactant-Coated Bimetallic Cobalt/Nickel Nanoclusters by XPS, EXAFS, WAXS, and SAXS. *The Journal of Physical Chemistry C* **2011**, *115* (14), 6360-6366.
27. Ono, L. K.; Behafarid, F.; Cuenya, B. R., Nano-Gold Diggers: Au-Assisted SiO<sub>2</sub>-Decomposition and Desorption in Supported Nanocatalysts. *ACS Nano* **2013**, *7* (11), 10327-10334.
28. Reddy, B. M.; Khan, A.; Yamada, Y.; Kobayashi, T.; Loridant, S.; Volta, J.-C., Surface Characterization of CeO<sub>2</sub>/SiO<sub>2</sub> and V<sub>2</sub>O<sub>5</sub>/CeO<sub>2</sub>/SiO<sub>2</sub> Catalysts by Raman, XPS, and Other Techniques. *The Journal of Physical Chemistry B* **2002**, *106* (42), 10964-10972.
29. Vander Wal, R. L.; Bryg, V. M.; Hays, M. D., XPS Analysis of Combustion Aerosols for Chemical Composition, Surface Chemistry, and Carbon Chemical State. *Anal. Chem.* **2011**, *83* (6), 1924-1930.
30. Lee, H.; Keun Lee, Y.; Nghia Van, T.; Young Park, J., Nanoscale Schottky behavior of Au islands on TiO<sub>2</sub> probed with conductive atomic force microscopy. *Appl. Phys. Lett.* **2013**, *103* (17), 173103.

31. Wang, H.; Zhang, Z.; Wong, L. M.; Wang, S.; Wei, Z.; Li, G. P.; Xing, G.; Guo, D.; Wang, D.; Wu, T., Shape-Controlled Fabrication of Micro/Nanoscale Triangle, Square, Wire-like, and Hexagon Pits on Silicon Substrates Induced by Anisotropic Diffusion and Silicide Sublimation. *ACS Nano* **2010**, *4* (5), 2901-2909.
32. Diale, M.; Challens, C.; Zingu, E. C., Cobalt self-diffusion during cobalt silicide growth. *Appl. Phys. Lett.* **1993**, *62* (9), 943-945.

## Chapter 5:

### Conclusions and Outlook

#### 5.1. Conclusions

This PhD thesis has contributed to the development of the chemical colloidal approach for the metal silicide formation. Detailed material characterizations and electrical measurement have been performed to have an overall understanding of the metal silicide layer formed via the colloidal approach (thickness, elemental composition, crystallinity, phase determination, surface roughness) in relation with its electrical properties via different microscopic and spectroscopic techniques.

Chapter 2 has focused on the development of a colloidal approach to generate a layer on Si (100) wafer using  $\text{Ni(COD)}_2$  and  $\text{SiH}_4$  as molecular precursors. This approach yields  $\sim 150$  nm homogeneous and amorphous  $\text{NiSi}_x$  layer on top of the Si substrate along with 2.8 nm colloids remaining in solution. Based on XPS data, the as-synthesized  $\text{NiSi}_x$  layer is composed of 36% carbon, which probably results from the hydrosilylation reaction of  $\text{SiH}_4$  and the cyclooctadiene ligand of  $\text{Ni(COD)}_2$ . While a subsequent treatment at higher temperature under  $\text{H}_2$  removes most of the carbon contaminations, it does not allow obtaining adequate electric properties, showing a Schottky barrier height of 0.41 eV and a resistivity of  $170 \mu\Omega\cdot\text{cm}$ . Using Si(0) nanoparticles as models show that the layer is composed of  $\text{NiSi}_2$  after post treatment at  $700^\circ\text{C}$  under  $\text{H}_2$  according to XAS. While  $\text{NiSi}_2$  should exhibit a conductor behaviour, the synthesized  $\text{NiSi}_2$  layer displays an energy barrier of 0.41 eV, which probably implies the presence of conductive and insulating domain, probably voids, likely formed upon removal of the hydrocarbon species. These voids impede the electron transfer in the layer.

We have thus investigated the use of an alternative Ni molecular precursor in Chapter 3, namely  $\text{Ni}[\text{N}(\text{SiMe}_3)(2,6\text{-iPr}_2\text{C}_6\text{H}_3)]_2$ , which contains ligands that cannot readily polymerize in contrast to COD. The reaction of  $\text{Ni}[\text{N}(\text{SiMe}_3)(2,6\text{-iPr}_2\text{C}_6\text{H}_3)]_2$  and  $\text{SiH}_4$  also yields a homogeneous 85 nm layer, with a lower carbon content in the as-synthesized layer (13% based on the XPS depth profile) by comparison with the layer obtained using  $\text{Ni(COD)}_2$  ( $\sim 36\%$  in Chapter 2). After the removal of residual hydrocarbon species by the post treatment at  $700^\circ\text{C}$  under  $\text{H}_2$ , the I-V characteristic


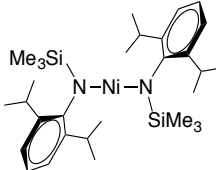
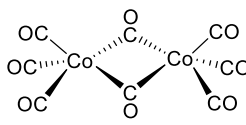
improves, but a Schottky behaviour with a Schottky barrier height of 0.4 eV and a low resistivity of 24  $\mu\Omega\cdot\text{cm}$  is still present. These results indicate that carefully selecting a nickel precursor is key to obtain improved electrical characteristic and requires further research.

In parallel, cobalt silicide formation via chemical colloidal reaction on Si (100) wafer was also investigated (Chapter 4) since this metal silicide displays the lowest resistivity among all metal silicides used for transistors. Herein,  $\text{Co}_2(\text{CO})_8$  was selected as the Co precursor due to the presence of CO ligands, which can be in principle easily removed upon thermal treatment at high temperature and under vacuum. The reaction of  $\text{Co}_2(\text{CO})_8$  and  $\text{SiH}_4$  in toluene at 55 °C generates a 20-nm homogeneous  $\text{CoSi}_x$  layer along with 3.5 nm colloids remaining in the solution. XPS analysis shows that the carbon content in the as-synthesized layer is 8%, which is comparable with the carbon content measured on the pristine Si wafer. This as-synthesized layer still shows a typical Schottky behaviour from the I-V curve, which likely results from the amorphous nature of this layer prepared via a low-temperature chemical colloidal approach. However, post-treatment at 850 °C under vacuum generates crystalline cobalt silicide layer, with formation of a (001)-oriented crystalline  $\text{CoSi}_2$  layer with a low surface roughness of 5.3 nm. The I-V measurement shows that this  $\text{CoSi}_2$  layer has Ohmic behaviour with a lower resistivity of 12  $\mu\Omega\cdot\text{cm}$  compared to the  $\text{CoSi}_2$  layer from conventional PVD method, which is 56  $\mu\Omega\cdot\text{cm}$ . This greatly improved electric performance has been attributed to the formation of an oriented crystallinity combined with a low surface roughness.

Hydrogen-terminated and trenched-structure Si (100) wafers have also been used as the substrate for the cobalt silicide synthesis in order to evaluate the formation of layers with good conformality on the 3D structure. After reaction of  $\text{Co}_2(\text{CO})_8$  and  $\text{SiH}_4$  in toluene at 55 °C, the as-synthesized layer shows a very good uniformity all around the trenched structure with the same thickness. The post-treatment at 850 °C under vacuum does not alter the conformality of the layer. Therefore, this work confirms that by selecting the easily removed ligands, like CO, on the metal precursor, the desired conformal metal silicide layer with the conductor behaviour can be achieved.

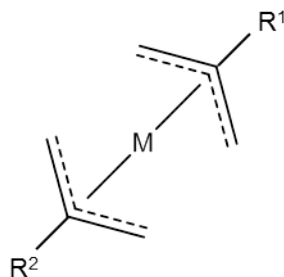
Overall, this PhD thesis has established a new methodology for forming metal silicide layers on Si (100) wafer via a chemical colloidal approach. The chemical colloidal reaction has been carried out using three metal precursors with different ligands. From the TEM and AFM results, the prepared layers are homogeneous and conformal; yet at the nanometer scale, one can observe surface roughness, which is likely induced by the deposition of clusters as the layer grows. Based on these experimental results, we propose that the main mechanism of layer deposition on the Si substrate depends on the layer-by-layer growth via the hydrosilation reaction between Si-H bond on the surface and the metal precursor. However, the small amounts of surface clusters likely result from the deposition and further reaction of colloidal nanoparticles or small clusters onto the Si substrate. It is noteworthy that the nanoparticles formed in solution do not deposit on the substrate, which is likely due to the poor affinity between the surface ligands on the nanoparticles and the Si substrate. After layer deposition, XPS shows that the carbon contents range from 8% to 36% depending on the metal precursors. X-ray techniques, such as XRD and XAS on Si(0) model reveal the formation of amorphous metal silicide after the layer preparation, which can crystallize upon high temperature treatment ( $\text{NiSi}_2$  in Chapter 2-3 vs.  $\text{CoSi}_2$  in Chapter 4). Then, detailed I-V measurements reveal the critical effect of the structure of the metal precursors on the final electrical behaviour as summarized in Table 5.1.

**Table 5.1** Comparison of the used metal precursor in this PhD thesis

<b>Metal Precursor</b>			
<b>Ligands</b>	Cyclooctadiene	Amido	Carbonyl
<b>As-synthesized carbon ratio (at%)</b>	36%	13%	8%
<b>Post-treated I-V characteristic</b>	Shottcky	Shottcky	Ohmic

## 5.2. Outlooks

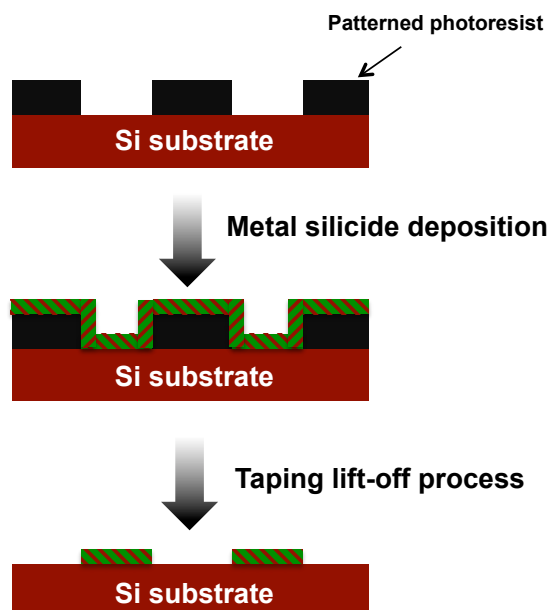
This PhD thesis provides an overall investigation of the chemical structures and electrical properties of the metal silicide layer from the colloidal approach, which creates a new route for future microelectronic design in order to keep the Moore's law moving forward. It has shown that the nature of the metal precursor is crucial for obtaining a good metal conductivity for the metal silicide layer when prepared via a colloidal reaction. Therefore, to achieve desired electrical properties, it is necessary to use metal complexes with tailored ligands, which can be easily removed under reaction conditions or post-treatment without leaving carbon residues. Carbonyl ligands have shown to be ideal for the synthesis of cobalt silicides. However, preliminary work using  $\text{Ni(CO)}_4$  has shown that this approach is not general as no colloids are formed after reaction under standard conditions. Other potential precursor candidates are needed. One possibility would be metal allyl complexes (Figure 5.1) as these ligands are ubiquitous in organometallic chemistry and are used to stabilize a broad range of transition metals, such as palladium, rhodium, and nickel.<sup>1, 2</sup> These complexes are typically soluble in non-coordinating solvent; allyl-type ligands should be quite reactive under reaction conditions ( $\text{SiH}_4$ ) to produce the corresponding silicide and light olefins that can be removed.



**Figure 5.1.** Proposed chemical structure of the metal-allyl complex.

Besides, the generation of phosphorus-doped (P-doped) semiconductor has also been investigated due to the capability of increasing the conductivity of semiconductors.<sup>3, 4</sup> Preliminary results on phosphorus doping in the nickel silicide layer show that the conductivity can be improved by phosphorus doping using a colloidal approach via the reaction of  $\text{Ni(COD)}_2$  (0.07 mmol) and  $\text{SiH}_4$  (0.33 mmol) in toluene at 55 °C with 0.01 mmol  $\text{PH}_3$  on Si (100) wafer (see appendix). However, after reaction, the layer still exhibits a Schottky barrier height of 0.5 eV and a low sheet resistance of 1.0  $\Omega$  due to carbon contamination. This strategy should be applied to Co and possibly other metal/ligand sets.

For the further development towards an industrial process, it is necessary to apply this methodology onto the Si wafer with patterned structure, which includes the extra step of photoresist stripping. Generally, the photoresist is composed of polymers, such as poly(methyl methacrylate) (PMMA) or polyphthalamide (PPA). In order to remove the photoresist after the conventional silicidation process, organic solvents are used to wash away the polymer without attacking the metal silicide layer. However, in our case, due to the amorphous nature of the as-synthesized metal silicide layer, it is not readily applicable since the layer would likely react with most organic solvents used in the conventional photoresist stripping process (e.g. acetone). However, lift-off process, used for graphene,<sup>5</sup> should be suitable because it does not involve complex chemical treatment, which can damage the metal silicide layer. The concept of tapping process on our device is exemplified in Figure 5.2. Then, the properties of the patterned layer can be fully understood and evaluated for further application based on the established methodology in this PhD thesis.



**Figure 5.2.** Proposed process flow for the taping lift-off techniques.

### 5.3. References

1. Ma, S., Some Typical Advances in the Synthetic Applications of Allenes. *Chem. Rev.* **2005**, *105* (7), 2829-2872.
2. Bai, T.; Ma, S.; Jia, G., Insertion reactions of allenes with transition metal complexes. *Coord. Chem. Rev.* **2009**, *253* (3), 423-448.
3. Zhang, Y.; Mori, T.; Ye, J.; Antonietti, M., Phosphorus-Doped Carbon Nitride Solid: Enhanced Electrical Conductivity and Photocurrent Generation. *J. Am. Chem. Soc.* **2010**, *132* (18), 6294-6295.
4. Norris, D. J.; Efros, A. L.; Erwin, S. C., Doped Nanocrystals. *Science* **2008**, *319* (5871), 1776-1779.
5. Novoselov, K. S.; Geim, A. K.; Morozov, S. V.; Jiang, D.; Zhang, Y.; Dubonos, S. V.; Grigorieva, I. V.; Firsov, A. A., Electric Field Effect in Atomically Thin Carbon Films. *Science* **2004**, *306* (5696), 666-669.

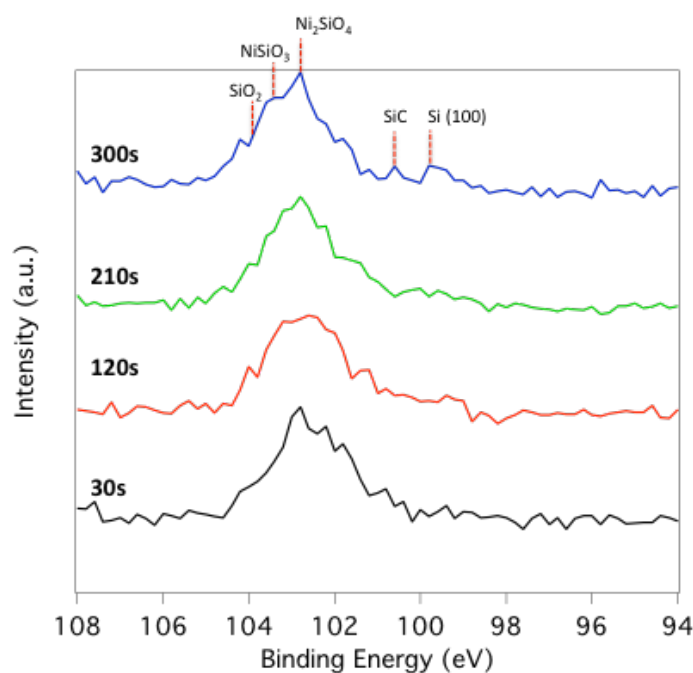


## **Appendix A: Annexes**

## A.2. Appendix to Chapter 2.

### Surface oxidation effect due to ex-situ transferring to XPS

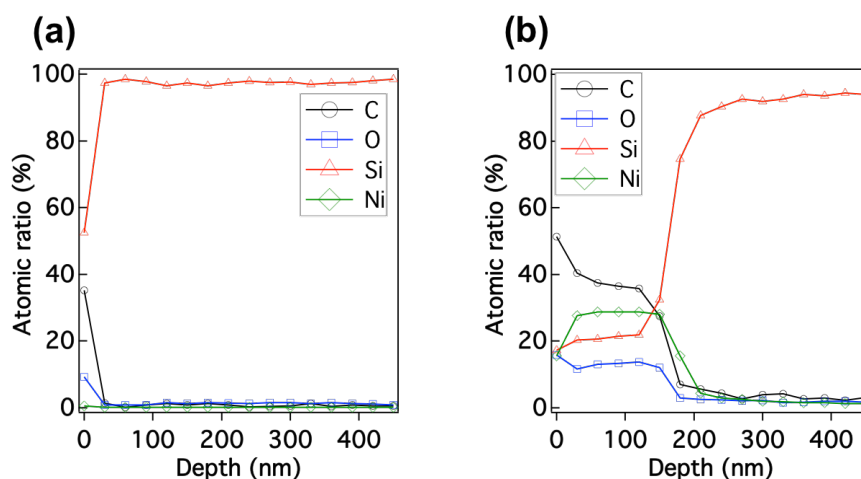
Figure A.2.1 shows the XPS Si 2p spectra of the Ni-rich layer captured at different sputtering time during a 10 nm/min depth profiling analysis. The spectra range from the black line after 30 seconds to the blue line for 5 minutes; it shows that there was a homogeneous film in depth after the one-pot synthesis. It also indicates that, after exposure to air, the layer was mainly composed of oxidized NiSi<sub>x</sub>. From data fitting made on the spectrum obtained after 300 s sputtering, the peaks in it are at 101.7 eV (17%), 102.2 eV (7%), 102.8 eV (39%), 103.5 eV (32%), and 104.2 eV (4%), in which the major peaks are assigned to the oxidized Si in the form of Ni<sub>2</sub>SiO<sub>4</sub> (102.8 eV, 39%) and NiSiO<sub>3</sub> (103.50 eV, 32%), respectively.



**Figure A.2.1.** X-ray photoelectron spectra of Si 2p at different sputtering times.

## Element background analysis by XPS depth profile

Figure A.2.2 and Table A.2.1 compares the XPS depth profiling of a pristine wafer and our wafer after one-pot synthesis. The reference of surface contamination was measured on the pristine wafer, which contains 18% carbon and 5% oxygen.



**Figure A.2.2.** XPS depth profiles of Pristine and Ni-rich layer on the Si substrate. **(a)** Pristine wafer. **(b)** As-synthesized Ni-rich layer on the Si substrate. Note that the Si wafers underwent the same cleaning procedure, i.e. 40% HF cleaning, drying under high vacuum, and wafers were stored under inert atmosphere.

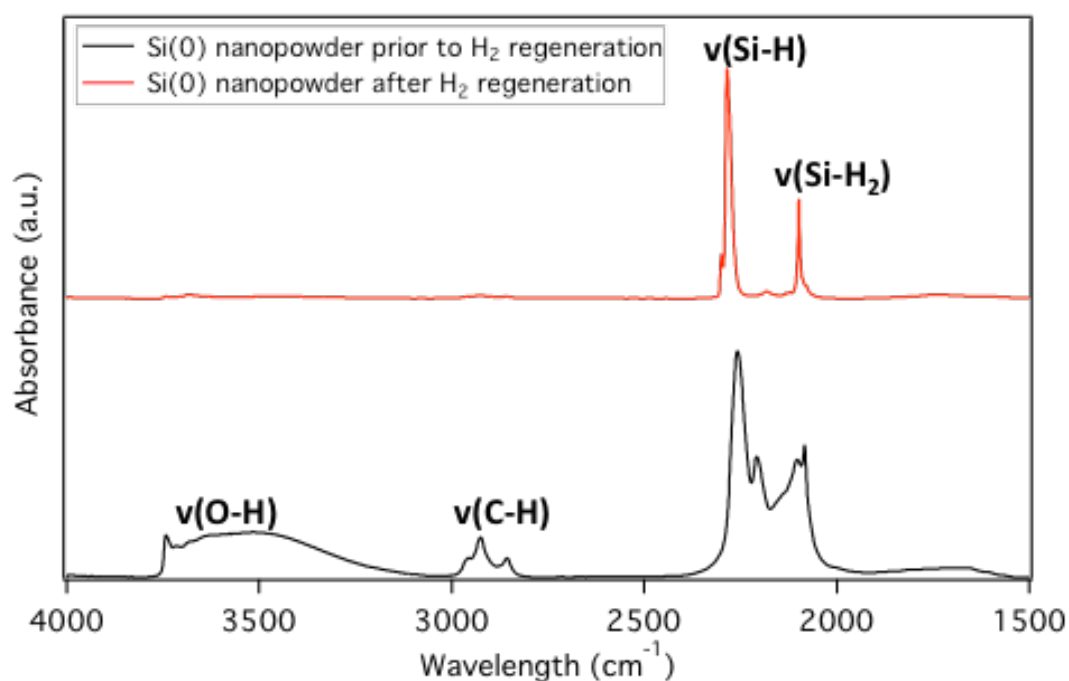
**Table A.2.1.** Quantitative XPS depth profiles of Ni-rich layer on the Si substrate with pristine Si wafer as reference.

Condition	Nickel [%]	Silicon [%]	Carbon [%]	Oxygen [%]
Pristine <sup>a)</sup>	0	75	18	5
As-syn <sup>b)</sup>	22	19	46	13

<sup>a)</sup>Pristine Si substrate, the surface atomic ratio was counted in the first 30 nm; <sup>b)</sup>as-synthesized sample, the atomic ratio was averaged in the first 30 nm

### Surface characterization of thermal-treated Si(0) nanopowder by FTIR

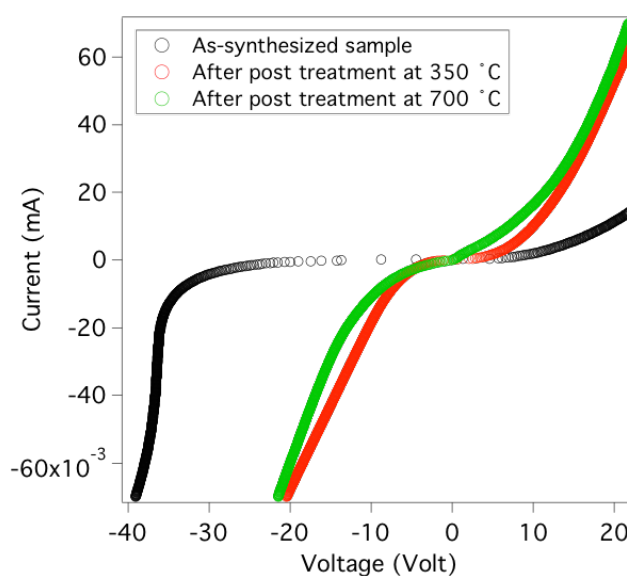
Figure A.2.3 shows that there are only 2 kinds of Si-H bonds on the surface. One is Si-H stretch signal on  $2280\text{ cm}^{-1}$ , and another is  $\text{SiH}_2$  stretch signal on  $2100\text{ cm}^{-1}$ . It indicates that after hydrogen regeneration, the surface of Si(0) nanopowder was solely terminated by Si-H.



**Figure A.2.3.** Transmission FTIR analysis of Si(0) nanopowder before and after  $\text{H}_2$  regeneration.  $\text{NiSi}_x$  layer on the as-synthesized wafer (red line), and the pristine Si wafer (black line).

### I-V characteristics of NiSi<sub>x</sub> samples

The NiSi<sub>x</sub> layers exhibit a rectifying behavior, which indicates that there are space charges between NiSi<sub>x</sub> nanoparticles (Figure A.2.4). For the as-synthesized sample, more obvious rectifying characteristics are found compared to the samples after post-treatment, indicating that, in the as-synthesized sample, electrons have to overcome larger energy barrier. After post-treatment, the rectifying behavior is less obvious, as shown by the decreased depletion area (Figure A.2.4). This observation indicates the largely reduced space charges, which probably induce the lower series resistance from 371.8 to 8.5 (Table 2.2). Moreover, the reduced rectifying characteristics in the post-treated samples result in the higher ideality factor along with the lower series resistance (Table 2.2).



**Figure A.2.4.** I-V characteristics of NiSi<sub>x</sub> layer on the Si(100) wafer. Black circles: As-synthesized wafer; red circles: sample after 350 °C post-treatment; green circles: sample after 700 °C post-treatment.

### Calculation method of the thermionic emission equation

$$I_a = AA_0 T^2 e^{-\frac{\Phi_n}{k_B T}} \left[ e^{-\frac{e_0(V-R_s I_a)}{\eta k_B T}} - 1 \right], \quad (\text{A.2.1})$$

$I_a$  : applied current (A)

$V$  : measured voltage (V)

$A$  : active area ( $7.8 \times 10^{-7} \text{ m}^2$ )

$A_0$  : effective Richardson constant ( $1.20 \times 10^6 \text{ A.m}^{-2}\text{K}^{-2}$ )

$T$  : temperature of the measurement (298K)

$k_B$  : the Boltzmann constant ( $8.62 \times 10^5 \text{ eV/K}$ )

$\Phi_n$  : Schottky barrier height (eV)

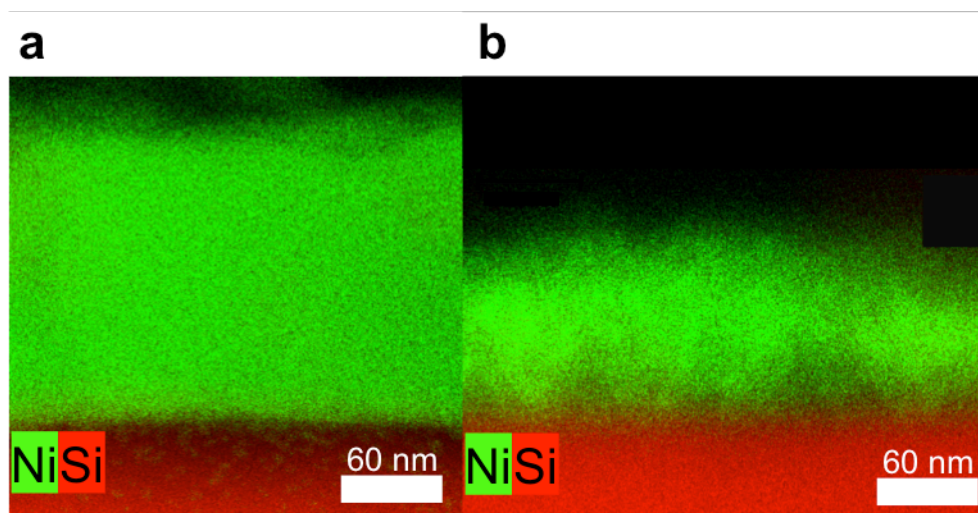
$\eta$  : the ideality factor

$R_s$  : the series resistance ( $\Omega$ )

Fitting the positive part of the  $I_a$  and  $V$  curve, the nonlinear least-squares method was used on the thermionic emission equation (Eq. A.2.1), providing  $\Phi_n$ ,  $\eta$ , and  $R_s$  shown in Table 2.2.

### TEM-EDS mapping of as-synthesized sample and after post-treatment at 700 °C

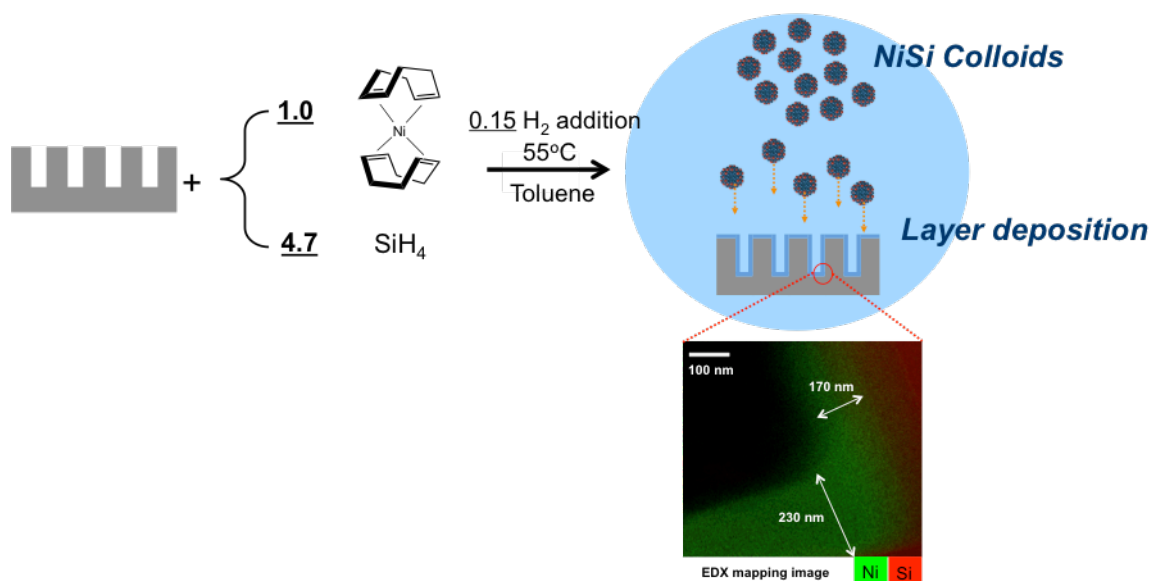
From Figure A.2.5a, it indicates that for as-synthesized sample, a homogeneous layer is deposited on the Si substrate. However, after thermal treatment (Figure A.2.5b), due to the diffusion effect, the layer becomes thinner and with more voids inside because of the removal of carbon contaminations.



**Figure A.2.5.** TEM-EDS Ni/Si mapping image of the NiSi<sub>x</sub> layer on the Si substrate. (a) as-synthesized wafer; (b) wafer with post-treatment at 700 °C in H<sub>2</sub> flow.

### One-pot chemical approach on 3D-structured Si wafer

Figure A.2.6 shows the experimental scheme and the EDS mapping result of the as-synthesized sample from the same one-pot method. After reaction, there is a homogeneous  $\text{NiSi}_x$  layer covered on the trenched Si wafer with the step coverage of 0.74.

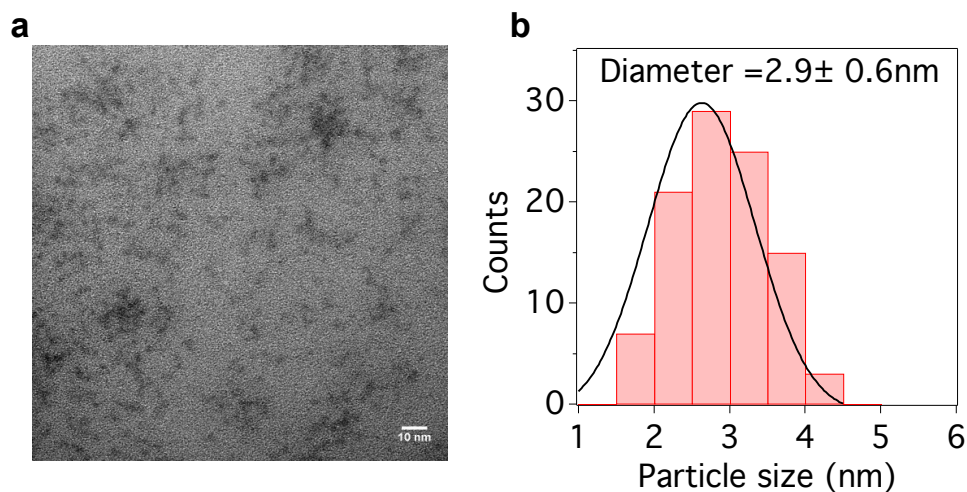


**Figure A.2.6.** Reaction scheme for one-pot synthesis, and the condition is as below:  $\text{Ni(COD)}_2/\text{die}$ ,  $110000 \text{ Ni.nm}^{-2}$ ,  $\text{SiH}_4/\text{Ni}=4.7$  with  $0.01 \text{ mmol H}_2$ , toluene,  $55^\circ\text{C}$  for 16 h with EDS mapping image for Ni and Si of the Ni-rich layer on the trenched-Si substrate. The wafer was exposed to air prior to analysis.



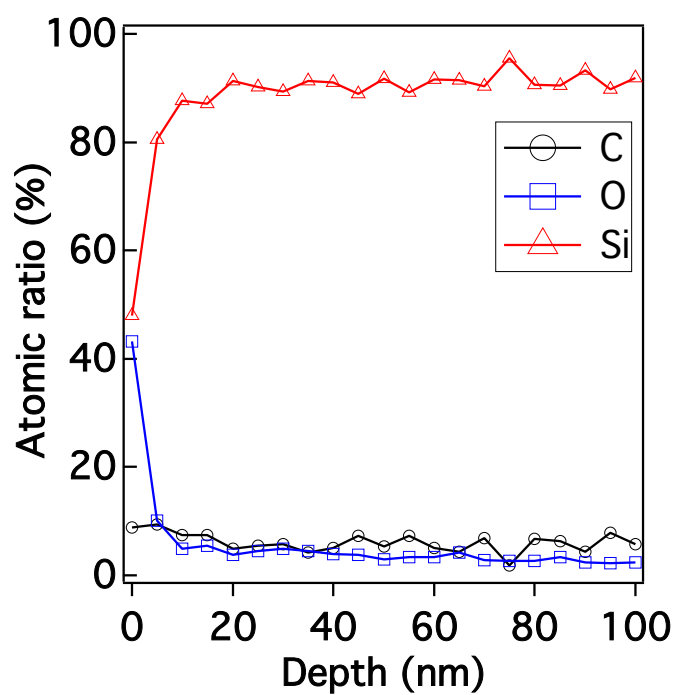
### A.3. Appendix to Chapter 3.

**TEM image for the colloidal nanoparticles.** After reaction, there is a colloidal solution containing 3.5 nm colloids inside (Figure A.3.1a-A.3.1b).



**Figure A.3.1.** (a) TEM image of colloidal nanoparticles formed after chemical one-pot synthesis. and (b) Calculated averaged size distribution in (a).

### Element background analysis by XPS depth profile.



**Figure A.3.2.** XPS depth profile of a pristine wafer. Note that the substrate underwent the cleaning procedure, i.e. 40% HF cleaning, drying under high vacuum, and wafers were stored under inert atmosphere.

**Calculation method of the thermionic emission equation.** The thermionic emission model (A.3.1) is used to fit the I-V curve of the as-synthesized sample (Figure 3.2d).

$$I_a = AA_0 T^2 e^{-\frac{\Phi_n}{k_B T}} \left[ e^{-\frac{e_0(V-R_s I_a)}{\eta k_B T}} - 1 \right], \quad (\text{A.3.1})$$

$I_a$  : applied current (A)

$V$  : measured voltage (V)

$A$  : active area ( $7.8 \times 10^{-7} \text{ m}^2$ )

$A_0$  : effective Richardson constant ( $1.20 \times 10^6 \text{ A.m}^{-2}\text{K}^{-2}$ )

$T$  : temperature of the measurement (298K)

$k_B$  : the Boltzmann constant ( $8.62 \times 10^{-5} \text{ eV/K}$ )

$\Phi_n$  : Schottky barrier height (eV)

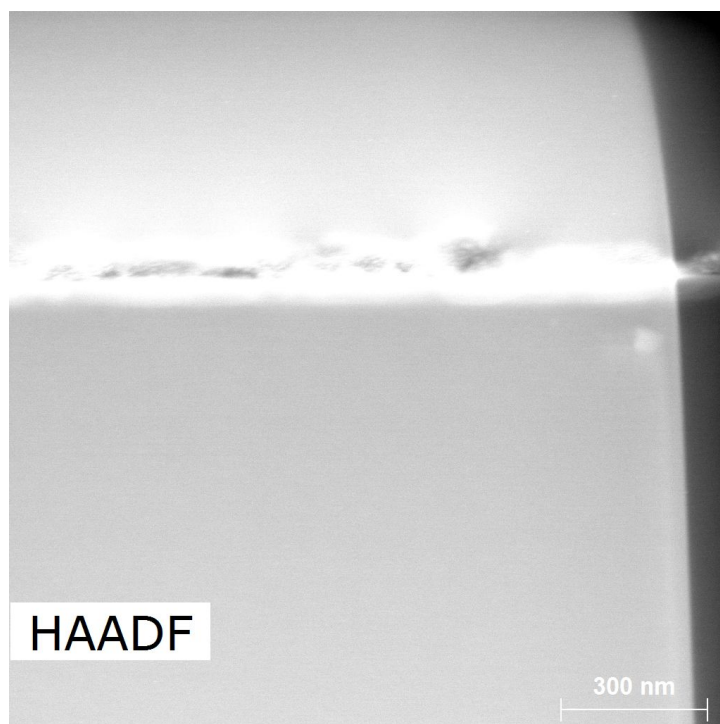
$\eta$  : the ideality factor

$R_s$  : the series resistance ( $\Omega$ )

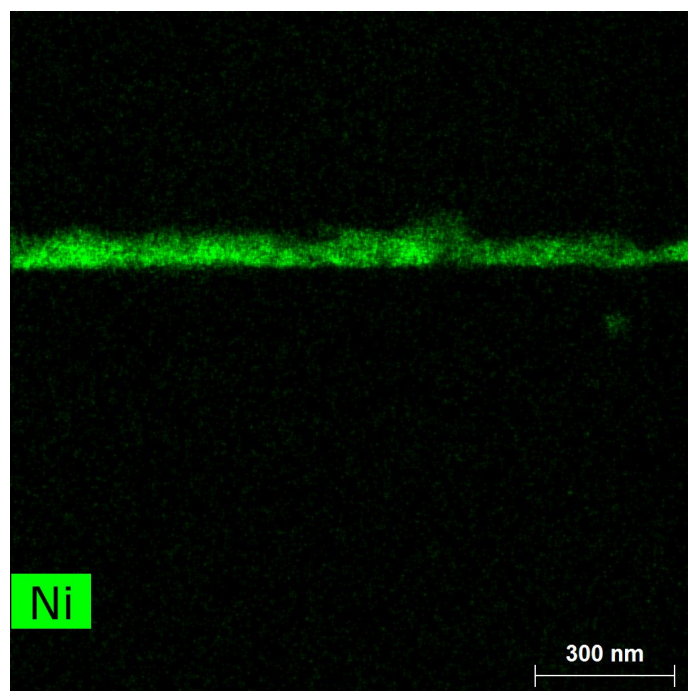
Fitting the positive part of the  $I_a$  and  $V$  curve, the nonlinear least-squares method was used on the thermionic emission equation (Eq. A.3.1), providing  $\Phi_n$ ,  $\eta$ , and  $R_s$ .

The fitted Schottky barrier height and the series resistance are 0.64 eV and 5.4  $\Omega$ , respectively, with the ideality factor of 149.

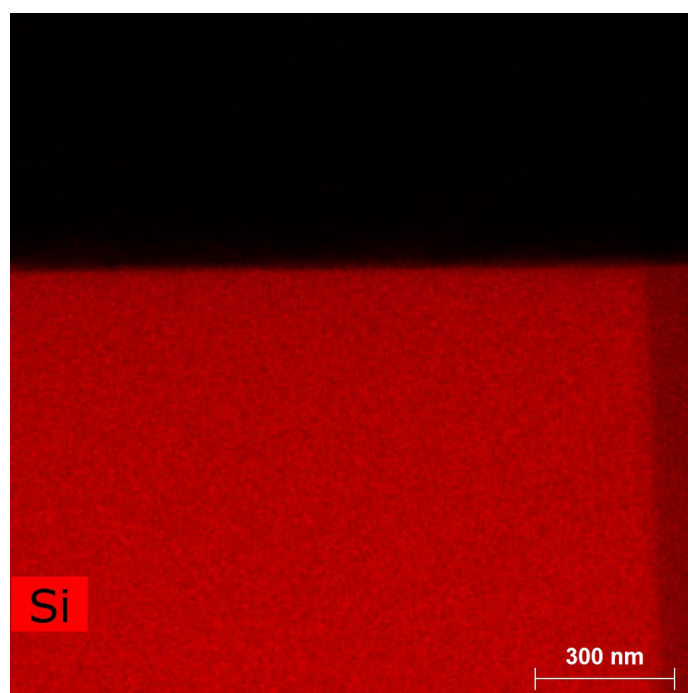
**HAADF image and EDS mapping of post-treated NiSi<sub>x</sub> layer.** HAADF image of post-treated NiSi<sub>x</sub> (Figure A.3.3) shows that the thickness of NiSi<sub>x</sub> layer is ~75 nm, which also reveals a homogeneous coverage on the Si wafer. Additionally, EDS mapping shows that the layer contains a homogeneous composition of Ni (Figure A.3.4) and Si (Figure A.3.5) along with some amounts of carbon (Figure A.3.6) and oxygen (Figure A.3.7).



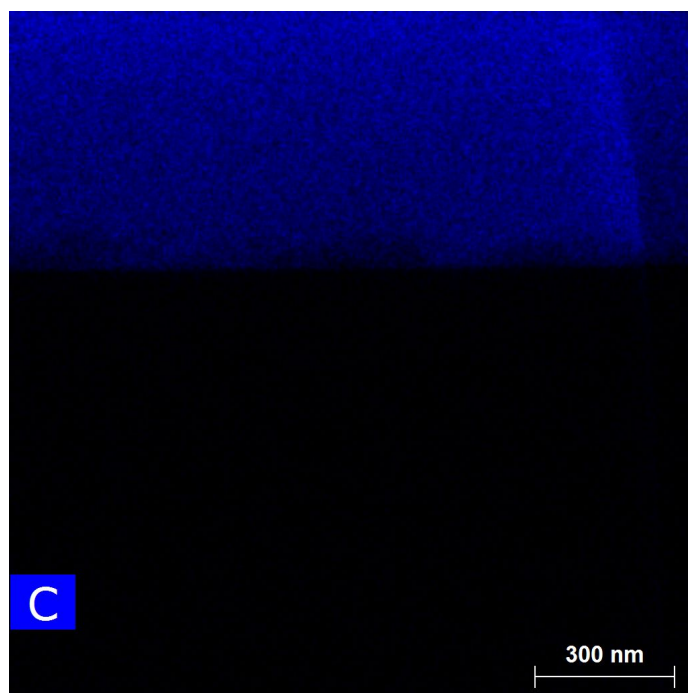
**Figure A.3.3.** HAADF image of the NiSi<sub>x</sub> layer on the Si substrate.



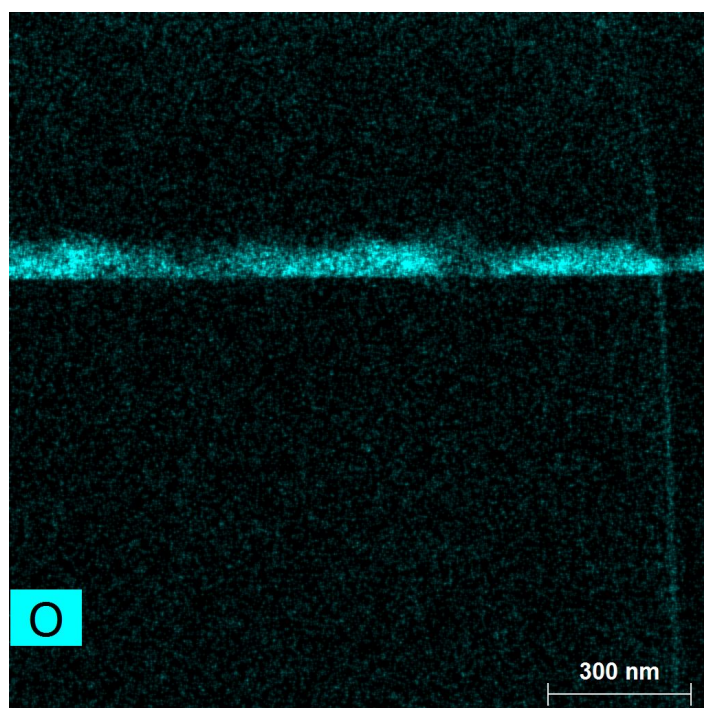
**Figure A.3.4.** EDS mapping image of Ni in the NiSi<sub>x</sub> layer on the Si substrate.



**Figure A.3.5.** EDS mapping image of Si in the NiSi<sub>x</sub> layer on the Si substrate.



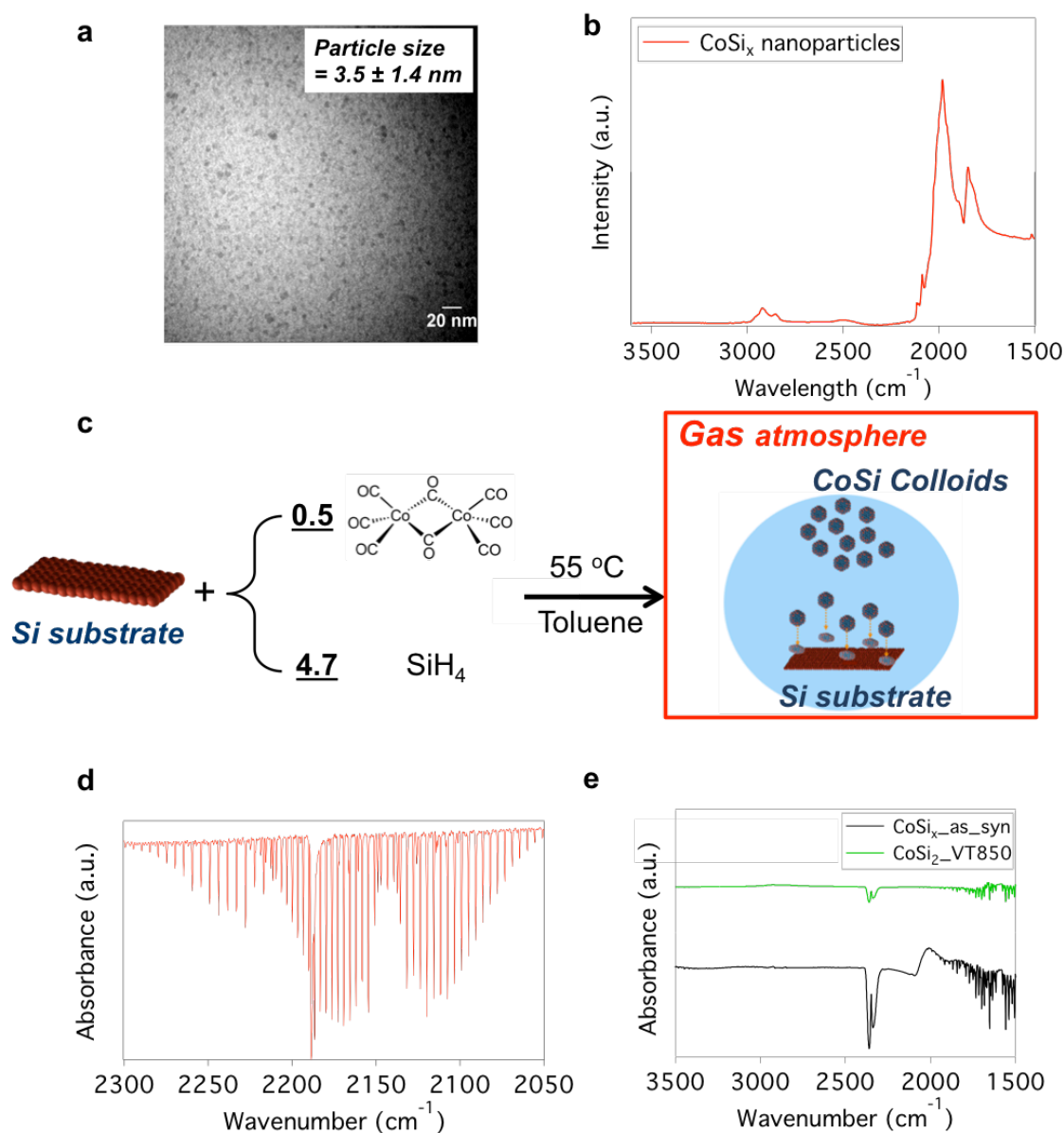
**Figure A.3.6.** EDS mapping image of C in the NiSi<sub>x</sub> layer on the Si substrate.



**Figure A.3.7.** EDS mapping image of O in the NiSi<sub>x</sub> layer on the Si substrate.

#### A.4. Appendix to Chapter 4.

**Fourier Transform infrared spectroscopy (FTIR) results.** After reaction, there is a homogeneous Co-rich layer on the Si (100) wafer (Figure 4.1b) along with 3.5 nm colloids in the remaining solution (Figure A.4.1a). FTIR-ATR (attenuated total reflectance) shows that there are bridging CO at  $1847\text{ cm}^{-1}$  and terminal CO at  $1980\text{ cm}^{-1}$  with the peak at  $2087\text{ cm}^{-1}$  indicating the Si-H vibration on the surface (Figure A.4.1b).<sup>1</sup> It reveals that some CO ligands remained on the surface of the  $\text{CoSi}_x$  colloids after reaction, probably contributing to the small amount of carbon ratio in the deposited layer. FTIR spectroscopy is conducted to monitor the formation of chemical species at the Si-wafer surface and in the gas atmosphere during the  $\text{CoSi}_x$  layer deposition (Figure A.4.1c). FTIR spectra of gas-phase contains vibration-rotation transition signals for each molecular species, inducing characteristic harmonic branches, which are composed of a series of closely separated peaks (Figure A.4.1d).<sup>2</sup> The data reveal the presence of two harmonic bands centered at  $2140\text{ cm}^{-1}$  and  $2180\text{ cm}^{-1}$ , which are assigned to CO decomposition product of  $\text{Co}(\text{CO})_8$  and unreacted  $\text{SiH}_4$ , respectively.<sup>3,4</sup> The remaining of  $\text{SiH}_4$  is owing to the excess amount introduced in the reaction, while a high integrity area of CO bands indicates a large amount of CO released during the reaction. However, there is a certain ratio of CO remained in the as-synthesized layer via FTIR measurement (black curve in Figure A.4.1e). To remove the embedded CO ligands as well as achieving the crystalline  $\text{CoSi}_x$ , thermal treatment at  $850\text{ }^\circ\text{C}$  under vacuum was conducted. From FTIR, the CO signals are eliminated, indicating the CO ligands have been totally removed (green curve in Figure A.4.1e).

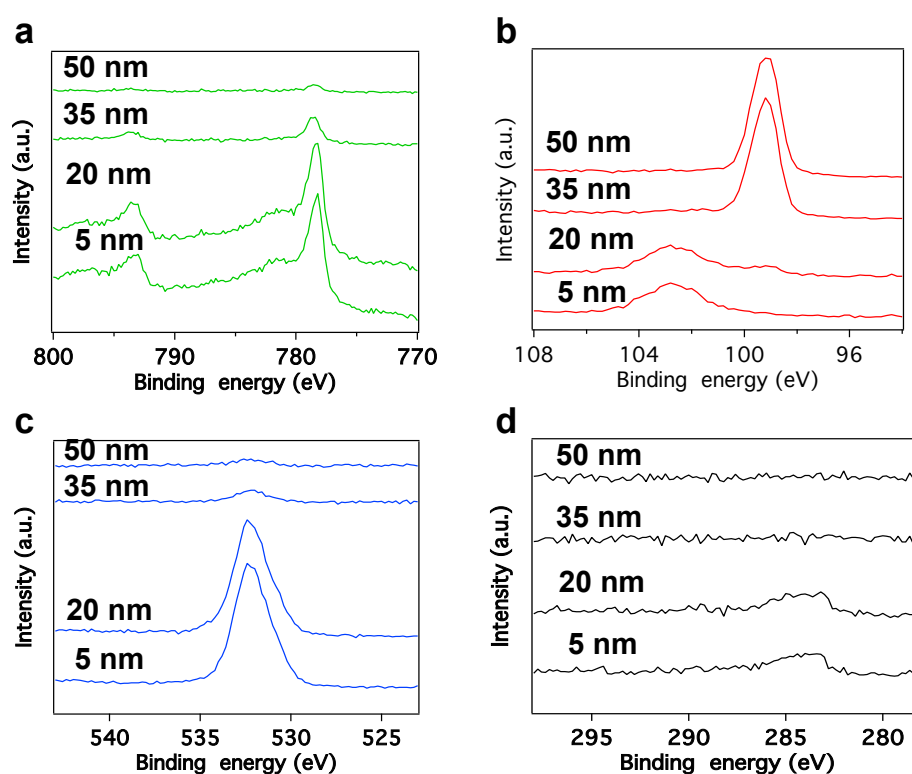


**Figure A.4.1.** (a) TEM image of colloidal nanoparticles formed after chemical one-pot synthesis. (b) FTIR-ATR spectrum of as-synthesized CoSi<sub>x</sub> nanoparticles (c) Scheme of gas-phase after chemical one-pot reaction for FTIR. (d) Gas-phase transmission FTIR for the atmosphere obtained after one-pot synthesis. (e) Transmission FTIR spectrum of the CoSi<sub>x</sub> layer on the as-synthesized wafer (black curve) and the CoSi<sub>2</sub> layer after post-treatment (green curve). Note: the dual peak at 2337 and 2360  $\text{cm}^{-1}$  indicate CO<sub>2</sub>, while the harmonic peak centered at 1596  $\text{cm}^{-1}$  is H<sub>2</sub>O, from which the incident beam went through.<sup>5</sup>

**XPS analysis.** The Co core level was characterized by a binding energy around 778.3 eV (Figure A.4.2a), corresponding to Co with a higher oxidation state. The main peak



for Si 2p at 103 eV (Figure A.4.2b) indicates that Si is also oxidized, that is interpreted by an oxidation of the cobalt silicide sub-layer to cobalt silicate. This happened during the transfer of the specimen to XPS chamber. Between 35 nm and 50 nm, only a peak at 99.2 eV is observed, which is assigned to pure Si(0) (Figure A.4.2b). Co 2p signal is also noticed at this depth (30-50 nm), which reveals a portion of Co has diffused into the substrate. The oxygen peak at 532.4 eV almost disappeared in the bulk Si substrate (Figure A.4.2c, peak at 35 nm and 50 nm), shows that except for surface contamination, there are only low amounts of interstitial oxygen in the Si substrate. The carbon 1s peak shows that there are small amounts of carbon on the surface, while inside the bulk substrate, the carbon peak disappeared, indicating there are no more carbon contamination in the Si substrate.

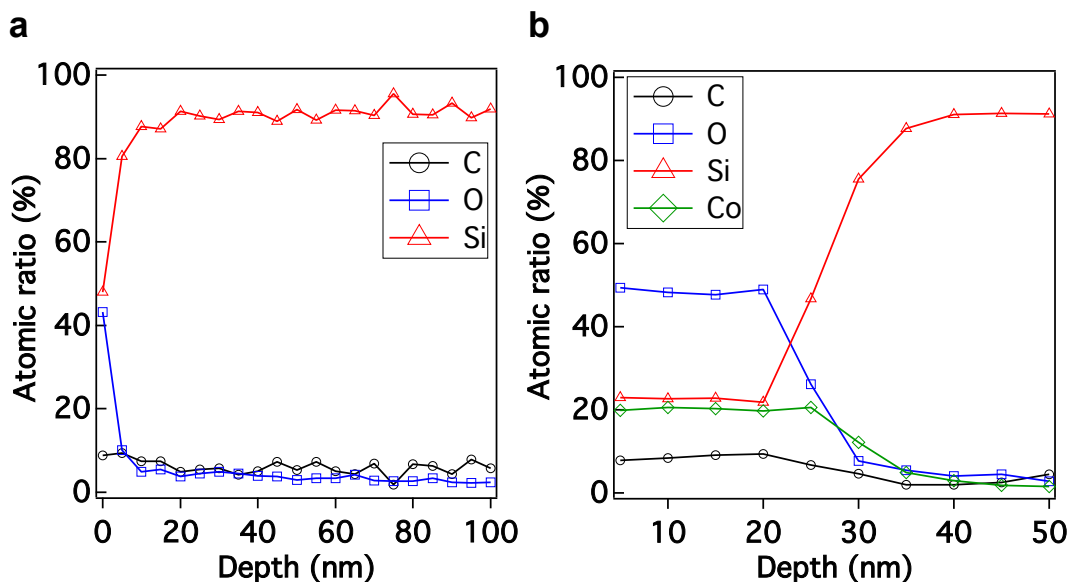


**Figure A.4.2.** XPS spectra of (a) Co 2p<sub>3/2</sub>, (b) Si 2p, (c) O 1s and (d) C 1s at different sputtering depth of 5 nm, 20 nm, 35 nm, and 50 nm.

### Element background analysis by XPS depth profile

Figure A.4.3 and Table A.4.1 compares the XPS depth profiling of a pristine wafer and our wafer after one-pot synthesis. The reference of surface contamination was measured on the pristine wafer, which contains 9% carbon and 43% oxygen (Figure

A.4.3a). Compared to the as-synthesized sample (Figure A.4.3b), the surface carbon and oxygen ratio is 8% and 49%, respectively, which is similar with the amounts found in the reference pristine Si wafer (Table A.4.1). It indicates that the surface contamination on the Si wafer after the chemical reaction mainly comes from the ambient environment.



**Figure A.4.3.** XPS depth profiles of (a) pristine wafer and (b) as-synthesized Co-rich layer on the Si substrate. Note that both substrates underwent the same cleaning procedure, i.e. 40% HF cleaning, drying under high vacuum, and wafers were stored under inert atmosphere.

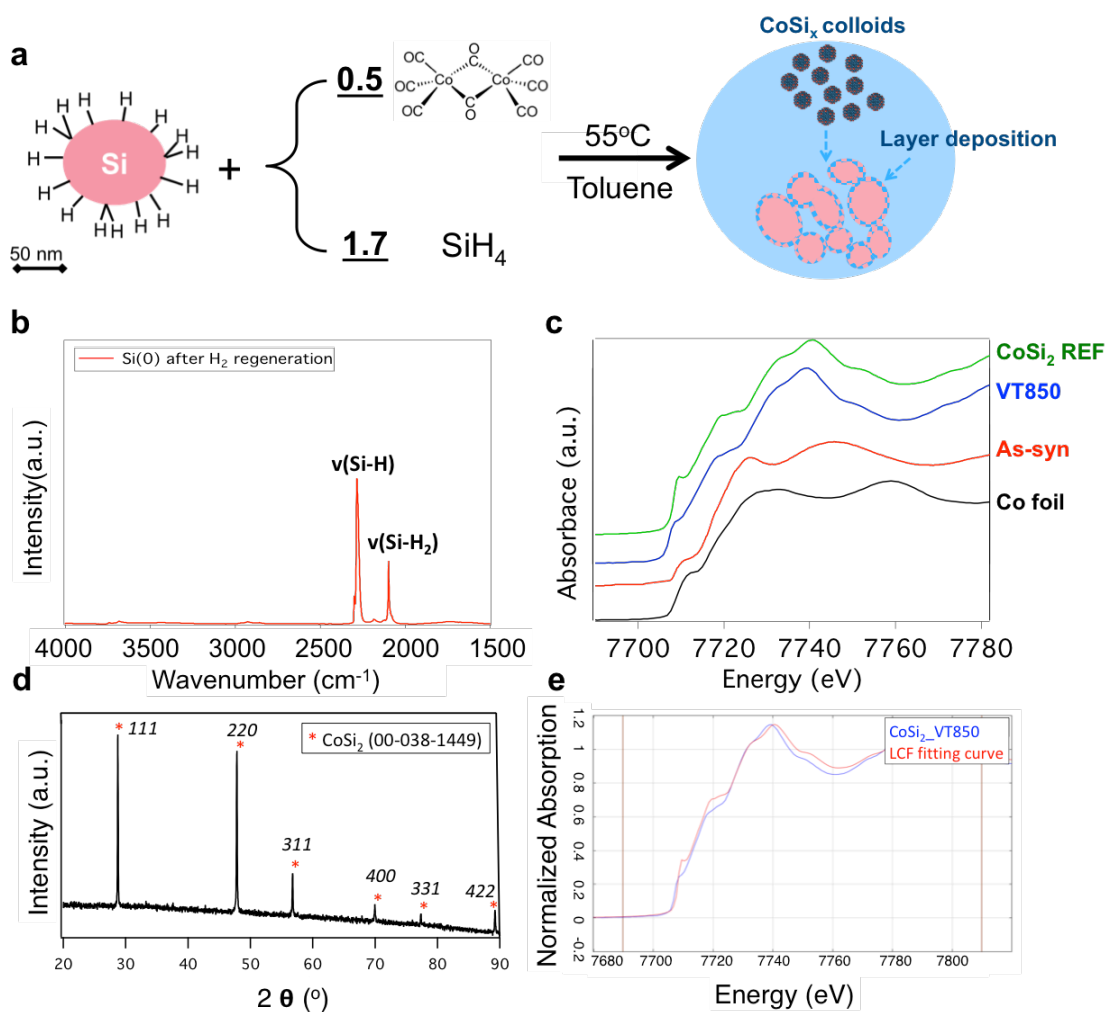
**Table A.4.1.** Quantitative XPS depth profiles of Co-rich layer on the Si substrate with pristine Si wafer as reference.

Sample	Co [%] <sup>c</sup>	Si [%] <sup>c</sup>	C [%] <sup>c</sup>	O [%] <sup>c</sup>
Pristine <sup>a</sup>	0	48	9	43
As-syn <sup>b</sup>	20	23	8	49

<sup>a</sup>)Pristine Si substrate, the surface atomic ratio was counted in the surface point; <sup>b</sup>)as-synthesized sample, the atomic ratio was averaged in the first 20 nm; <sup>c</sup>)Atomic %.

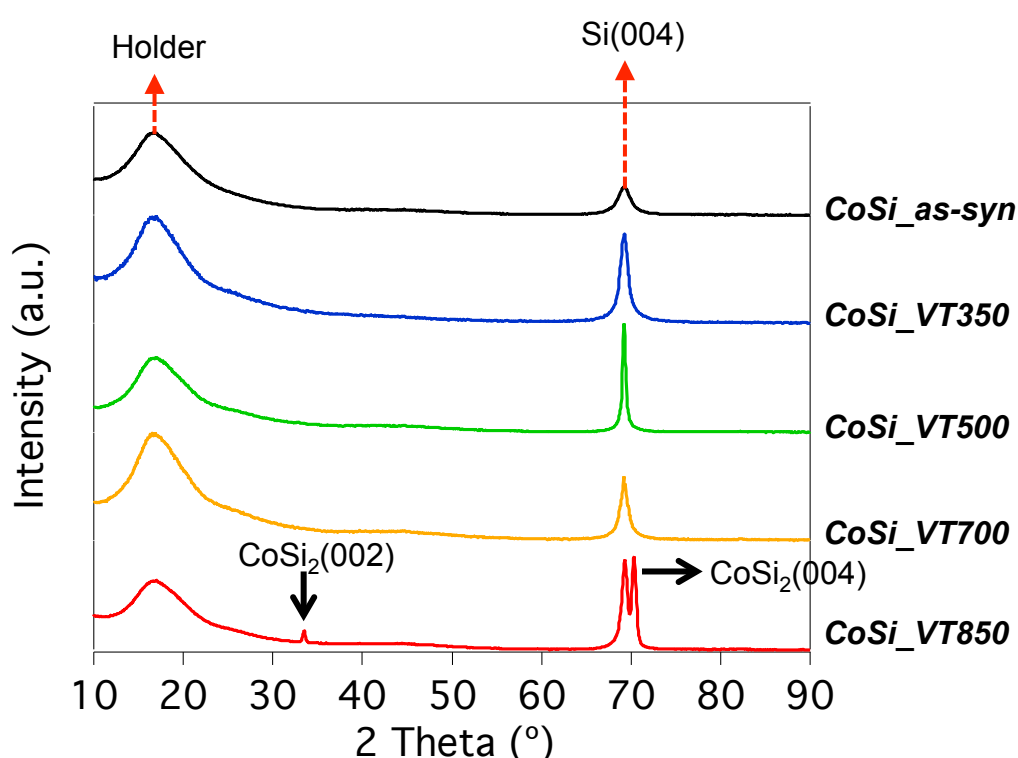
**Characterization of CoSi<sub>x</sub> layer using Si nanoparticles as a model.** One-pot synthesis was used on the support of Si(0) nanoparticles, which were previously treated at 900 °C under H<sub>2</sub> to form a pristine terminated Si-H surface, similarly to the surface of wafers (Figure A.4.4a). Note that the Co loading was lower than the one for wafer: 350 Co.nm<sup>-2</sup> instead of 110'000 Co.nm<sup>-2</sup> due to the higher surface area of Si(0) nanoparticles.

The CoSi<sub>x</sub> layer structure was investigated at the different stage of the sample preparation using X-ray absorption spectroscopy (XAS) at the Co K-edge under pristine condition. There are significantly different configurations between the spectrum of as-synthesized Co-rich layer on Si(0) nanopowder (red curve, Figure A.4.4c) and Co(0) foil reference (black curve, Figure A.4.4c), associated with the charge redistribution for the CoSi<sub>x</sub> formation.<sup>6</sup> For the samples after post-treatment at 850 °C (blue curve, Figure A.4.4c), the observed edge at 7707 eV revealed the formation of CoSi<sub>2</sub>.<sup>7</sup> Also, linear combination fitting was conducted on the sample after post-treatment at 850 °C and compared with the reference samples of CoSi<sub>2</sub> and Co(0) foil, which shows the presence of ca. 99.2% CoSi<sub>2</sub> and 0.8% Co(0). The XRD of CoSi<sub>2</sub> reference material and the linear combination fitting curve are provided as Figure A.4.4d and Figure A.4.4e, respectively.



**Figure A.4.4.** (a) Reaction scheme of the one-pot synthesis on a Si(0) nanoparticles. ( $\text{Co}_2(\text{CO})_8$  350 Co/ $\text{nm}^2$ ,  $\text{SiH}_4/\text{Co}=1.7$ , toluene,  $55^\circ\text{C}$ ). (b) Transmission FTIR analysis of Si(0) nanopowder after  $\text{H}_2$  regeneration (red line). (c) X-ray absorption spectra of samples of as-synthesized  $\text{CoSi}_x$  on Si(0) nanopowder (red curve),  $\text{CoSi}_x$  after thermal treatment at  $850^\circ\text{C}$  under vacuum for 12 h (blue curve), commercial  $\text{CoSi}_2$  powder (green curve) and Co (0) foil as the reference (black curve). (d) XRD of the  $\text{CoSi}_2$  reference material. (e) Linear combination fitting curve of  $\text{CoSi}_2$ \_VT850.

**Crystallinity investigation via XRD using different treated temperature.** XRD data (Figure A.4.5) show that there is no presence of crystalline  $\text{CoSi}_x$  in the as-synthesized layer. It means that after the chemical reaction, the film is composed of amorphous  $\text{CoSi}_x$  nanoparticles. Despite increasing the temperature from to 350 °C, 500 °C, to 700°C, it still shows no crystalline signals, which indicates that there is always an amorphous film after the thermal vacuum treatment until 700°C. However, once after the vacuum treatment at 850 °C,  $\text{CoSi}_2$  crystalline signals appeared in the film with {100} out-of-plane orientation. This single orientation is resulted from the excellent epitaxial growth of  $\text{CoSi}_2$  on Si (100) substrate.



**Figure A.4.5.** X-ray diffraction of  $\text{CoSi}_x$  on Si(100) substrate: As-synthesized sample (black curve) and samples after 350 °C (blue curve), 500 °C (green curve), 700 °C (yellow curve), and 850 °C (red curve) thermal vacuum treatment.

**Calculation method of the thermionic emission equation.** The thermionic emission model is used to fit the I-V curve of the as-synthesized sample (Figure 4.2d).

$$I_a = AA_0 T^2 e^{-\frac{\Phi_n}{k_B T}} \left[ e^{-\frac{e_0(V-R_s I_a)}{\eta k_B T}} - 1 \right], \quad (\text{A.4.1})$$

$I_a$  : applied current (A)

$V$  : measured voltage (V)

$A$  : active area ( $7.8 \times 10^{-7} \text{ m}^2$ )

$A_0$  : effective Richardson constant ( $1.20 \times 10^6 \text{ A.m}^{-2}\text{K}^{-2}$ )

$T$  : temperature of the measurement (298K)

$k_B$  : the Boltzmann constant ( $8.62 \times 10^{-5} \text{ eV/K}$ )

$\Phi_n$  : Schottky barrier height (eV)

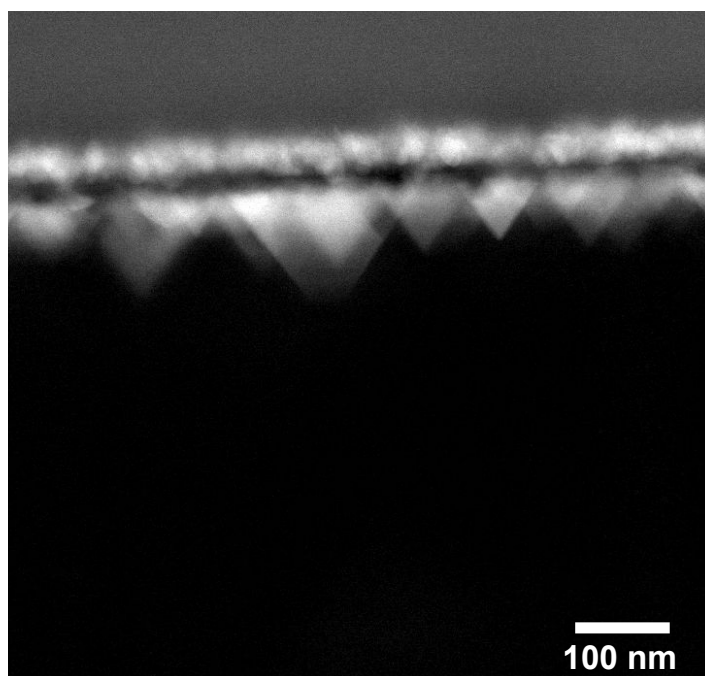
$\eta$  : the ideality factor

$R_s$  : the series resistance ( $\Omega$ )

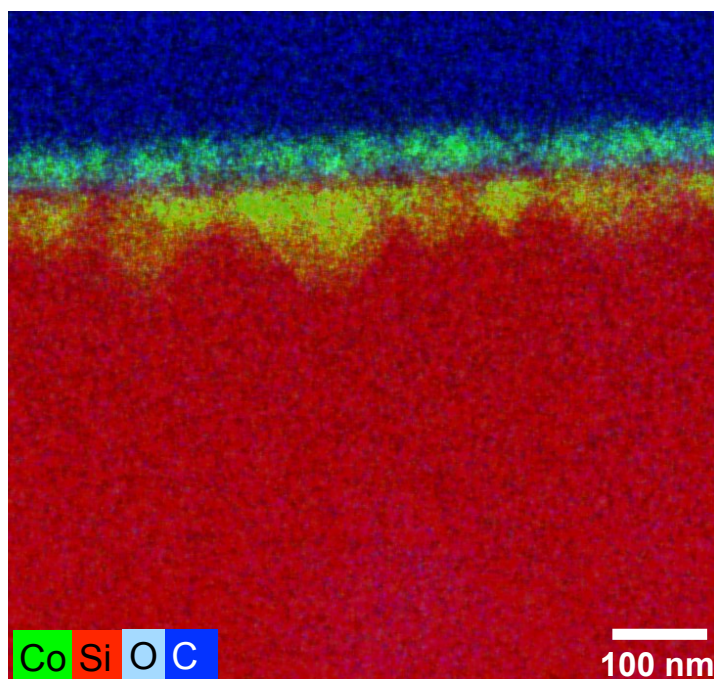
Fitting the positive part of the  $I_a$  and  $V$  curve, the nonlinear least-squares method was used on the thermionic emission equation (Eq. A.4.1), providing  $\Phi_n$ ,  $\eta$ , and  $R_s$ .

The fitted Schottky barrier height and the series resistance are 0.54 eV and 147  $\Omega$ , respectively, with the ideality factor of 115.

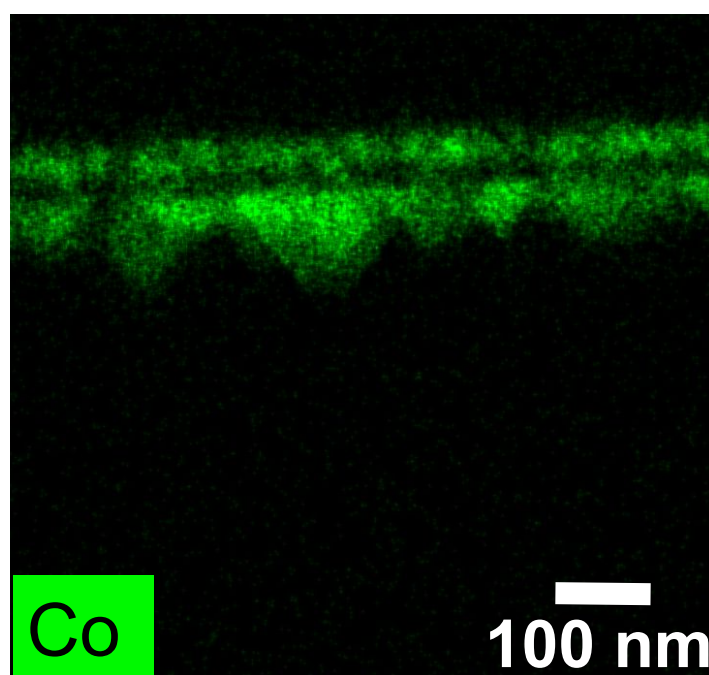
**EDS mapping of post-treated CoSi<sub>2</sub> layer.** EDS mapping of post-treated CoSi<sub>2</sub> (Figure A.4.6) shows that the thickness of CoSi<sub>2</sub> layer is ~30 nm, which also reveals a homogeneous coverage on the Si wafer. Additionally, pyramid-shape of Co-based material is formed below the interface of CoSi<sub>2</sub> and Si substrate (Figure A.4.6-A.4.7). They are resulted from the diffusion of Co into Si substrate along Si(111) surface (Figure A.4.8-A.4.9), which exhibits the lowest the energy among the Si crystalline surfaces. Also, there are still oxygen (Figure A.4.10) and carbon (Figure A.4.11) embedded in this layer, which mainly come from the ex-situ transfer before the TEM measurement. Moreover, to disclose the Co diffusion behavior between the interface of CoSi<sub>2</sub> and Si substrate, TEM on the specific area has further confirmed that the Co diffuses along with the Si (111) direction (Figure A.4.12).



**Figure A.4.6.** HAADF image of the CoSi<sub>2</sub> layer on the Si substrate.

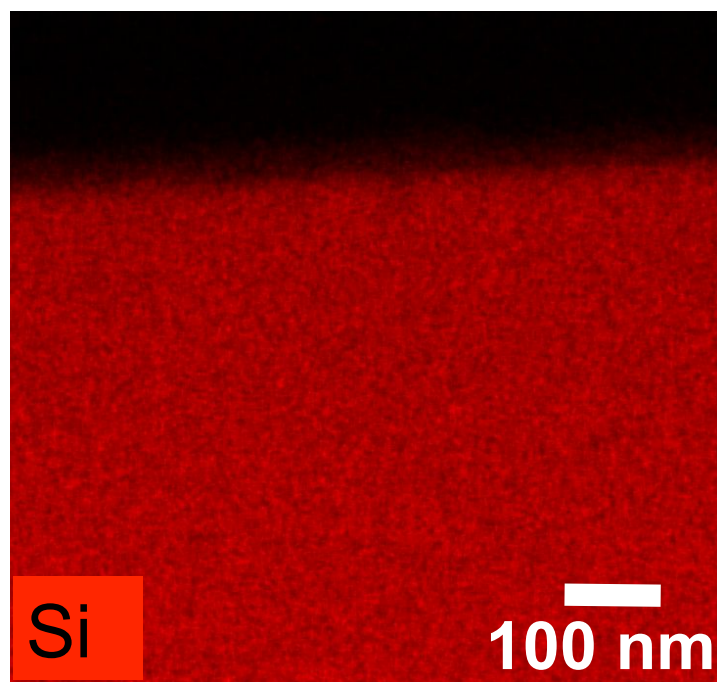


**Figure A.4.7.** EDS mapping image of the CoSi<sub>2</sub> layer on the Si substrate.

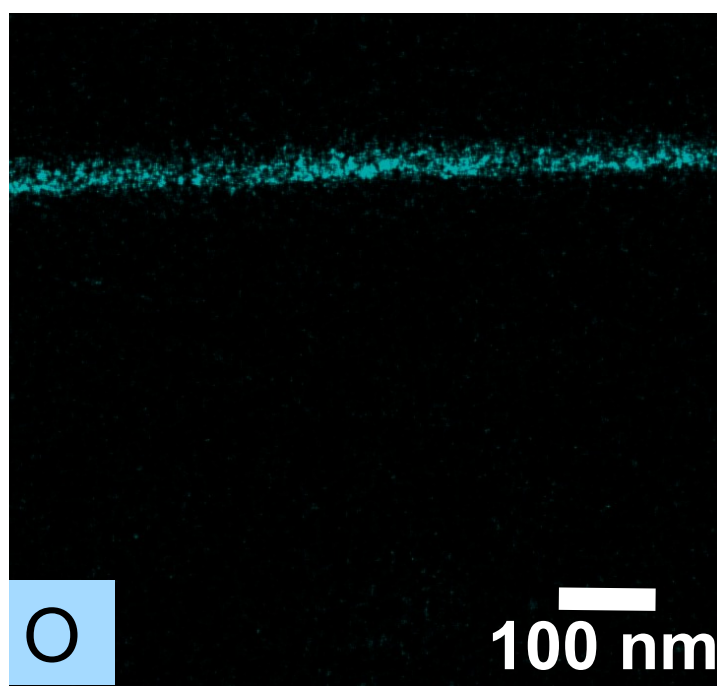


**Figure A.4.8.** EDS mapping image of Co element in the CoSi<sub>2</sub> layer on the Si substrate.

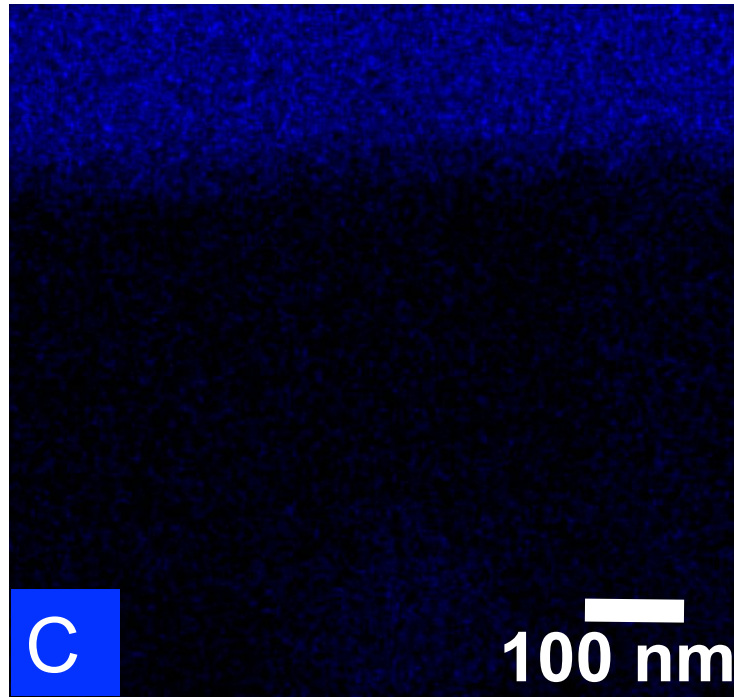




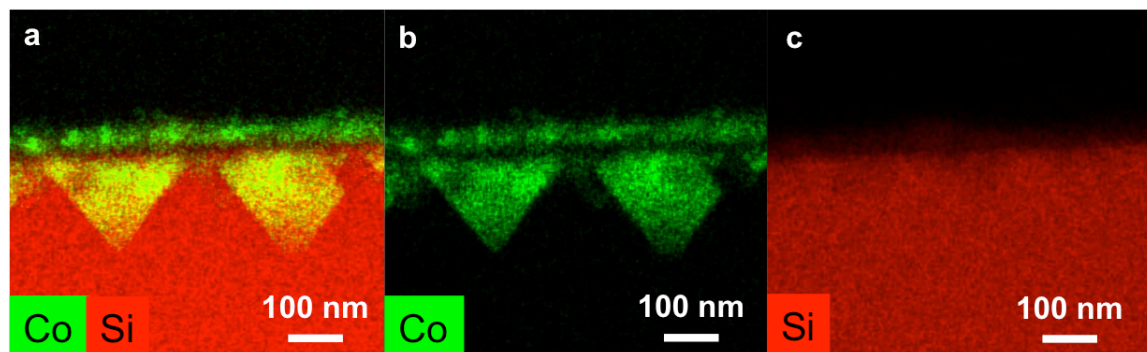
**Figure A.4.9.** EDS mapping image of Si element in the  $\text{CoSi}_2$  layer on the Si substrate.



**Figure A.4.10.** EDS mapping image of O element in the  $\text{CoSi}_2$  layer on the Si substrate.

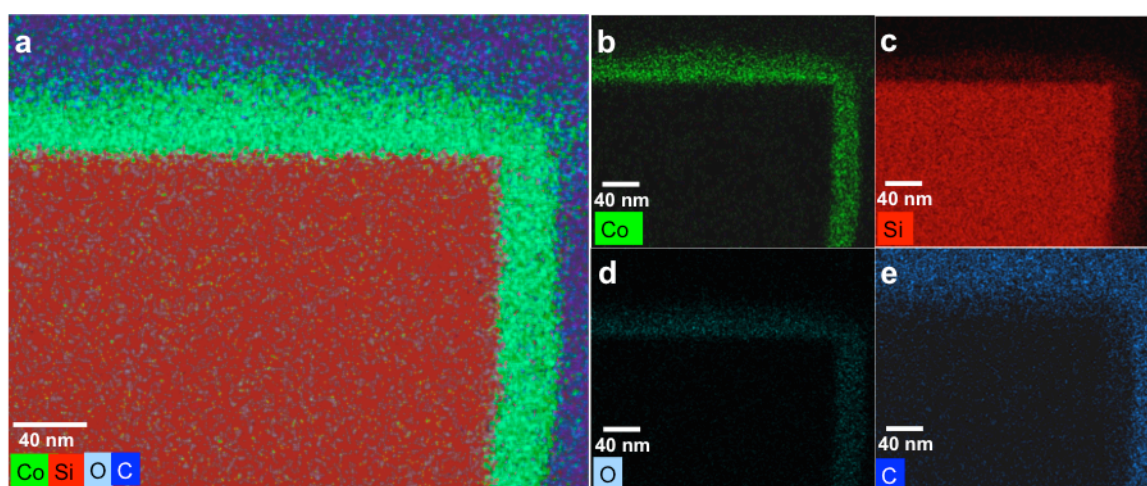


**Figure A.4.11.** EDS mapping image of C element in the CoSi<sub>2</sub> layer on the Si substrate.

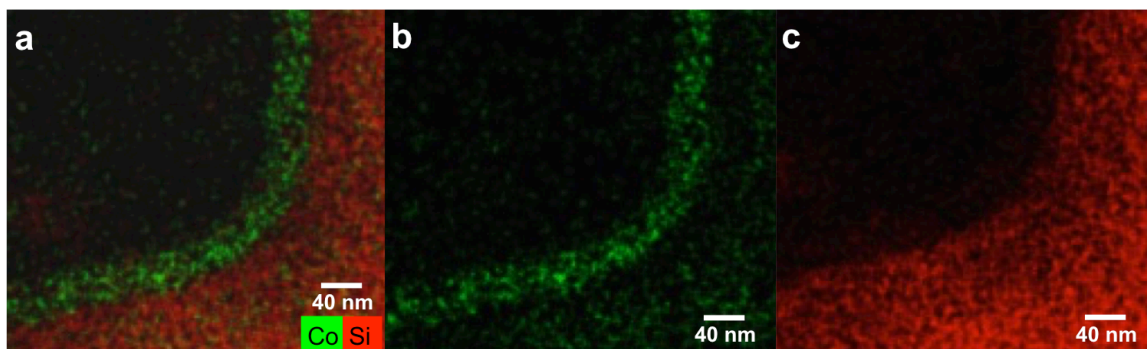


**Figure A.4.12.** (a) EDS mapping image of the CoSi<sub>2</sub> layer on the Si substrate. (b-c) Co and Si EDS mapping images of the CoSi<sub>2</sub> layer on the Si substrate, respectively. The wafer was exposed to air prior to analysis.

**Conformal deposition on trenched Si substrate.** EDS mapping of as-synthesized  $\text{CoSi}_x$  on the trench-structured wafer (Figure A.4.13) shows that the thickness of  $\text{CoSi}_x$  layer deposited on the top is 37.8 nm and the thickness on the edge is 38.4 nm. It reveals that this chemical method provides an excellent capability of conformal deposition, shown by the consistent thickness between the edge part and the top part. This provides the value of step coverage equals to 1.01. As described before and in the main text, the contamination of oxygen (Figure A.4.13d) comes from the ex-situ transfer to TEM. Also, for the bottom part, TEM-EDS mapping (Figure A.4.14) results showed that the thickness on the bottom and edge is  $\sim 36.9$  nm, revealing a step coverage is  $\sim 1$ , which is consistent with the upper part of the trench.



**Figure A.4.13.** (a) EDS mapping image of the Co-rich layer on the trenched-Si substrate. (b-e) Co, Si, O, and C EDS mapping images of the Co-rich layer on the Si substrate, respectively. The wafer was exposed to air prior to analysis.



**Figure A.4.14.** (a) EDS mapping image of the Co-rich layer on the trenched-Si substrate. (b) Co and (c) Si EDS mapping images of the Co-rich layer on the Si substrate, respectively. The wafer was exposed to air prior to analysis.

## References

1. Buriak, J. M., Organometallic Chemistry on Silicon and Germanium Surfaces. *Chem. Rev.* **2002**, *102*, 1271-1308.
2. Atkins, P.; Paula, J. D. *Atkins' Physical Chemistry*; Macmillan Higher Education: 2006.
3. Kolomiitsova, T. D.; Savvateev, K. F.; Shchepkin, D. N.; Tokhadze, I. K.; Tokhadze, K. G., Infrared Spectra and Structures of SiH<sub>4</sub> and GeH<sub>4</sub> Dimers in Low-Temperature Nitrogen Matrixes. *J. Phys. Chem. A* **2015**, *119*, 2553-2561.
4. London, J. W.; Bell, A. T., Infrared spectra of carbon monoxide, carbon dioxide, nitric oxide, nitrogen dioxide, nitrous oxide, and nitrogen adsorbed on copper oxide. *J. Catal.* **1973**, *31*, 32-40.
5. Kauffman, K. L.; Culp, J. T.; Goodman, A.; Matranga, C., FT-IR Study of CO<sub>2</sub> Adsorption in a Dynamic Copper(II) Benzoate–Pyrazine Host with CO<sub>2</sub>–CO<sub>2</sub> Interactions in the Adsorbed State. *J. Phys. Chem. C* **2011**, *115*, 1857-1866.
6. Naftel, S. J.; Coulthard, I.; Sham, T. K.; Das, S. R.; Xu, D. X., Structural and electronic property evolution of nickel and nickel silicide thin films on Si(100) from multicore x-ray-absorption fine-structure studies. *Phys. Rev. B* **1998**, *57*, 9179-9185.
7. Lerch, P.; Jarlborg, T.; Codazzi, V.; Loupiaz, G.; Flank, A. M., X-ray-absorption spectroscopy in CoSi<sub>2</sub> and NiSi<sub>2</sub>: Experiment and theory. *Phys. Rev. B* **1992**, *45*, 11481-11490.

## A.5. Appendix to Chapter 5.

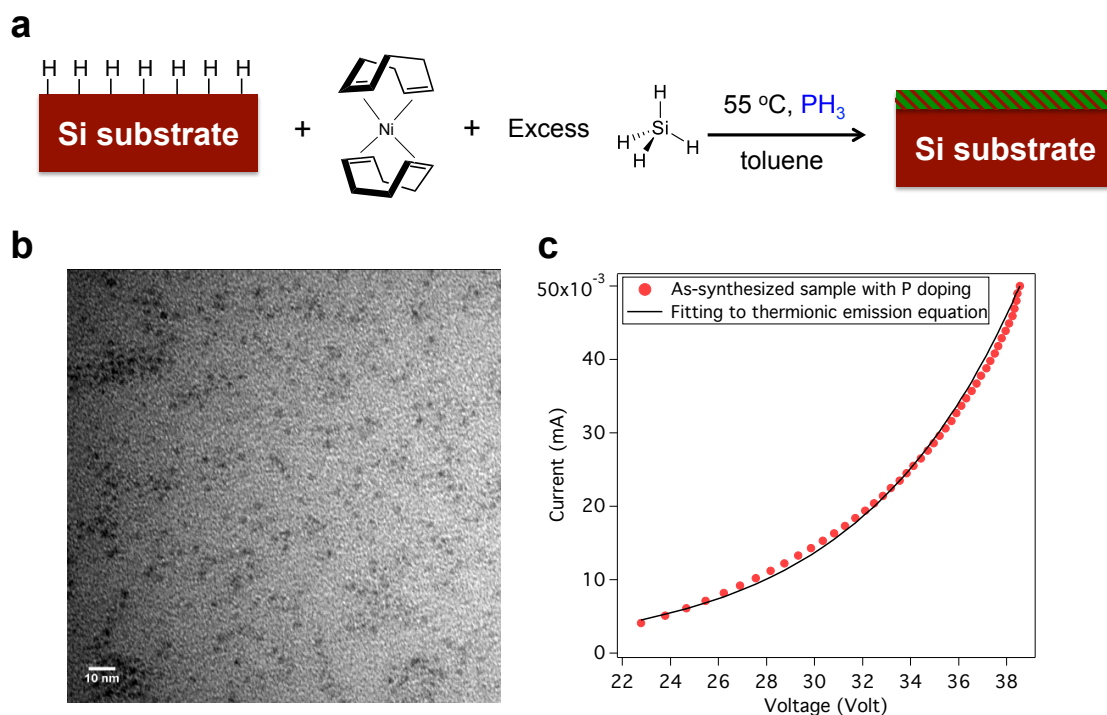
### **Preparation of P-doped nickel silicide layer on Si wafer (One-pot synthesis).**

Double-side polished p-type 4" Si wafers with (100) orientations were diced into 2 cm  $\times$  1 cm dies and cleaned by 40% HF solution for 60 s. The diced wafers were then dried under high vacuum ( $\sim 10^{-5}$  mbar) at room temperature for 12 h.

A HF-treated diced Si-wafer and 20 mg  $\text{Ni(COD)}_2$  (0.07 mmol) were placed in a 325 mL Fischer-Porter bottle in a glovebox and dissolved in toluene (10 mL). The reactor was then pressurized under 2.7 bars of 1%  $\text{SiH}_4$  in He (0.33 mmol). Then, the reactor was filled with 2.7 bars of 1%  $\text{SiH}_4$  (0.33 mmol) and 0.01 mmol  $\text{PH}_3$  at room temperature and the reaction mixture was heated to 55 °C for 16 h, during which a layer was formed on top of the Si-wafer accompanied by the formation of a dark solution (colloids formation). The colloidal solution was transferred out from the reactor via a cannula and the Si-wafer was washed twice with 10 mL of toluene. Prior storage inside glovebox, the as-synthesized wafer was dried under vacuum ( $\sim 10^{-2}$  mbar) for 3 h.

The reaction scheme is shown in Figure A.5.1a, and the TEM image (Figure A.5.1b) shows that the size of the particles is around 2.3 nm. The I-V curve of the as-synthesized wafer (Figure A.5.1c) was measured by the 4-point-probe measurement, which reveals that the fitted Schottky barrier height and the series resistance are 0.5 eV and 1.0  $\Omega$ , respectively.





**Figure A.5.1.** (a) Reaction scheme for one-pot synthesis, and the condition is as below:  $\text{Ni(COD)}_2/\text{die}$ ,  $110000 \text{ Ni.nm}^{-2}$ ,  $\text{SiH}_4/\text{Ni}=4.7$  with  $0.01 \text{ mmol PH}_3$ , toluene,  $55^\circ\text{C}$  for 16 h. (b) TEM image of colloidal nanoparticles formed after the chemical one-pot synthesis. (c) I-V characteristics of P-doped  $\text{NiSi}_x$  layer on the Si(100) wafer fitting to thermionic emission equation.

## **Appendix B: Investigation of Phosphorus Grafting Capability on Silica with Different Surface Environments via $^{31}\text{P}$ NMR**

Individual contributions:

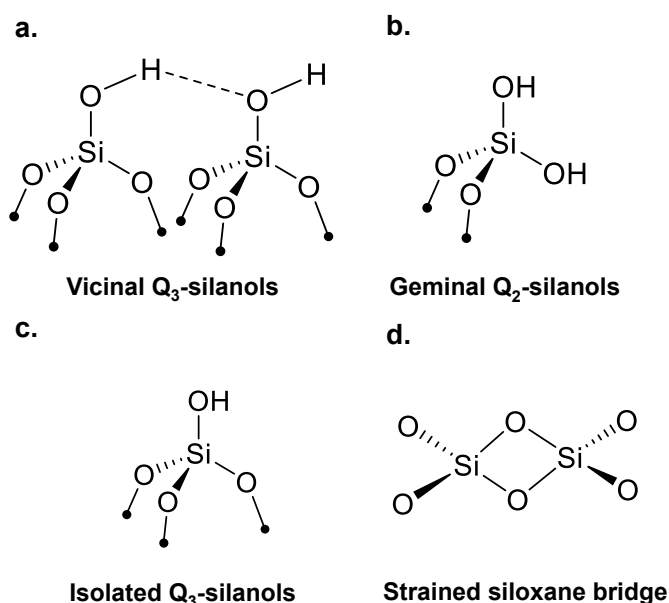
T-H. Lin, W-C. Liao, K. Searles and C. Copéret designed all experiments. T-H. Lin developed and characterized all materials. T-H. Lin prepared samples and conducted NMR analysis with W-C. Liao. All authors contribute to the scientific discussions.

### ***B.1. Introduction***

The preparation of advanced nanoscale fabrications (photocatalysts<sup>1, 2</sup>, semiconductors<sup>3-5</sup>, etc.) necessitates molecular level control and precision for continued developments. Thus, a controlled method and understanding for selective surface incorporation is essential. Surface Organometallic Chemistry (SOMC) has emerged as a powerful route for the development of well-defined heterogeneous materials through stringent control of surface functionalities, typically surface –OH groups of oxide materials.<sup>6-12</sup> This allows for the incorporation of well-defined molecular precursors with nanoscale precision and has found applications.

Among several oxide materials, amorphous silica has been extensively utilized as a support for the preparation of well-defined heterogeneous materials using SOMC due to the ability to control the density and identity of surface silanols. It is well-established that the silica surface presents mainly three types of silanols: vicinal Q<sub>3</sub>-, geminal Q<sub>2</sub>-, and isolated Q<sub>3</sub>-silanols (Figure B.1).<sup>13</sup> The density and ratio of silanol groups changes upon increasing the temperature of dehydroxylation; at >700 °C mostly isolated Q<sub>3</sub>-silanols are present. In general, these surface silanols are used as grafting sites. However, the dehydroxylation process also generates siloxane bridges, which become more strained at higher temperatures and can yield highly reactive 4-membered siloxane bridges when prepared at sufficiently high temperatures.<sup>14, 15</sup> Overall, the density of these 4-membered siloxane bridges is far less than the isolated Q<sub>3</sub>-silanols (0.15/nm<sup>2</sup>).<sup>14</sup> Grafting of organometallic complexes directly on these strained-sites has been shown to take place when either highly reactive organometallics and/or highly dehydroxylated surfaces are used.





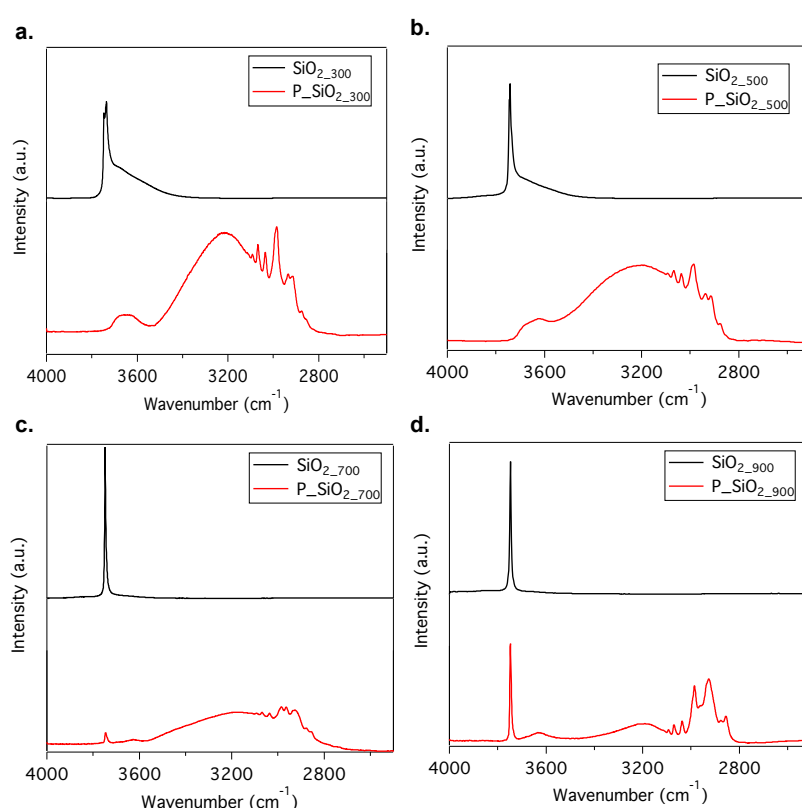
**Figure B.1.** Different types of silica surface structures.

Since phosphonate precursors are often used as alternative anchoring group for a broad range of organic ligands,<sup>17</sup> we have investigated in greater details the reactivity of diethyl benzylphosphonate – OP(OEt)<sub>2</sub>(CH<sub>2</sub>Ph) (DEBP) – towards silica surfaces in a broad range of temperature treatment (300-900 °C). We show in particular that such phosphonate has minimal reactivity towards surface silanols (if any) and hardly grafts on silica partially dehydroxylated at low temperatures, while grafting readily takes place on silica partially dehydroxylated at high temperatures according to detailed phosphorus-31 solid-state NMR spectroscopy. These observations indicate that phosphonate selectively graft on reactive – strained – siloxane bridge that are formed upon dehydroxylation.

## B.2. Results and discussion

Grafting of the phosphonate precursor O=P(OC<sub>2</sub>H<sub>5</sub>)<sub>2</sub>(CH<sub>2</sub>Ph) (1 equiv. to surface SiOH) is carried out in pentane at room temperature for 16h with silica partially dehydroxylated at different temperatures, yielding P\_SiO<sub>2\_X</sub> (X = 300, 500, 700 and 900 °C). After subsequent washings with pentane (3 x 6 mL) and drying under high vacuum (10<sup>-5</sup> mbar) for 3 h, the infrared (IR) spectra of all materials, P\_SiO<sub>2\_X</sub> (X = 300, 500, 700, 900 °C), are recorded (Figure B.2). P\_SiO<sub>2\_300/500</sub> (red trace in Figure B.2a-b) shows two broad features ranging from 2800 cm<sup>-1</sup> to 3550 cm<sup>-1</sup> and from 3550 cm<sup>-1</sup> to 3750 cm<sup>-1</sup> associated with H-bonded hydroxyl species, and some sharp features between 3091 and 2857 cm<sup>-1</sup> associated with C–H bond stretching. The IR

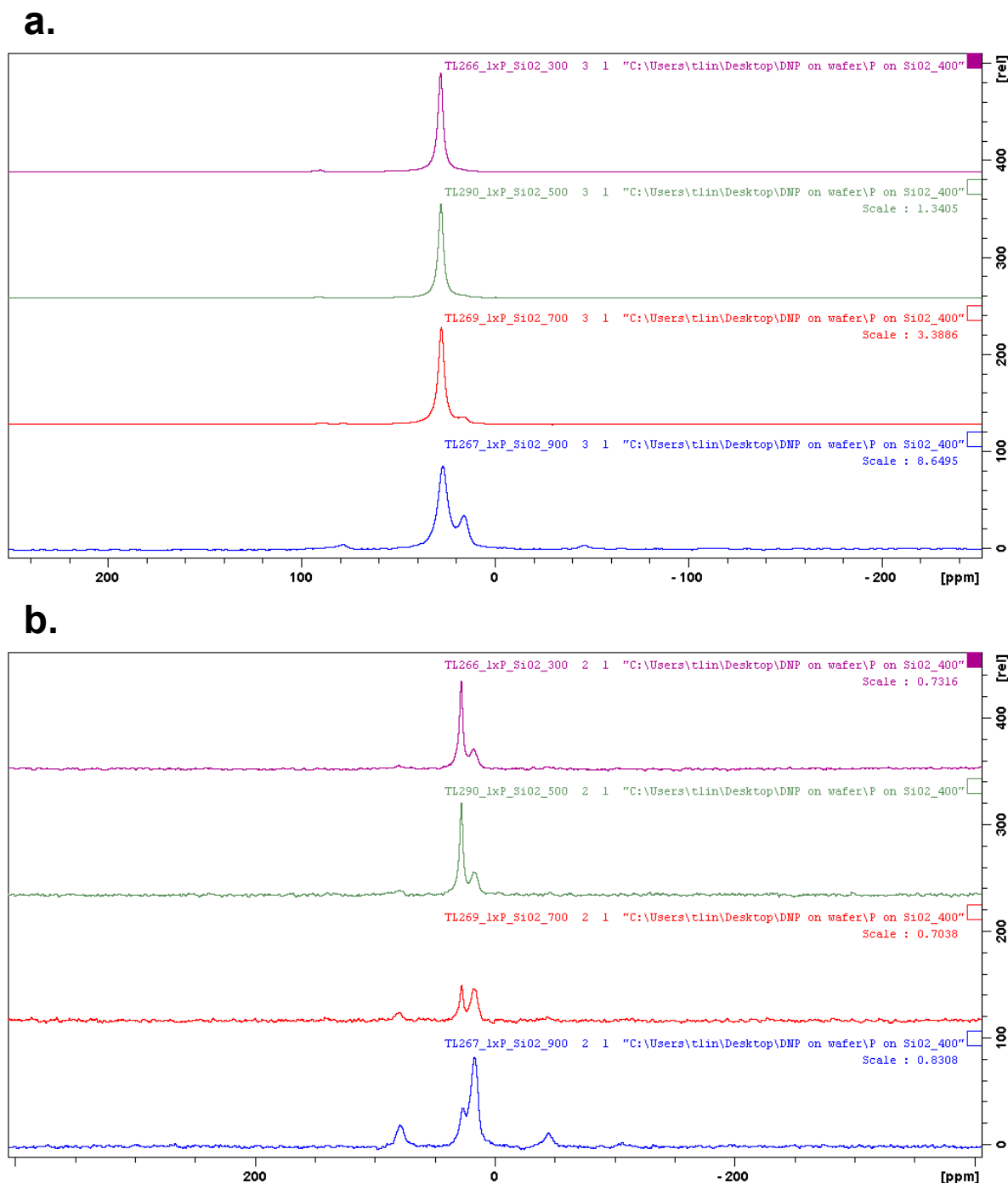
spectra of P\_SiO<sub>2</sub>\_700 (red traces in Figure B.2c) show similar features, but the broad features centred at ca. 3200 cm<sup>-1</sup> are less intense. The spectrum also shows the peak at 3745 cm<sup>-1</sup>, associated with the remaining isolated silanol groups on the surface. The IR spectrum of P\_SiO<sub>2</sub>\_900 (red traces in Figure B.2d) is noteworthy as it displays bands at 3745 cm<sup>-1</sup> (sharp and intense – isolated OH group), 3600 cm<sup>-1</sup> (broad and small – OH interacting with aromatic rings), 3200 cm<sup>-1</sup> (broad and medium – interacting OH group presumably with P=O) associated presumably with specific types of OH groups along with a series of sharper bands at lower wave number associated with the ethyl and benzyl group as found in the molecular precursor.



**Figure B.2.** FT-IR of 1 equiv. of diethylbenzylphosphonate on silica dehydroxylated at 300 (P\_SiO<sub>2</sub>\_300), 500 (P\_SiO<sub>2</sub>\_500), 700 (P\_SiO<sub>2</sub>\_700), and 900 °C (P\_SiO<sub>2</sub>\_900).

Each material is also analysed by direct-excitation <sup>31</sup>P solid-state NMR (SSNMR) (Figure B.3a). While the <sup>31</sup>P SSNMR spectrum of P\_SiO<sub>2</sub>\_300/500 (violet/green trace in Figure B.3a) indicates the presence of one major surface species. P\_SiO<sub>2</sub>\_700/900 (red/blue traces in Figure B.3a) display two peaks at 28 ppm and 17 ppm, associated with two different <sup>31</sup>P surface species, for which the more downfield peak at ~28 ppm is also present in P\_SiO<sub>2</sub>\_300/500. Based on the chemical shift anisotropy (CSA)

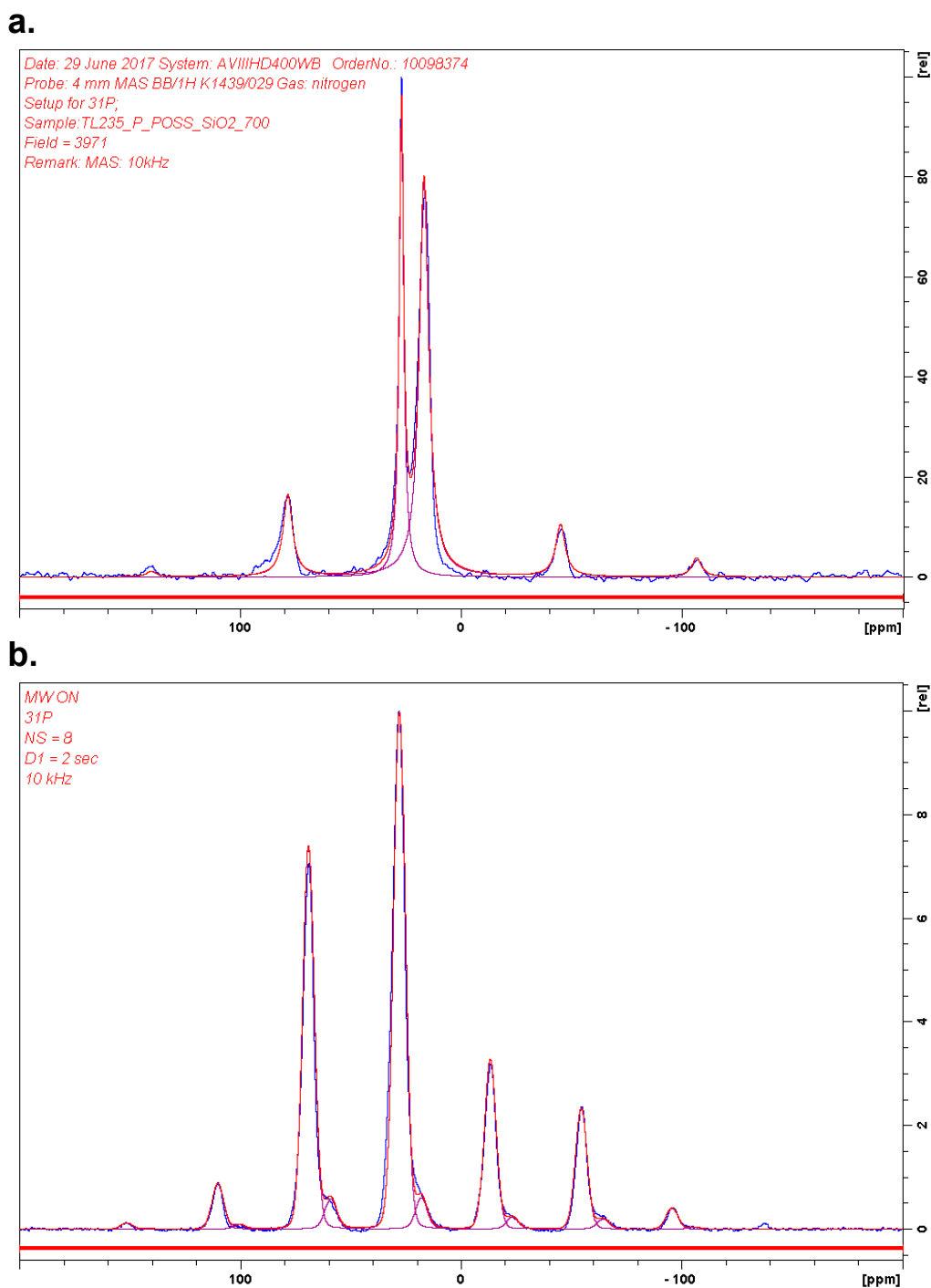
analysis of the downfield peak, the span ( $\Omega$ ) is 0 and 14 for P\_SiO<sub>2</sub>\_700 and P\_SiO<sub>2</sub>\_900, respectively. In contrast, the upfield peak at ~17 ppm has a significantly larger span, which is 151 and 160 for P\_SiO<sub>2</sub>\_700 and P\_SiO<sub>2</sub>\_900, respectively (Table B.S1), suggesting a more rigid structure with less dynamics. This analysis is further supported by the comparison between direct-excitation and cross-polarization magic-angle spinning (CP-MAS) solid-state NMR spectrum (Figure B.3b), where the peak at ~17 ppm is now significantly more intense than this at ~28 ppm as a result of a more efficient CP transfer, consistent with a less mobile species. Note that the signal appearing at ~17 ppm associated with a larger anisotropy is also found in P\_SiO<sub>2</sub>\_300/500, albeit with a very small intensity (vide infra).



**Figure B.3.**  $^{31}\text{P}$  solid-state NMR (a) direct-excitation spectra of 1 equiv. of diethylbenzylphosphonate on silica dehydroxylated at 300 ( $\text{P\_SiO}_2_{300}$ ), 500 ( $\text{P\_SiO}_2_{500}$ ), 700 ( $\text{P\_SiO}_2_{700}$ ), and 900  $^{\circ}\text{C}$  ( $\text{P\_SiO}_2_{900}$ ). (b) CP-MAS spectra of 1 equiv. of diethylbenzylphosphonate on silica dehydroxylated at 300 ( $\text{P\_SiO}_2_{300}$ ), 500 ( $\text{P\_SiO}_2_{500}$ ), 700 ( $\text{P\_SiO}_2_{700}$ ), and 900  $^{\circ}\text{C}$  ( $\text{P\_SiO}_2_{900}$ ).

To further confirm the difference of dynamic between these two species and to easily obtain the CSA parameter, the NMR spectrum of  $\text{P\_SiO}_2_{700}$  is also recorded at 100 K

under Dynamic Nuclear Polarization Surface Enhanced  $^{31}\text{P}$  ssNMR Spectroscopy (DNP SENS) (blue trace in Figure B.4b; the data for other samples are provided in Table B.S2). At this temperature, the signal at 28.1 ppm displays a larger number of spinning side bands, consistent with a more static surface species at 100 K. The  $^{31}\text{P}$  ssNMR at 100 K and 293 K could be fitted to obtain the CSA parameters listed in Table B.1. At 293 K, the corresponding  $\Omega$  of downfield site 1 and upfield site 2 are 0 and 151, respectively. However, at 100 K, the corresponding  $\Omega$  of site 1 significantly increased to 144, while the site 2 remained a similar value of 172, indicating that the downfield site 1 is associated with a very dynamic probably physisorbed species. On the other hand, the corresponding  $\Omega$  of upfield site 2 is not very sensitive to temperature, indicating that this species is rigid, chemically grafted on the silica surface and strongly interacting with the surface shutting down dynamics.<sup>18</sup> This proposal is confirmed by recording  $^{31}\text{P}$  ssNMR spectra on samples washed with THF, where the main peak at 28.1 ppm totally disappears, while the peak at 17.2 ppm remains (Figure B.S1-S4).

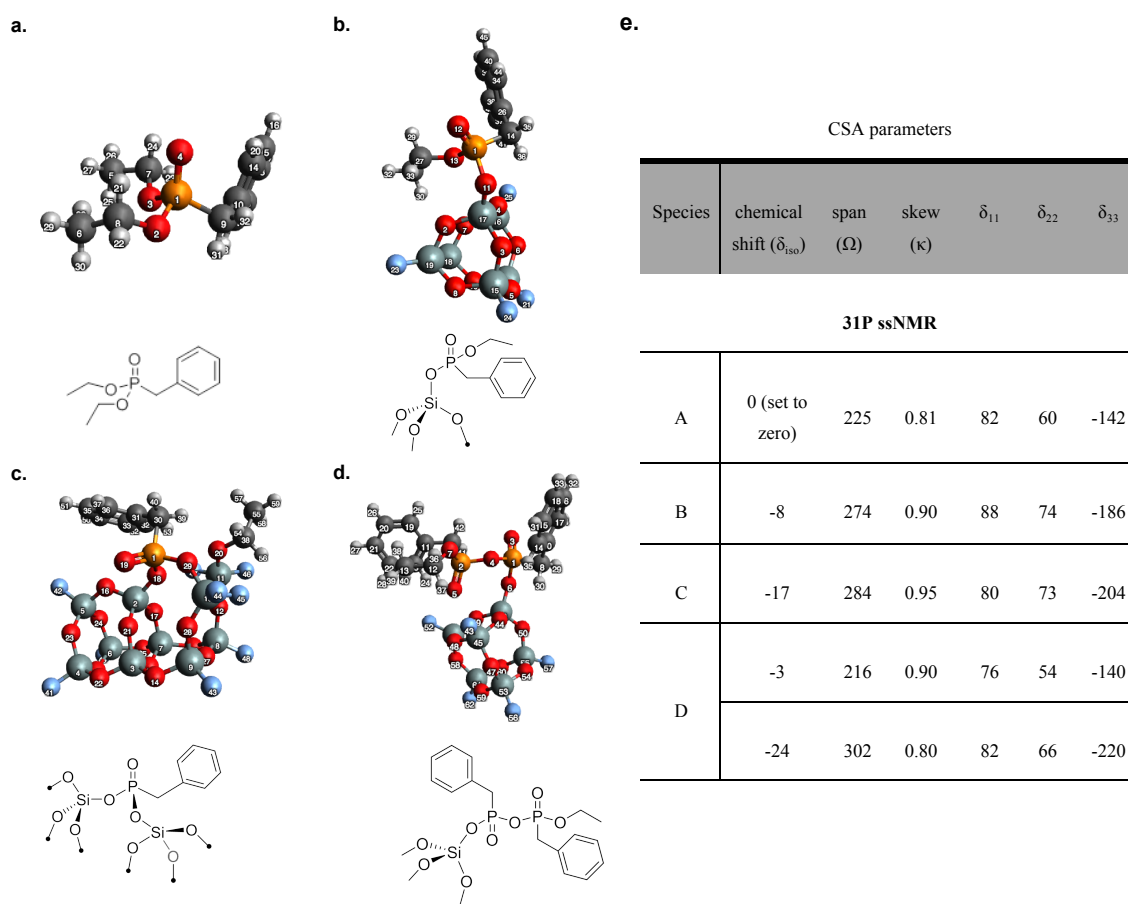


**Figure B.4.** (a)  $^{31}\text{P}$  ssNMR CP-MAS spectra and (b) DNP SENS  $^{31}\text{P}$  CP-MAS (blue trace) of diethylbenzylphosphonate grafted on silica dehydroxylated at 700 °C ( $\text{P\_SiO}_{2\_700}$ ) fit with two sets of CSA parameters (purple and red traces).

**Table B.1.** CSA parameters of SiO<sub>2-700</sub> of silica surface via fitting to the acquired <sup>31</sup>P ssNMR at 293 K and 100 K

CSA parameters						
site	chemical shift ( $\delta_{\text{iso}}$ )	span ( $\Omega$ )	skew ( $\kappa$ )	$\delta_{11}$	$\delta_{22}$	$\delta_{33}$
<b>31P ssNMR at 293 K</b>						
site 1	27	0	0.26	28	28	27
site 2	17	151	0.99	68	67	-82
<b>31P ssNMR at 100 K</b>						
site 1	30	144	0.61	87	59	-57
site 2	20	172	0.58	90	53	-83

To fully ascertain the assignment of the <sup>31</sup>P NMR spectra, four phosphonate species are modelled and their calculated chemical shift compared with the experimental results: the molecular precursor (**A**, Figure B.5a), a mono-grafted species (**B**, Figure B.5b), a bipodal-grafted species (**C**, Figure B.5c), and a phosphonate dimer on silica (**D**, Figure B.5d). By comparison with the diethylbenzyl phosphonate molecular precursor, grafting leads to an upfield shift of -8 and -17 for mono-grafted and bipodal-grafted species (Table B.2). The phosphonate dimer on silica is associated with two distinct chemical shifts of -24 and -3 ppm for the phosphonate species directly bound to silica surface and the species not directly bound to the surface, respectively. Of all, the species **B** with a calculated upfield shift of 8 ppm is closer to experimental observation, indicating that the observed species are mono-grafted.

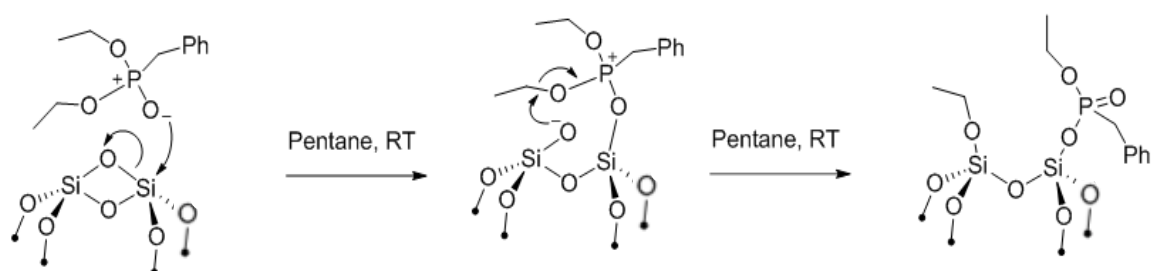


**Figure B.5.** Proposed surface species of diethylbenzyl phosphonate on silica: (a) diethyl benzylphosphonate molecule, species A; (b) isolated phosphonate, species B; (c) bipodal phosphonate on silica; (d) phosphonate dimer on silica; (e) NMR CSA parameters calculated from DFT for four sites of diethylbenzylphosphonate grafted on silica dehydroxylated at 700 °C ( $\text{P\_SiO}_{2\text{-}700}$ ).

In summary, NMR results indicate that grafting of phosphonate in pentane generates two major phosphorus species adsorbed on the  $\text{SiO}_2$  surface: one is dynamic at  $\sim 28$  ppm and physisorbed species, while another one – rigid and chemisorbed – appears at  $\sim 17$  ppm. The former can in fact be removed by washing with coordinating solvent like THF. More importantly, the chemisorbed species are preferentially formed on silica partially dehydroxylated at a very high temperature, which contains smaller amount of silanols but where highly strained siloxane bridges exist. These data point to the selective grafting of phosphonate on siloxane bridges and not on surface silanols, in sharp contrast to the metal alkoxides.<sup>13, 19</sup> This is consistent with FT-IR data (Figure B.2), which shows that the  $\text{V}_{\text{OH}}$  peak at  $3745\text{ cm}^{-1}$  is barely affected by the reaction with the phosphonate. The chemisorbed species are attributed to



monografted species according to computational models; we thus propose that the phosphonate selectively react with strained siloxane bridges as shown in Scheme B.1 and it strongly interact with adjacent OH groups since broad bands – associated respectively with the OH interacting with phenyl and P=O species – are observed around 3600 and 3200  $\text{cm}^{-1}$ .



**Scheme B.1.** Proposed strain-open reaction between diethylbenzyl phosphonate and strain siloxane on the silica surface.

### B.3. Conclusion

In this work, it was shown that diethyl benzylphosphonate hardly grafts on the  $\text{SiO}_2_{300}$  and that the amount of grafting phosphonate species increases with increasing dehydroxylation temperatures of silica, indicating that surface silanols are not the main grafting sites. It is proposed that grafting occurs on siloxane bridges, in particular strain siloxane bridges, which become more abundant with increasing dehydroxylation temperature. Overall, this work points out that surface grafting mode of molecular species on metal oxide could be significantly changed depending on different surface environments.

#### ***B.4. Experimental details***

##### **General Considerations**

The experiments were carried out by Schlenk techniques and in an mBraun LABstar glovebox under argon atmosphere. Glassware was made out of glass where the temperature was below 500 °C and out of quartz where the temperature exceeded 500 °C. Commercial chemicals as well as solvents were dried before use by using a drying agent followed by distillation. Pentane and toluene were dried using a MBraun solvent purification system. As a support, Aerosil® 200 of Evonik Industries was used. Toluene-d8 was dried over Na/benzophenone and degassed by three freeze-pump-thaw cycles. Infrared spectra were recorded on a Bruker Alpha FT-IR spectrometer. Every glassware was oven-dried for at least 4 h prior to use at temperatures greater than 150 °C.

##### **Dehydroxylation of silica at 300°C**

Silica was compacted using water and then sieved to obtain particles between 25 and 45 µm. The dihydroxylation of compacted silica was done in the following way: ca. 2.5 g of silica was loaded in a quartz reactor and heated under air to 500 °C for calcination using a ramp of 200 °C h<sup>-1</sup>. After 16 h, the reactor was evacuated (10<sup>-5</sup> mbar). Until the temperature decreased down to RT, degassed H<sub>2</sub>O in a rotaflow was connected to the system for hydroxylation for 1 h, and then the temperature was increased to 300 °C for 5 h. Then, disconnect the rotaflow with H<sub>2</sub>O and evacuate the reactor (10<sup>-5</sup> mbar) at 300 °C for 12 h. After dehydroxylation, the reactor was closed while hot and cooled down before emptying inside the glovebox.

##### **Dehydroxylation of silica at high temperature (700 or 900 °C in this work)**

Silica was compacted using water and then sieved to obtain particles between 25 and 45 µm. The dihydroxylation of compacted silica was done in the following way: ca. 2.5 g of silica was loaded in a quartz reactor and heated under air to 500 °C for calcination using a ramp of 200 °C h<sup>-1</sup>. After 16 h, the reactor was evacuated (10<sup>-5</sup> mbar) for dehydroxylation. To obtain SiO<sub>2-700</sub>, the reactor was kept at 500 °C for 12 h and then heated to 700 °C for 8 h using a ramp of 60 °C h<sup>-1</sup>. On the other hand, to obtain SiO<sub>2-900</sub>, the reactor was kept at 500 °C for 12 h and then heated to 900 °C for

8 h using a ramp of  $60\text{ }^{\circ}\text{C h}^{-1}$ . After dehydroxylation, the reactor was closed while hot and cooled down before emptying inside the glovebox.

### **General Procedure for diethyl benzylphosphonate grafting on dehydroxylated silica**

Dehydroxylated silica (Aerosil-200, Degussa, 1.2 g) was suspended in pentane (6 mL) containing diethyl benzylphosphonate (0.48 mL) and stirred for 16 h in a sealed schlenk under static argon at room temperature. The remaining solution was transferred to an NMR tube containing ferrocene as an internal standard, and the propene and butane were quantified using  $^1\text{H}$  NMR spectroscopy. The solid was washed with pentane (3 x 6 mL). The solid was dried on a high vac line ( $10^{-5}$  mbar) for 3 h and stored in an Ar filled glovebox.

### **DNP sample preparation**

Given the nature of the sample, all sample manipulations were conducted in an argon-filled glovebox. The sample powder was incipient wetness impregnated with a 16mM solution of TEKPol in 1,1,2,2-tetrachloroethane (TCE) at a ratio of 1 mg per  $\mu\text{L}$ . The mixture was packed into a 3.2 mm sapphire rotor. A Teflon insert was placed on the sample, and the rotor was finally closed with a corresponding zirconia drive cap. The packed rotor was then immediately inserted into the pre-cooled DNP probe for experiments.

### **DNP enhanced solid-state NMR**

DNP enhanced solid-state NMR experiments were conducted on a Bruker 600 MHz (14.1 T) DNP NMR spectrometer using a 3.2 mm HX probe located at ETH Zurich. The static magnetic field was externally referenced to adamantane with the higher frequency peak set to 38.4 ppm with respect to TMS (0 ppm). The sample is cooled to 100 K by a cryogenic heat exchanger system. Microwaves used to generate electron polarization are provided by gyrotrons emitting at and 395 GHz (600 MHz spectrometer) with power between 6 to 10 W. Ramped cross polarization (CP) from  $^1\text{H}$  to  $^{31}\text{P}$  was used for all experiments with contact time at 1 ms. The CP contact powers were optimized to fulfill Hartmut-Hahn condition under MAS. SPINAL64 was used for  $^1\text{H}$  decoupling at an  $rf$  field of 100 kHz. The DNP build up time ( $T_{\text{DNP}}$ )

was measured by saturation recovery, and the recycling delay of all experiments was set to  $1.3 \times T_{DNP}$ .

### **Solid-state NMR**

Solid-state NMR experiments were conducted on a Bruker 400 MHz (9.4T) NMR spectrometer using a 4 mm double resonance probe located at ETH Zurich. All samples were packed in 4 mm zirconia rotors using the corresponding VESPEL drive caps. The static magnetic field was externally referenced to  $(\text{NH}_4)_2\text{HPO}_4 \cdot 2\text{H}_2\text{O}$  with the  $^{31}\text{P}$  signal set to 0 ppm. Ramped cross polarization (CP) from  $^1\text{H}$  to  $^{31}\text{P}$  was used for all experiments with contact time at 3 ms. The CP contact powers were optimized to fulfill Hartmut-Hahn condition under MAS. SPINAL64 was used for  $^1\text{H}$  decoupling at an *rf* field of 73 kHz. The recycling delay was set to 1 and 2 seconds for CPMAS and single-pulse experiments, respectively.

### **DFT calculation**

The structures of the non-/grafted phosphorous species were fully optimized with B3LYP including D3 empirical dispersion corrections using the Gaussian 09 code as a cluster model. All atoms were described by the 6-31G(d,p) basis set.

Calculations of the NMR parameters were carried out at the B3LYP-D3 level as implemented in the ADF code (2014). The all-electron TZP basis set was used for all atoms in the NMR parameter calculations. Relativistic effects and spin-orbit couplings were taken into account through the ZORA method for the calculations of the isotropic chemical shift ( $\delta_{\text{iso}}$ ) and the principal components ( $\delta_{11}$ ,  $\delta_{22}$ , and  $\delta_{33}$ ) of all considered species. For the calculations of  $\delta_{\text{iso}}$ , the chemical shieldings of molecular diethyl benzylphosphate was set to 0 ppm for  $^{31}\text{P}$ .

### B.5. References

1. Madhusudanan, S. P.; Gangaja, B.; Shyla, A. G.; Nair, A. S.; Nair, S. V.; Santhanagopalan, D., Sustainable Chemical Synthesis for Phosphorus-Doping of TiO<sub>2</sub> Nanoparticles by Upcycling Human Urine and Impact of Doping on Energy Applications. *ACS Sustainable Chemistry & Engineering* **2017**, *5* (3), 2393-2399.
2. Materna, K. L.; Crabtree, R. H.; Brudvig, G. W., Anchoring groups for photocatalytic water oxidation on metal oxide surfaces. *Chem. Soc. Rev.* **2017**.
3. Mathey, L.; Alphazan, T.; Valla, M.; Veyre, L.; Fontaine, H.; Enyedi, V.; Yckache, K.; Danielou, M.; Kerdiles, S.; Guerrero, J.; Barnes, J.-P.; Veillerot, M.; Chevalier, N.; Mariolle, D.; Bertin, F.; Durand, C.; Berthe, M.; Dendooven, J.; Martin, F.; Thieuleux, C.; Grandidier, B.; Copéret, C., Functionalization of Silica Nanoparticles and Native Silicon Oxide with Tailored Boron-Molecular Precursors for Efficient and Predictive p-Doping of Silicon. *The Journal of Physical Chemistry C* **2015**, *119* (24), 13750-13757.
4. Ho, J. C.; Yerushalmi, R.; Jacobson, Z. A.; Fan, Z.; Alley, R. L.; Javey, A., Controlled nanoscale doping of semiconductors via molecular monolayers. *Nat Mater* **2008**, *7* (1), 62-67.
5. Hazut, O.; Agarwala, A.; Amit, I.; Subramani, T.; Zaidiner, S.; Rosenwaks, Y.; Yerushalmi, R., Contact Doping of Silicon Wafers and Nanostructures with Phosphine Oxide Monolayers. *ACS Nano* **2012**, *6* (11), 10311-10318.
6. Delley, M. F.; Núñez-Zarur, F.; Conley, M. P.; Comas-Vives, A.; Siddiqi, G.; Norsic, S.; Monteil, V.; Safonova, O. V.; Copéret, C., Proton transfers are key elementary steps in ethylene polymerization on isolated chromium(III) silicates. *Proc. Natl. Acad. Sci. U. S. A.* **2014**, *111* (32), 11624-11629.
7. Searles, K.; Siddiqi, G.; Safonova, O. V.; Copéret, C., Silica-supported isolated gallium sites as highly active, selective and stable propane dehydrogenation catalysts. *Chemical Science* **2017**, *8* (4), 2661-2666.
8. Copéret, C.; Comas-Vives, A.; Conley, M. P.; Estes, D. P.; Fedorov, A.; Mougél, V.; Nagae, H.; Núñez-Zarur, F.; Zhizhko, P. A., Surface Organometallic and Coordination Chemistry toward Single-Site Heterogeneous Catalysts: Strategies, Methods, Structures, and Activities. *Chem. Rev.* **2016**, *116* (2), 323-421.

9. Stalzer, M. M.; Delferro, M.; Marks, T. J., Supported Single-Site Organometallic Catalysts for the Synthesis of High-Performance Polyolefins. *Catal. Lett.* **2015**, *145* (1), 3-14.
10. Copéret, C.; Fedorov, A.; Zhizhko, P. A., Surface Organometallic Chemistry: Paving the Way Beyond Well-Defined Supported Organometallics and Single-Site Catalysis. *Catal. Lett.* **2017**, *147* (9), 2247-2259.
11. Pelletier, J. D. A.; Basset, J.-M., Catalysis by Design: Well-Defined Single-Site Heterogeneous Catalysts. *Acc. Chem. Res.* **2016**, *49* (4), 664-677.
12. Estes, D. P.; Cook, A. K.; Lam, E.; Wong, L.; Copéret, C., Understanding the Lewis Acidity of Co(II) Sites on a Silica Surface. *Inorg. Chem.* **2017**, *56* (14), 7731-7736.
13. Conley, M. P.; Rossini, A. J.; Comas-Vives, A.; Valla, M.; Casano, G.; Ouari, O.; Tordo, P.; Lesage, A.; Emsley, L.; Coperet, C., Silica-surface reorganization during organotin grafting evidenced by  $^{119}\text{Sn}$  DNP SENS: a tandem reaction of gem-silanols and strained siloxane bridges. *Phys. Chem. Chem. Phys.* **2014**, *16* (33), 17822-17827.
14. Scott, S. L.; Basset, J.-M., Coordination Chemistry on Surfaces: A New Method To Graft Rhenium(VII) Oxide on Highly Dehydroxylated Oxides. *J. Am. Chem. Soc.* **1994**, *116* (26), 12069-12070.
15. Fleischman, S. D.; Scott, S. L., Evidence for the Pairwise Disposition of Grafting Sites on Highly Dehydroxylated Silicas via Their Reactions with  $\text{Ga}(\text{CH}_3)_3$ . *J. Am. Chem. Soc.* **2011**, *133* (13), 4847-4855.
16. Alphazan, T.; Mathey, L.; Schwarzwälder, M.; Lin, T.-H.; Rossini, A. J.; Wischert, R.; Enyedi, V.; Fontaine, H.; Veillerot, M.; Lesage, A.; Emsley, L.; Veyre, L.; Martin, F.; Thieuleux, C.; Copéret, C., Monolayer Doping of Silicon through Grafting a Tailored Molecular Phosphorus Precursor onto Oxide-Passivated Silicon Surfaces. *Chem. Mater.* **2016**, *28* (11), 3634-3640.
17. Shimizu, Y.; Takamizawa, H.; Inoue, K.; Yano, F.; Nagai, Y.; Lamagna, L.; Mazzeo, G.; Perego, M.; Prati, E., Behavior of phosphorous and contaminants from molecular doping combined with a conventional spike annealing method. *Nanoscale* **2014**, *6* (2), 706-710.
18. Blanc, F.; Basset, J.-M.; Copéret, C.; Sinha, A.; Tonzetich, Z. J.; Schrock, R. R.; Solans-Monfort, X.; Clot, E.; Eisenstein, O.; Lesage, A.; Emsley, L., Dynamics of Silica-Supported Catalysts Determined by Combining Solid-State NMR Spectroscopy and DFT Calculations. *J. Am. Chem. Soc.* **2008**, *130* (18), 5886-5900.

19. Allouche, F.; Klose, D.; Gordon, C. P.; Ashuiev, A.; Wörle, M.; Kalendra, V.; Mougél, V.; Copéret, C.; Jeschke, G., Low-Coordinated Titanium(III) Alkyl—Molecular and Surface—Complexes: Detailed Structure from Advanced EPR Spectroscopy. *Angewandte Chemie International Edition* 0 (0).

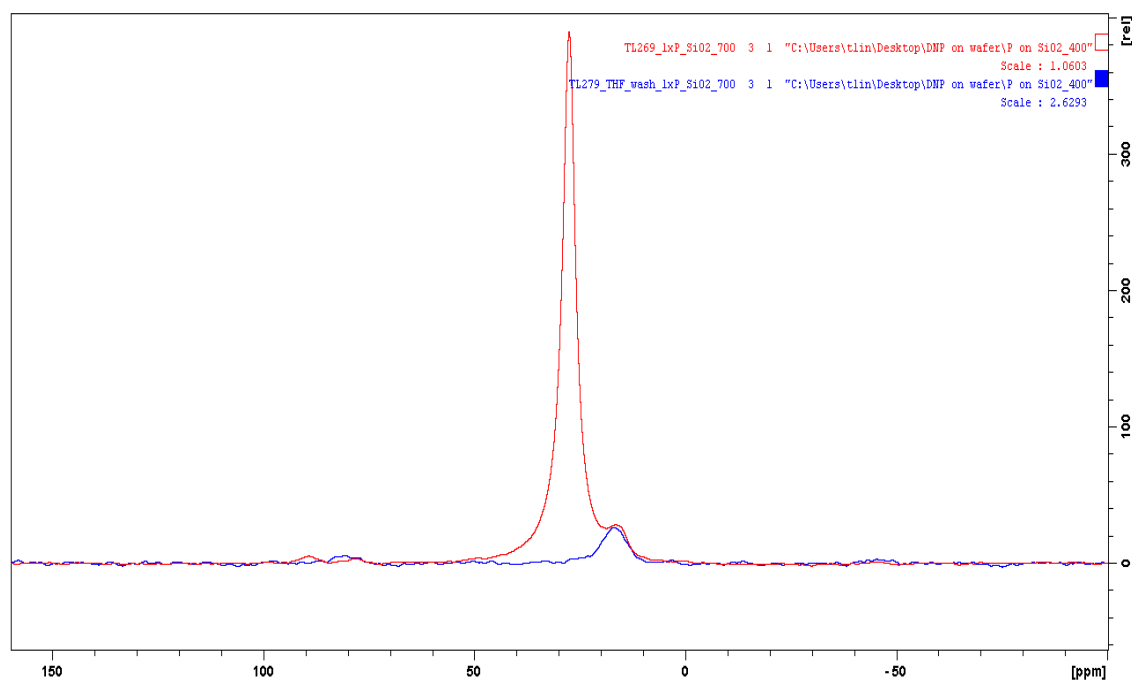
**Table B.S1.** CSA parameters of SiO<sub>2\_700/900</sub> of silica surface via fitting to the acquired <sup>31</sup>P SSNMR at 293 K

CSA parameters						
site	chemical shift ( $\delta_{\text{iso}}$ )	span ( $\Omega$ )	skew ( $\kappa$ )	$\delta_{11}$	$\delta_{22}$	$\delta_{33}$
<b>SiO<sub>2_700</sub></b>						
site 1	27	0	0.26	28	28	27
site 2	17	151	0.99	68	67	-82
<b>SiO<sub>2_900</sub></b>						
site 1	26	14	-0.85	36	23	22
site 2	17	160	0.67	79	53	-81

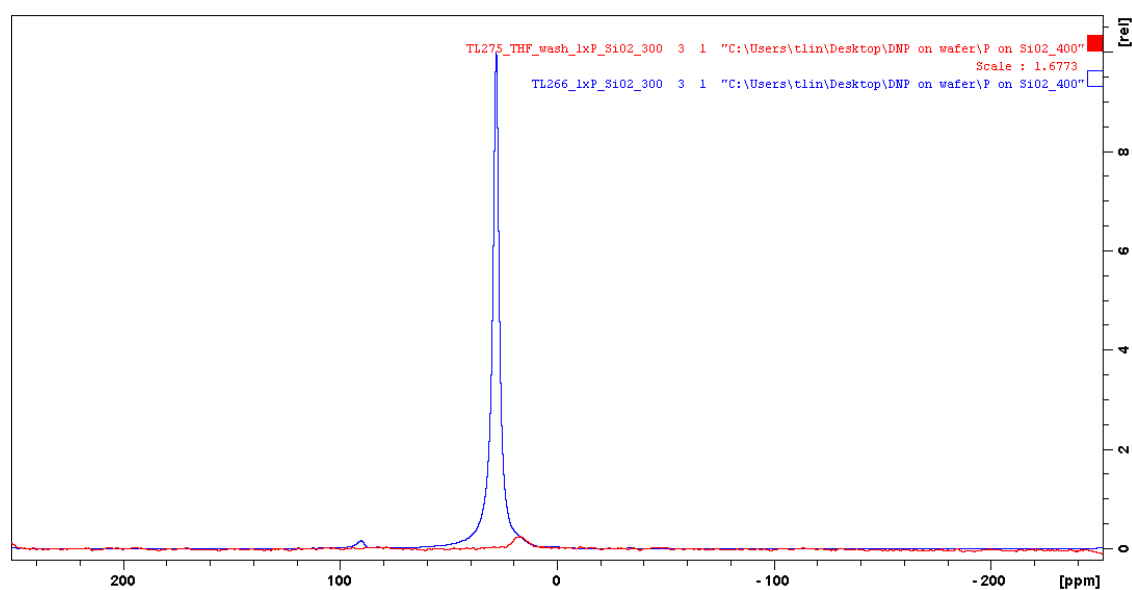


**Table B.S2.** CSA parameters of SiO<sub>2\_x</sub> (X = 300, 500, 700 and 900 °C) of silica surface via fitting to the acquired Dynamic Nuclear Polarization Surface Enhanced <sup>31</sup>P SSNMR

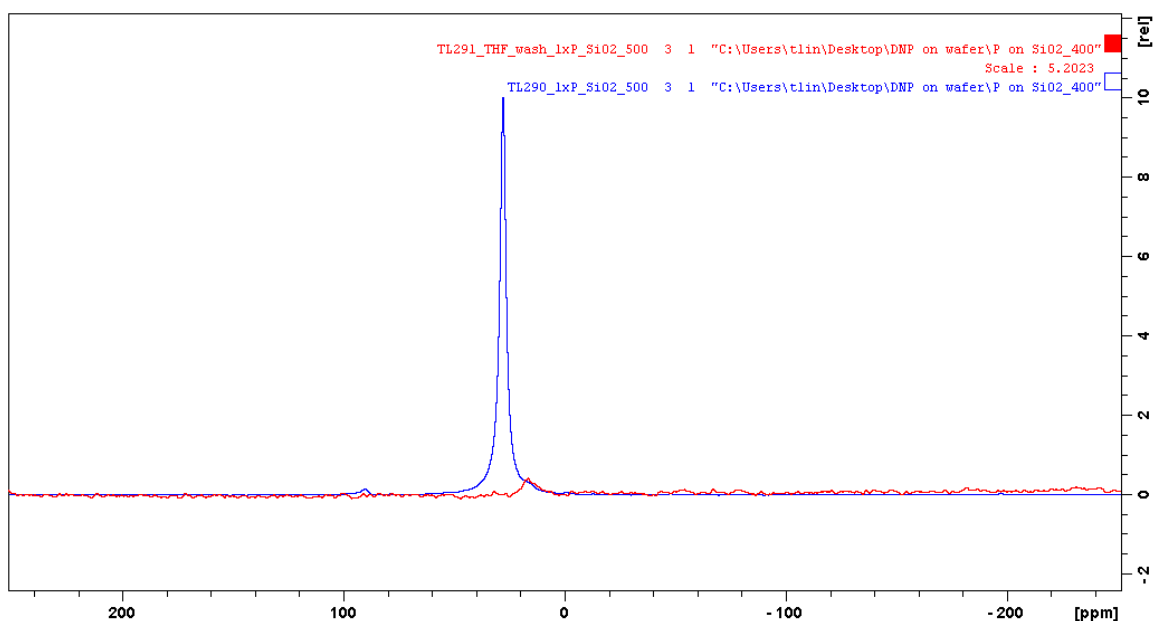
CSA parameters						
site	chemical shift ( $\delta_{iso}$ )	span ( $\Omega$ )	skew ( $\kappa$ )	$\delta_{11}$	$\delta_{22}$	$\delta_{33}$
<b>SiO<sub>2_300</sub></b>						
site 1	30	138	0.55	87	56	-51
site 2	20	161	0.67	82	55	-79
<b>SiO<sub>2_500</sub></b>						
site 1	31	126	0.66	80	59	-46
site 2	20	172	0.66	87	58	-86
<b>SiO<sub>2_700</sub></b>						
site 1	30	144	0.61	87	59	-57
site 2	20	172	0.58	90	53	-83
<b>SiO<sub>2_900</sub></b>						
site 1	30	140	0.50	87	55	-53
site 2	20	187	0.60	91	58	-90



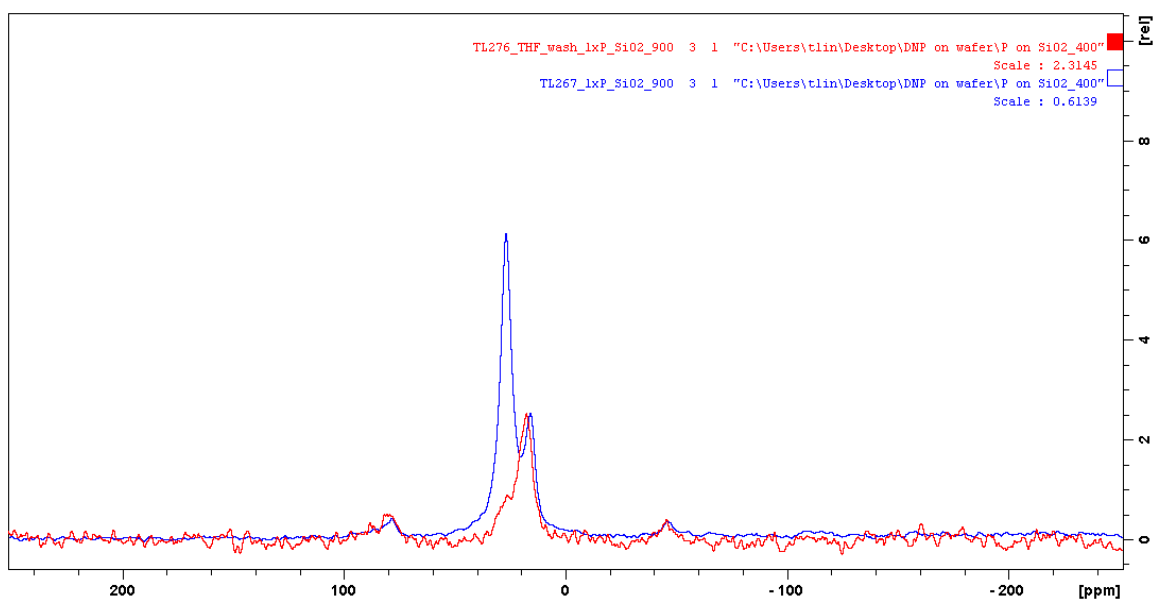
**Figure B.S1.**  $^{31}\text{P}$  solid-state NMR direct-excitation spectra of diethylbenzylphosphonate on silica dehydroxylated at 700 °C (P\_SiO<sub>2</sub><sub>700</sub>, red trace) and the materials after THF washing (blue trace).



**Figure B.S2.**  $^{31}\text{P}$  solid-state NMR direct-excitation spectra of diethylbenzylphosphonate on silica dehydroxylated at 300 °C (P\_SiO<sub>2</sub><sub>300</sub>, red trace) and the materials after THF washing (blue trace).



**Figure B.S3.**  $^{31}\text{P}$  solid-state NMR direct-excitation spectra of diethylbenzylphosphonate on silica dehydroxylated at 500 °C (P\_SiO<sub>2\_500</sub>, red trace) and the materials after THF washing (blue trace).



**Figure B.S4.**  $^{31}\text{P}$  solid-state NMR direct-excitation spectra of diethylbenzylphosphonate on silica dehydroxylated at 900 °C (P\_SiO<sub>2\_900</sub>, red trace) and the materials after THF washing (blue trace).

## **Appendix C: Additional synthesis**

### ***Preparation of nickel phosphide catalyst for dry reforming of methane<sup>1</sup>***

The experiments were carried out using Schlenk techniques. Toluene was dried and collected using a mBraun SBS-800 purification system and degassed by Schlenk techniques (vacuum to  $10^{-1}$  mbar and purged with dry Ar for 10 times). Nickel phosphide (>98.5%) was purchased from Sigma-Aldrich. Ni(COD)<sub>2</sub> (99.5%) was purchased from Strem Chemicals. Hexadecylamine (HDA, 99.5%) and Steaic acid (99.5%) were purchased from Alfa Aesar. Incipient Wetness Impregnations were carried out using a Schlenk line with Ar (grade 4.5) and  $10^{-3}$  mbar vacuum. H<sub>2</sub> was purified over R3-11 BASF catalyst / MS 4 Å before use. Silica was obtained from Aerosil Degussa.

### ***Catalyst Synthesis***

#### **Dehydroxylation of silica at 700°C**

Silica was compacted using water and then sieved to obtain particles between 25 and 45  $\mu\text{m}$ . The dihydroxylation of compacted silica was done in the following way: ca. 2.5 g of silica was loaded in a quartz reactor and heated under air to 500 °C for calcination using a ramp of 200 °C h<sup>-1</sup>. After 16 h, the reactor was evacuated ( $10^{-5}$  mbar) for dehydroxylation. To obtain SiO<sub>2-700</sub>, the reactor was kept at 500 °C for 12 h and then heated to 700 °C for 8 h using a ramp of 60 °C h<sup>-1</sup>.

#### **Ni<sub>2</sub>P colloids (Ni<sub>2</sub>P<sub>Col</sub>) preparation**

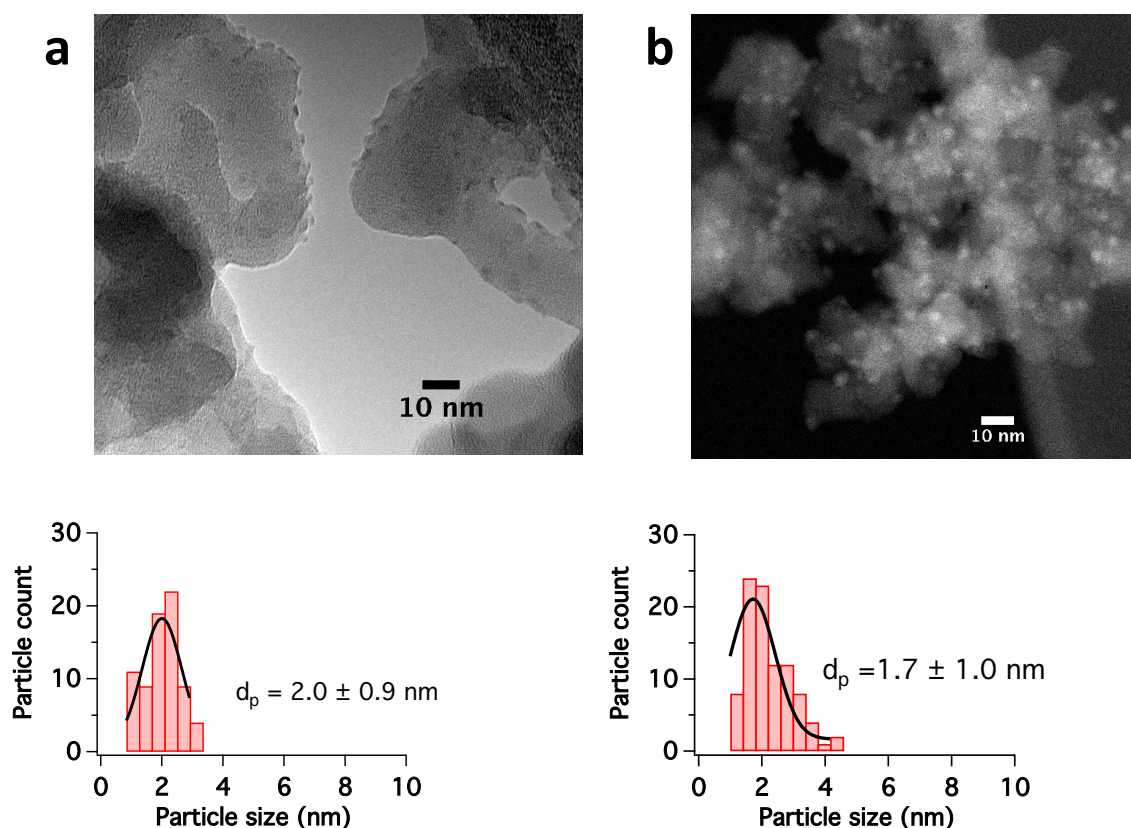
Ni(COD)<sub>2</sub> (84 mg, 0.3 mmol), HDA (34 mg, 0.15 mmol), and steaic acid (40 mg, 0.15 mmol) were placed in a 325 mL Fischer–Porter bottle in a glove box and dissolved in toluene (80 mL). The solution was then pressurized under 1.5 bar PH<sub>3</sub> (1% PH<sub>3</sub> in He, 0.15 mmol of PH<sub>3</sub>) at 25 °C for 48 h, during which the color turned black. The black solution was evaporated under vacuum down to a volume of approximately 2 mL.

## Catalyst synthesis

1 g of SiO<sub>2</sub> support was impregnated with the concentrated 2 mL colloidal solution using an incipient wetness impregnation method (IWI). After drying of the materials under high vacuum at room temperature for 3 h, the catalyst was calcined under flow of synthetic air for 5 h at 400 °C with a temperature ramp of 1 °C.min<sup>-1</sup>. Prior to catalytic test, the catalyst was reduced under flow of hydrogen at 650 °C for 1 h (100 mL.min<sup>-1</sup>).

## TEM characterizations

TEM image shows that there are homogeneous nanoparticles distributed on the silica support after the impregnation of Ni<sub>x</sub>P<sub>Col</sub> by IWI method, for which the size is ~2 nm (Figure C.1a). After the H<sub>2</sub> reduction, the catalyst also shows a homogeneous distribution with the particle size of ~ 1.7 nm via the HAADF-STEM measurement (Figure C.1b).



**Figure C.1.** (a) Bright field TEM image and size distribution of Ni<sub>x</sub>P<sub>Col</sub>/ SiO<sub>2</sub>; (b) HAADF-STEM image and size distribution of Ni<sub>x</sub>P/SiO<sub>2</sub>.

## ***References***

1. Margossian, T., *PhD thesis, ETH Zürich, Switzerland, 2017.*

## **Curriculum Vitae**



## Tsung-Han Lin

Email: lin@inorg.chem.ethz.ch

Mobile: +41-78-827-3246

Address: Birchstrasse 590, 8052 Zürich

Nationality: Taiwan

Date of Birth: 16.06.1987

Language: Mandarin (native), English (professional), German (basic)

### WORK and RESEARCH EXPERIENCE

- |                     |   |
|---------------------|---|
| Oct. 2014-present   | PhD candidate, ETH Zürich, Dept. of Chemistry and Applied Bioscience  |
|                     | <ul style="list-style-type: none"><li>• Elucidated the surface of metal silicide layer from chemical approach by microstructural surface analysis.</li><li>• Initiated an interdisciplinary team with electrical engineer in EPFL and chemical engineer in ETH for transistor device build-up.</li><li>• Generated a conformal, conductive, and single-crystalline metal silicide layer based on the chemical solution technique.</li></ul>                           |
| Aug. 2012-Aug. 2014 | Process Engineer, Taiwan Semiconductor Manufacturing Company  |
|                     | <ul style="list-style-type: none"><li>• Improved productivity by 15% per year (corresponding to 150,000 USD/year) by improving receiving modes for laser signals.</li><li>• Optimized equipment quality monitoring processes to increase equipment available time by 14% during production ramp-up.</li></ul>   |
| Jul. 2009-Jun. 2011 | Research Assistant, NTU, Dept. of Materials Science and Engineering   |
|                     | <ul style="list-style-type: none"><li>• Elucidated the role of inorganic nanoparticles (<math>\text{Cu}_2\text{S}</math> and <math>\text{CdSe}</math>) in improving power conversion efficiency (PCE) of opto-electronic devices quantitatively by utilizing the technique of small angle X-ray scattering.</li><li>• Examined the structure of polymer and fullerene particles in the opto-electronic devices during annealing to increase the PCE by 31%.</li></ul> |

### EDUCATION

- |                |  |
|----------------|--|
| 2014 - Present | Ph.D candidate in the department of Chemistry and Applied Bioscience, Eidgenössische Technische Hochschule Zürich, Switzerland |
| 2009 - 2011    | Master of Materials Science and Engineering, National Taiwan University, Taiwan  |
| 2005 - 2009    | Bachelor of Materials Science and Engineering, National Taiwan University, Taiwan  |

### SKILLS

**Synthesis:** nanoparticle synthesis by colloidal one-pot reaction; nanoparticle synthesis by gas-phase reaction; nanoparticle synthesis by hot-injection; inorganic metal complex synthesis.

**Device fabrication/characterization:** FTIR spectroscopy (Thermo Scientific Nicolet 6700 and Bruker ALPHA-T); Alpha stepper (KLA-Tencor); FIB-SEM (Zeiss NVision40); semiconductor device fabrication; I-V characteristic measurement with Signatone S1160; I-V data acquired by a Keysight B1500; small-angle X-ray scattering (SAXS) analysis and transmission electron microscopy (CM12 and Hitachi HT7700).

#### AWARDS and FELLOWSHIPS

2010	Poster Award, Materials Research Society of Taiwan Annual Conference
2010	Poster Award, 16th National Synchrotron Radiation Research Center User's Meeting
2009	Award of Outstanding Engineering Essay, Chinese Institute of Engineers
2008	Presidential Award, top performance of the class, National Taiwan University
2008	Fellowship and Research Grant for Undergraduate Researcher, Taiwan National Science Council

#### SELECTED PUBLICATIONS AND CONFERENCE PROCEEDINGS

- 1.** Tsung-Han Lin, Tigran Margossian, Li-Qing Zheng, Sudhir Kumar, Ivan Morazau, Olha Sereda, Dmitry Y Zemlyanov, Chih-Jen Shih, Renato Zenobi, David Baudouin, Giovanni De Micheli, Pierre-Emmanuel Gaillardon, Christophe Copéret, "Conformal Deposition of Conductive Single-Crystalline Cobalt Silicide Layer on Si Wafer via a Colloidal Approach" 2018, *Chem. Mater.*, 30, 2168-2173.
- 2.** Tsung-Han Lin, Tigran Margossian, Michele De Marchi, Maxime Thammasack, Dmitry Y Zemlyanov, Sudhir Kumar, Jakub Jagielski, Li-Qing Zheng, Chih-Jen Shih, Renato Zenobi, Giovanni De Micheli, David Baudouin, Pierre-Emmanuel Gaillardon, Christophe Copéret, "Low-Temperature Wet Conformal Nickel Silicide Deposition for Transistor Technology through an Organometallic Approach" 2017, *ACS Appl. Mater. Interfaces*, 9, 4948-4955.
- 3.** Thibault Alphazan, Laurent Mathey, Martin Schwarzwälder, Tsung-Han Lin, Aaron J Rossini, Raphaël Wischert, Virginie Enyedi, Hervé Fontaine, Marc Veillerot, Anne Lesage, Lyndon Emsley, Laurent Veyre, François Martin, Chloé Thieuleux, Christophe Copéret, "Monolayer Doping of Silicon through Grafting a Tailored Molecular Phosphorus Precursor onto Oxide-Passivated Silicon Surfaces" 2016, *Chem. Mater.*, 28, 3634-3640.
- 4.** Hsueh-Chung Liao, Cheng-Si Tsao, Tsung-Han Lin, Meng-Huan Jao, Chih-Min Chuang, Sheng-Yong Chang, Yu-Ching Huang, Yu-Tsun Shao, Charn-Ying Chen, Chun-Jen Su, U-SerJeng, Yang-Fang Chen, and Wei-Fang Su, "Nanoparticle Tuned Self-Organization of Bulk Heterojunction Hybrid Solar Cell with Enhanced Performance", 2012, *ACS Nano* 6(2), 1657-1666.
- 5.** Hsueh-Chung Liao, Cheng-Si Tsao, Tsung-Han Lin, Chih-Min Chuang, Charn-Ying Chen, U-SerJeng, Chiu-Hun Su, Yang-Fang Chen, Wei-Fang Su, "Quantitative Nanoorganized Structural Evolution for High Efficient Bulk Heterojunction Polymer Solar Cell", 2011, *J. Am. Chem. Soc.*, 133, 13064-13073.
- 6.** Yu-Ching Huang, Tsung-Han Lin<sup>\*</sup> and Wei-Fang Su, "Interfacial Behaviors of Surface Modified TiO<sub>2</sub> Nanorods in Poly(3-hexylthiophene)/TiO<sub>2</sub> Hybrid System for Solar Cell Applications," *International Union of Materials Research Societies (IUMRS) - International Conference on Electronic Materials*, Seoul, Korea, 2010. (**\*Oral presentation**)